The Dissertation Committee for Eric Lewis Danielson Certifies that this is the approved version of the following dissertation:

Lateral Device Techniques for Characterizing Organic Bulk Heterojunction Photovoltaic Materials

Committee:

Ananth Dodabalapur, Supervisor

Seth R. Bank

Arumugam Manthiram

Keith J. Stevenson

David A. Vanden Bout

Edward T. Yu

Lateral Device Techniques for Characterizing Organic Bulk Heterojunction Photovoltaic Materials

by

Eric Lewis Danielson, B.S.; M.S.

Dissertation

Presented to the Faculty of the Graduate School of

The University of Texas at Austin

in Partial Fulfillment

of the Requirements

for the Degree of

Doctor of Philosophy

The University of Texas at Austin

August 2014

Acknowledgements

I would first like to thank my advisor Professor Ananth Dodabalapur for his guidance and support of my education over the past five years. In addition, I'd like to thank all of the present and former members of the Organic Electronics Research Group: Dr. Brian Cobb, Dr. Davianne Duarte, Dr. Tae-Jun Ha, Dr. Chen-Guan Lee, Seonpil Jang, Bongjun Kim, Seohee Kim, Xin Xu, Barrett Worley, and especially Dr. Chris Lombardo, Kelly Liang, and Oleksiy Slobodyan for useful discussions, brainstorming, and help in the lab. Special thanks to Jo Ann Smith for her invaluable assistance with all things administrative, the Microelectronics Research Center staff for their advice and technical support, and the faculty and staff of the Materials Science and Engineering program. I can think of no place I would have rather spent the last five years than in Austin, and all of my friends here have made the graduate school experience much more enjoyable than it has any right to be. Finally, I would not be here without the advice, support, and love from my scientifically minded family, especially my mom, dad, and brother, to whom I dedicate this dissertation.

Lateral Device Techniques for Characterizing Organic Bulk Heterojunction Photovoltaic Materials

Eric Lewis Danielson, Ph.D.

The University of Texas at Austin, 2014

Supervisor: Ananth Dodabalapur

This work is focused on developing novel techniques for characterizing organic bulk heterojunction (BHJ) materials for organic photovoltaic (OPV) applications. Polymer:fullerene BHJs are a promising class of photovoltaic materials, but an improved understanding of the charge transport processes and materials science of BHJs is required for them to effectively compete with other photovoltaic systems. Key parameters of BHJ systems that need to be evaluated include both electron and hole mobilities, the carrier concentrations, the recombination mechanism and the recombination coefficient. For these studies, poly(3-hexylthiophene) (P3HT):[6,6]-phenyl C_{61}-butyric acid methyl ester (PCBM) have been characterized due to its wide use among researchers.

Traditional characterization techniques have focused on transient measurements in a vertical device configuration, but we demonstrate the use of lateral BHJ devices as materials diagnostic platforms. Lateral devices allow for direct access to the active layer for spatially resolved and environmental effect measurements. The devices are also measured under steady state operation, similar to a working OPV cell. Under these conditions, lateral BHJ devices exhibit space charge limited transport behavior. A detailed charge transport model is presented to describe the potential, electric field, and carrier concentration profiles of lateral BHJ devices, as well as the current versus voltage characteristics of different regions of the device.

We are able to calculate the slower carrier mobility from photocurrent measurements of lateral devices and the carrier mobility ratio from the device potential profile, even in ambipolar

BHJ systems. *In situ* potentiometry is used to construct detailed potential profiles of the device channel and calculate both carrier mobilities. The carrier concentration and recombination coefficient are calculated from lateral conductivity measurements, and we show that bimolecular recombination is the dominant mechanism in bulk P3HT:PCBM. A simplified *in situ* potentiometry and photocurrent measurement technique is presented to measure the time evolution of organic BHJ performance. Due to the open geometry of the lateral BHJ device, we are also able to monitor the change in key charge transport parameters, including the recombination mechanism, in response to environmental degradation, analyte exposure, and ambient temperature. We show increased geminate recombination in P3HT:$PC_{71}BM$ after prolonged light exposure. Lateral BHJ device measurements offer a useful complement to measurements on vertical photovoltaic structures and provide a more complete and detailed picture of OPV materials.

Table of Contents

List of Tables

List of Figures

Chapter 1: Organic Bulk Heterojunction Materials

1.1 Introduction

As the human population continues to grow into the 21st Century, demand for fossil fuel energy resources such as coal, oil, and natural gas will increase dramatically. The extraction and use of these non-renewable energy resources will cause many negative environmental effects, in particular the increased emission of greenhouse gases contributing to global warming. A variety of renewable sources of energy such as solar photovoltaic (PV) cells, solar thermal, wind, hydroelectric, tidal, and geothermal power will all need to be developed in concert to create a new clean energy generation and distribution system. Solar PV cells will be a key technology in this revolution due to the availability and magnitude of received solar energy, and the ease at which solar PV installations can be scaled from individual to utility scale power generation. PV cells currently account for approximately 136 GW of electrical power generated worldwide today and are the third largest renewable energy source behind hydroelectric and wind power, but are not yet cost-competitive with fossil fuel technologies.

Silicon (Si) PV cells constitute the majority of this installed solar capacity today, but have difficulty being cost-competitive with cheap fossil fuel technologies, particularly due to the high cost of the absorber material. As a result, there has been a tremendous amount of research devoted to develop a variety of thin film PV cell technologies within the last few decades. In particular, organic photovoltaics (OPV) have advanced rapidly and recently achieved device power conversion efficiencies (PCE) of more than 11% in recent years [1]. Si PV cells require a large volume (100-300 μm device thickness) of high grade semiconducting silicon as an absorber material, while organic semiconductors have strong absorption coefficients (typically $\geq 10^5$ cm^{-1}), giving high absorption even in thin ($\leq$ 100 nm) devices [2, 3]. OPV cells also have the potential to be fabricated using a variety of processes including spray coating, spin coating,

doctor blading, screen printing, and inkjet printing for high volume, low cost manufacturing [2, 4].

To understand the operation of a solar cell, consider the following series of energy band diagrams:

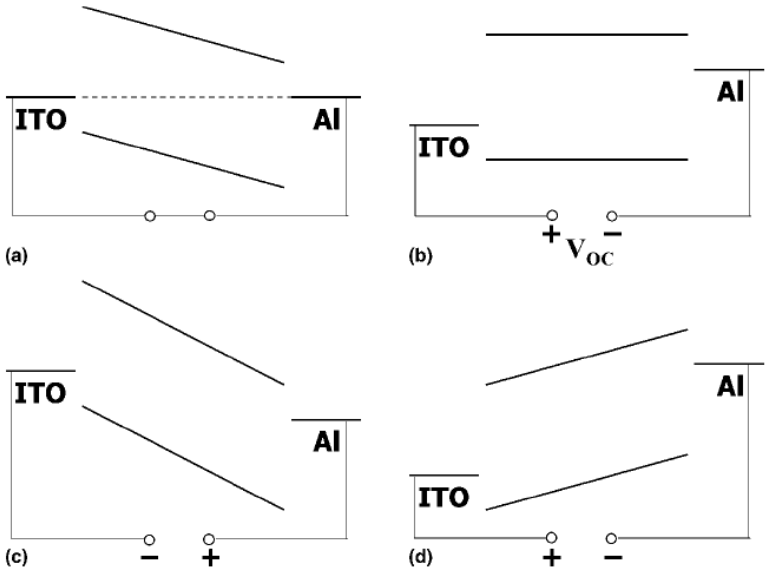

Figure 1.1: Metal-insulator-metal (MIM) energy level diagram of a diode under a) short circuit condition, b) open circuit condition, c) reversed bias, and d) forward bias larger than V_{oc}. [2]

In this diagram, the metal contacts are represented by their Fermi levels, and the semiconductor by its valence and conduction bands. In Figure 1.1a, at short circuit conditions, there is no applied voltage and therefore no net current flow under dark conditions. The difference in the two metal contact's work functions gives rise to a built in electric field distributed evenly throughout the device. Under illumination, photogenerated charges move in response to this built in electric field: the electrons drift the lower work function metal and the holes to the higher. This creates a short circuit current, I_{sc}, that flows out into the external circuit. In Figure 1.2b, at open circuit conditions, the voltage across terminals, V_{oc} corresponds to the difference the work functions of the metal and balances the internal electric field, resulting in no net current flow. Under reverse bias, the photogenerated charges drift under stronger electric fields to their contacts, resulting in higher reverse currents, and under forward biases higher than

V_{oc} the contacts efficiently inject charges into the semiconductor. Normal solar cell operation corresponds to forward bias conditions in which the terminal voltage is less than V_{oc}. The current-voltage characteristics for these different regimes are shown in Figure 1.2:

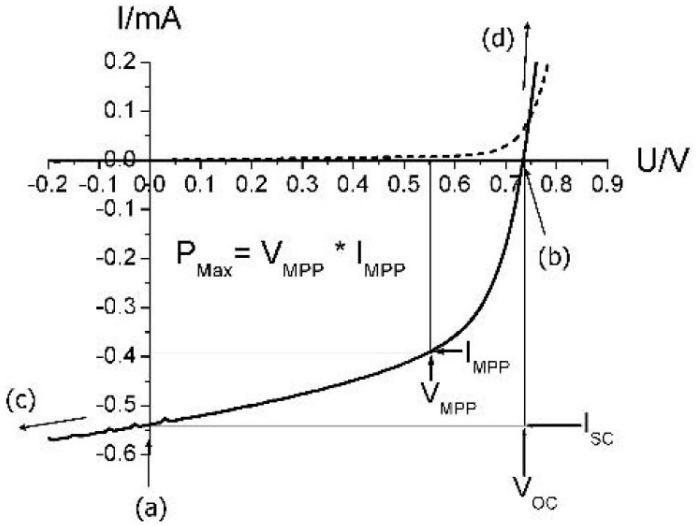

Figure 1.2: Current-voltage (I-V) curves of a solar cell under dark (dashed) and light (solid) conditions. The different points are labeled with their corresponding diagrams (a-d) from Figure 1.1. [2]

The operating regime of a solar cell is over the voltage range from 0 V to V_{oc}, in which the illuminated cell delivers power to the external circuit. Power reaches a maximum at some point along the curve. The efficiency of a solar cell is defined as the power density at this point as a fraction of the incident photon energy and can be expressed in terms of the V_{oc} and I_{sc}:

$$\eta = \frac{V_{MPP} I_{MPP}}{P_{incident}} = \frac{FF \cdot V_{oc} I_{sc}}{P_{incident}} \qquad (1.1)$$

in which FF, the fill factor, is defined as $\frac{I_{MPP} V_{MPP}}{I_{sc} V_{oc}}$. These three parameters, the fill factor, open circuit voltage and short circuit current, are the primary performance characteristics for solar cells and are greatly influenced by the material parameters of the cell's semiconductor, particularly the carrier mobility and recombination rate.

The ability of semiconducting organic materials to transport electric current and absorb light is due to the $sp^2 + p_z$ orbital hybridization of their carbon atoms. The electron in the p_z

orbital of one carbon atom will form π bonds with neighboring p_z electrons of adjacent atoms, leading to an alternating single and double bond structure [2, 5, 6]. These π electrons are delocalized, allowing for charge transport in these organic materials. Incident light can excite an electron to the lowest unoccupied molecular orbital (LUMO), leaving a hole in the highest occupied molecular orbital (HOMO). These orbitals are analogous to the conduction and valence bands in inorganic semiconductors. After the photogeneration of charges, the electron and hole remain Coulombically bound as an exciton in organic materials, unlike in many inorganic semiconductors such as Si. These excitons possess binding energies much greater (0.1 – 1 eV) than the thermal energy *kT* and cannot be dissociated by the electric field created by two asymmetric electrodes [7, 8]. Therefore, researchers began to use two different materials with different HOMO and LUMO energy levels to create an interface where the photogenerated exciton could dissociate into separate charge carriers and travel to their contacts [9]. In most OPV systems, the electron donating material is a π-conjugated polymer and the accepting material is a chemically modified fullerence, although other small molecule and polymer electron accepting materials have been reported [10-12]. The most common pair of electron donating and accepting materials is the polymer poly(3-hexylthiophene) (P3HT) and the modified fullerene [6,6]-phenyl C_{61}-butryic acid methyl ester (PCBM) or [6,6]-phenyl C_{71}-butryic acid methyl ester. Their chemical structures are shown in Figure 1.3. The P3HT employed is usually regioregular, which results in a much more ordered phase of the polymer with higher charge carrier mobilities compared to regiorandom P3HT, which typically results in amorphous films or domains [13, 14].

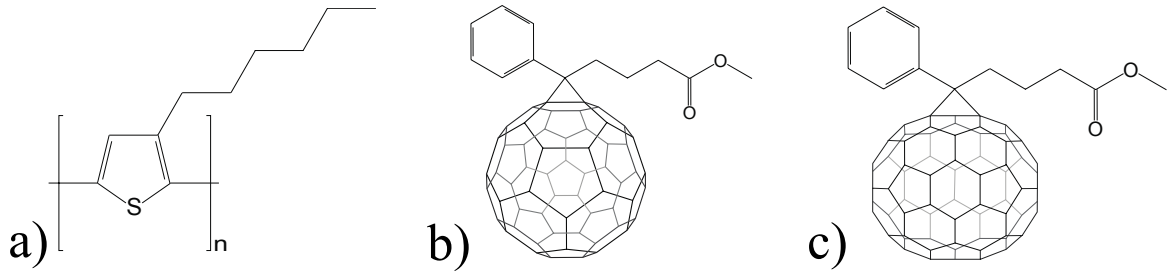

Figure 1.3: The chemical structure of a) P3HT, b) PCBM, and c) $PC_{71}BM$

1.2 OPV Device Operation

Due to their large binding energy, photogenerated excitons within organic materials must diffuse to the electron donor / acceptor interface in order to dissociate into separate charge carriers. However, the exciton diffusion length in organic materials is small when compared to their absorption length. Typically, the diffusion length is 10-50 nm in polycrystalline and amorphous organic films and only 5-8 nm in conjugated polymer systems[15, 16]. The morphology at these length scales must therefore be finely controlled in order to fabricate high efficiency devices.

Researchers initially used a bilayer device configuration, in which the donor and acceptor materials are placed in sequential layers and the exciton dissociation occurs at the planar interface between the two. The schematic energy level diagram of this system is shown in Figure 1.4.

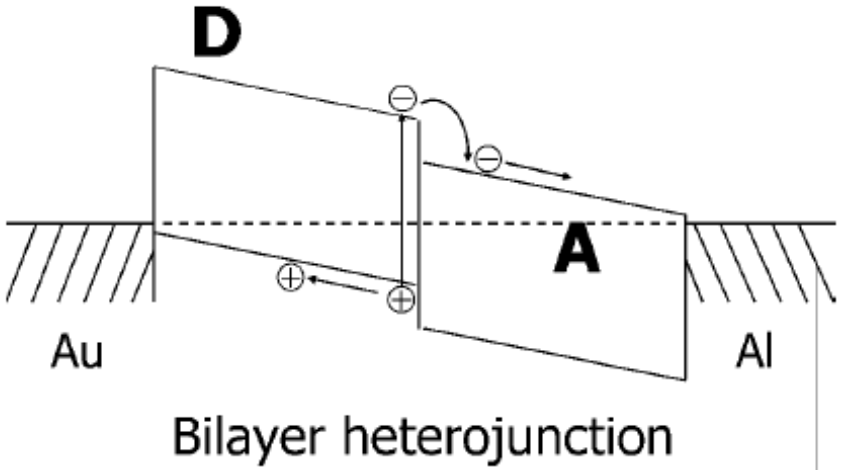

Figure 1.4: Schematic of a bilayer heterojunction device. Photogenerated excitons can only be separated in a thin layer adjacent to the interface.[2]

The bilayer device is sandwiched between two electrodes with work functions closely matching the donor HOMO and acceptor LUMO for efficient charge extraction. One advantage of the bilayer structure is the monomolecular charge transport. After the excitons are dissociated, the electrons travel in the n type acceptor material, and the holes within the p type donor material, under influence from the electric field generated by the two asymmetric electrodes. The two charge carriers are effectively separated as they travel to the electrodes, limiting recombination within the device. However, only photons absorbed within one exciton diffusion length of the donor/acceptor interface have the potential to be dissociated. These structures could therefore never operate at efficiencies much greater than 1% due to the large number of photogenerated excitons that recombine away from the interface [17].

In order to increase the efficiency of OPV cells made with these materials, it is necessary to increase the fraction of excitons which reach the donor/acceptor interface. This can be most easily achieved by increasing the interfacial surface area. For example, diffuse bilayer devices allow the two layers to slightly interpenetrate through controlled annealing, lamination, or using a solvent that partially dissolves the previously deposited layer [2, 18]. The logical extension to this need to maximize the interfacial area was first reported by *Yu et al*. in 1995 and termed a bulk heterojunction (BHJ) [19]. A BHJ is an interpenetrating blend of electron donating and accepting semiconducting materials within the same matrix. Ideally, the two materials are mixed well enough so that each donor/acceptor interface is less than one exciton diffusion length away from any other. The schematic energy level diagram of this system is shown in Figure 1.5.

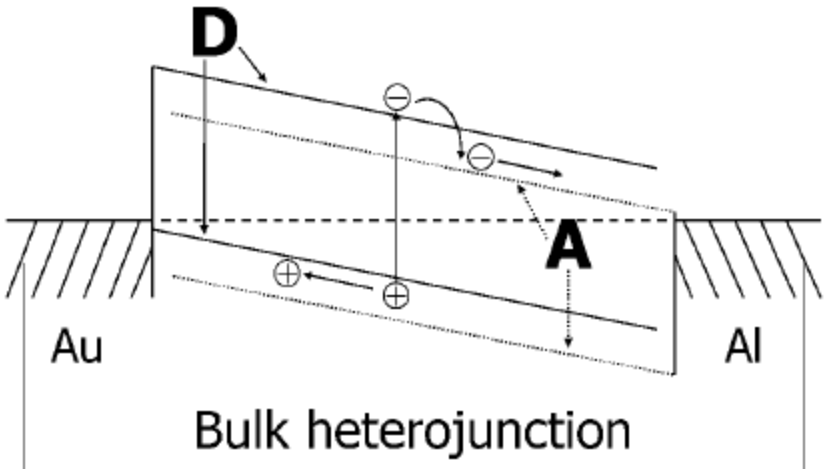

Figure 1.5: Schematic of a bulk heterojunction device. Photogenerated excitons can be dissociated into charges at any point within the film.[2]

The dissociated charges must then diffuse to their respective contacts via continuous paths of pure domains of electron donor or acceptor materials to their respective contacts. Typically, however, the BHJ network is not completely bicontinous or interpenetrating, and numerous 'islands' of one material domain exist in which one carrier type can be isolated, eventually recombining without exiting the device. In addition, the electron accepting (donating) material may contact the anode (cathode) where holes (electrons) are collected, leading to high recombination of carriers at the contacts. Often, carrier transport layers, which block the transport of one carrier type while facilitating the other, are placed as buffer layers between the BHJ and the contacts when fabricating an OPV device.

1.3 Recombination Mechanisms

Using a detailed balance approach, Shockley and Quiesser showed that the open circuit voltage of a solar cell is highest when charges recombine only radiatively [20]. However, in organic BHJ cells, most recombination mechanisms are nonradiative [21]. Therefore, there is a strong incentive to limit non-radiative recombination mechanisms in OPV cells to increase their device efficiency. These mechanisms can be broadly divided into monomolecular and bimolecular recombination, which are defined here as any first or second order process

determined by the light intensity dependence. Monomolecular recombination typically refers to either geminate recombination or Shockley-Read-Hall (SRH) recombination. Geminate recombination, which involves a single electron-hole pair which originated from a single incident photon, has been shown to be non-dominant in P3HT:PCBM solar cells [22]. SRH recombination is a first order process in which one electron and one hole recombination through a trap state [23]. Trap states can be introduced into polymer:fullerene BHJ through impurities in the fullerene or interfacial defects between the two materials that function as traps. One carrier type is preferentially trapped quickly, creating a reservoir of stationary trapped charges in which the other, more mobile carrier can recombine. The SRH recombination rate is therefore a first order process described as: $R_{SRH} \propto n_{trap} \cdot n_{mobile}(I)$, where I is the incident light intensity. Monomolecular recombination can also originate if significant charge carrier concentration gradients exist within the BHJ solar cell [22]. Near the electrodes, one carrier type will be at a much greater concentration, therefore only the minority carrier concentration will drive the recombination rate.

Bimolecular recombination is the recombination of a free hole with a free electron as they travel from their separation point to the contact, and is therefore dependent on both carrier populations. The bimolecular recombination rate can be descried as: $R_{BI} = \beta n_h(I) \cdot n_e(I)$, where β is the bimolecular recombination coefficient. There exists a special case of bimolecular recombination known as Langevin-type, in which the recombination rate is dependent on the mobilities of the charge carriers. In a disordered semiconductor, the bimolecular recombination rate is limited by the rate at which oppositely charged carriers find each other. The faster the carriers move, the faster they find each other, therefore the bimolecular recombination rate should be proportional to the charge carrier mobilities [24]. In Langevin-type recombination, the recombination coefficient is given by:

$$\beta_L = \frac{q(\mu_n + \mu_p)}{\varepsilon_r \varepsilon_0} \qquad (1.2)$$

where μ is the carrier mobility, q is the elementary charge, and ε is the dielectric constant of the semiconductor [25]. Although the presence of Langevin recombination has been observed in a variety of OPV systems, the strength of this mechanism is often suppressed, particularly in P3HT:PCBM [26-29].

However, the recombination behavior in organic BHJ systems has not been completely explained. Even in P3HT:PCBM OPV cells, mutually contradictory explanations for their current-voltage characteristics based on monomolecular [23, 30-32] and bimolecular [27, 33-35] recombination behavior have been proposed. Additionally, recombination within OPV devices may operate as some combination of these different mechanisms, or the dominant mechanism may change with respect to applied bias and incident light intensity. In order to answer these questions, researchers have developed a variety of techniques to probe charge transport material properties in organic BHJ materials.

1.4 Organic BHJ Materials Characterization Techniques

In order for OPV cells to effectively compete with other solar technologies, an improvement in their PCEs to more than 15% and a significant extension of their operating lifetime are necessary [8, 36, 37]. An improved understanding of the materials science, particularly the charge transport and recombination behavior, of OPV materials is required for addressing both of these issues.

Carrier mobility is one of the key parameters of interest towards improving device performance. Mobility within a BHJ system strongly depends on the purity and nanomorphology of the material network and can vary significantly between electrons and holes. The large mobilities (> 1 cm^2/Vs) of inorganic semiconductors is determined by Hall effect measurements, however this technique is not applicable to low mobility ($\leq 10^{-3}$ cm^2/Vs) polymer:fullerene BHJ materials [38]. The most common methods for measuring mobilities in BHJ systems are transient techniques such as the time-of-flight method and photoinduced charge extraction by a linearly

increasing voltage (photo-CELIV) on vertical solar cell structures, and mobility calculations from organic field effect transistor (OFET) measurements.

Time-of-flight (TOF) is based on the measurement of the carrier transit time (τ) of a population of photogenerated carriers. A sample is sandwiched between two electrodes, one of which is transparent. The electrodes are held at a constant voltage and the sample is excited via pulsed laser shone through the transparent electrode [39, 40]. Charge carriers are generated adjacent to the transparent electrode and drift as a sheet towards the other electrode. The transit time (τ) is defined as the time the band of charge carriers needs to travel through the sample and is measured from the transient photocurrent from the device. Mobility is calculated from τ, the thickness of the film, and the applied voltage [38]. Electron and hole mobilities can be measured separately by changing the bias configuration of the two electrodes [28, 40]. The transient photocurrent can also indicate the presence of deep trap states within the material. However, TOF measurements become difficult at high mobilities, as the short drift time overlaps with the noise of the initial excitation. In highly dispersive or disordered media, the photoinduced carriers do not travel uniformly to the electrode and the transient photocurrent is a simple exponential decay, making it very difficult to determine τ. High charge carrier concentrations within the sample also affect the drift velocity of the photogenerated charges and make accurate mobility measurements difficult. Finally, in TOF experiments, relatively thick samples of 5-20 μm are favorable in order to constrain the absorption depth so that it is much smaller than the total film thickness. These sample thicknesses are much larger than the typical thickness ($\leq$ 100 nm) of the active material in an OPV cell.

Charge extraction by linearly increasing voltge (CELIV) is a very popular technique for both organic and inorganic semiconductors [25, 41-44] and has important advantages over the TOF technique. In the CELIV technique, a linearly increasing voltage is applied one electrode and the resulting current transient from the extracted equilibrium charge carriers is used to calculate the mobility [38]. The carrier mobility is calculated from the time to the peak transient

photocurrent, the device thickness, and the voltage rise speed. Unlike in TOF experiments, there is no need to have a very optically thick sample, so CELIV measurements can be performed on very thin film OPV cells. Material systems with highly dispersive transport and high conductivities can also be studied. The main limitation of CELIV is that there is no way to distinguish electron and hole mobilities in ambipolar materials. A light pulse can also be applied before the carrier extraction (photo-CELIV) to increase the carrier concentration and measure the relaxation process of the photogenerated carriers [43]. By varying the time between the light pulse and carrier extraction, it is possible to estimate the carrier lifetime and calculate a recombination constant of the material [24, 29, 45]. An example CELIV transient with differentiated electron and hole mobilities is shown in Figure 1.6, with the applied voltage in the inset.

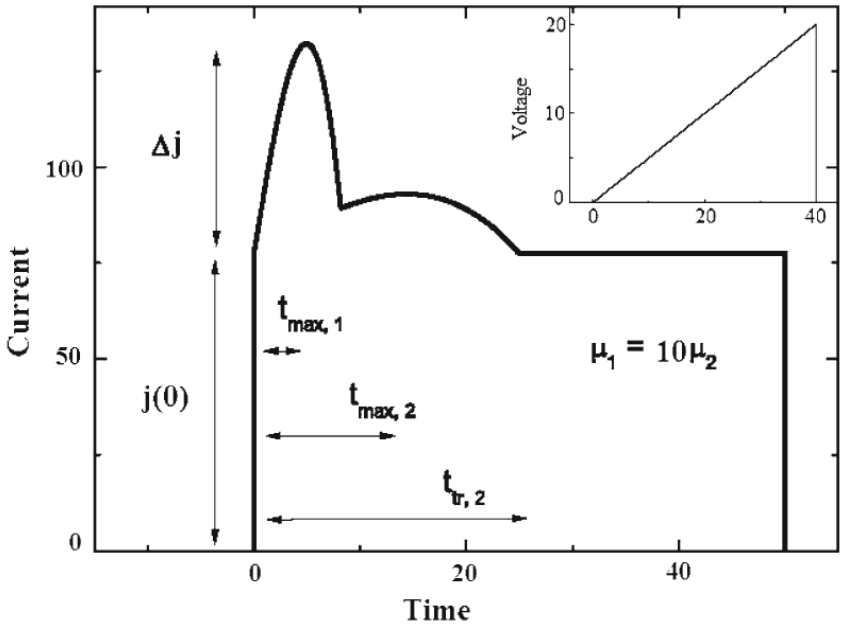

Figure 1.6: Transient current measurements from a CELIV experiment in which one carrier mobility is 10 times larger than the other. j(0) is the displacement current, while Δj is the current due to transported equilibrium charge carriers. The two peak times for the transient hole and electron photocurrents ($t_{max,1}$ and $t_{max,2}$). [38]

Although the difference in the two mobilities can be seen, there is no obvious way of determining which carrier is faster without other measurement techniques.

Organic semiconductors have been employed in a variety of electron applications besides solar cells, including field effect transistors (FET). The methods for determining field effect mobility from Id-Vg measurements are well understood and applicable to organic materials (OFETs) [46, 47]. An organic BHJ can therefore be fabricated in a FET configuration and operated in the linear and saturation regimes to calculate the field effect mobility from the following equations. In the linear regime:

$$I_D = \mu C \frac{W}{L}\left((V_{GS} - V_{th})V_{DS} - \frac{1}{2}V_{DS}^2\right) \quad (1.3)$$

And saturation regime:

$$I_D = \mu C \frac{W}{2L}(V_{GS} - V_{th})^2 \quad (1.4)$$

For ambipolar materials, the BHJ OFET can be operated in both n-FET and p-FET modes to calculate the mobilities of both charge carriers. In OFETs, the charges move within a narrow channel at the interface between the organic semiconductor and the gate dielectric. Charge transport is therefore highly sensitive to structural defects of the organic layer and dielectric at their interface, as well as the presence of traps at the interface. Calculated linear and saturation mobilities are not consistent due to the different electric field distributions in each mode. The mobility can also vary by gate voltage due to the presence of traps or from the mobility's dependence on the carrier concentration, which is modulated by V_G. FETs also typically operate with much microscopic higher carrier densities (> 10^{18} cm^{-3}) compared to solar cells, for which the carrier density is < 10^{17} cm^{-3} for 1-sun illumination levels.

Measurement techniques used to probe nongeminate recombination losses in BHJ OPV devices are equally varied; including charge extraction [48, 49], transient photoconductivity [50], impedance spectroscopy [51, 52], and intensity dependent measurements of cells operated close to V_{oc} and J_{sc} [24, 34, 35]. The simplest and most common method used to distinguish

bimolecular from trap-assisted recombination is measuring the V_{oc} dependence on incident light intensity. *Koster et al.* showed that the dependence is described by the relation:

$$V_{oc} = \frac{E_g}{q} - \frac{k_B T}{q} ln\left(\frac{N_{cv}^2}{n_e n_h}\right) \tag{1.5}$$

where E_g is the difference between the HOMO of the donor and LUMO of the acceptor, N_{CV} is the effective density of states in the donor and acceptor, and n_e and n_h are the dissociated carrier densities which vary with the incident light intensity [24, 53]. The V_{oc} of OPV cells in which the BHJ material is dominated by trap-free bimolecular recombination will therefore have a simple $\frac{k_B T}{q}$ dependence on the light intensity. When trap-assisted recombination is present, a higher slope will be observed, as shown in the case of P3HT in Figure 1.7.

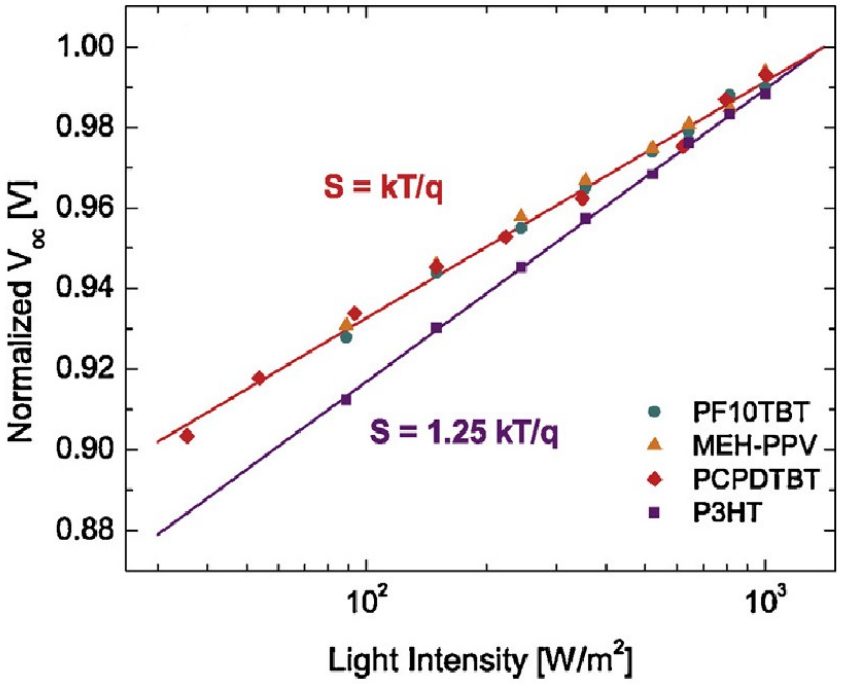

Figure 1.7: Normalized V_{oc} vs. light intensity for four polymer:fullerene systems. Three polymer:fullerene systems are dominated by bimolecular recombination, while the higher slope of the P3HT:PCBM device dependence indicates the presence of both trap-assisted and bimolecular recombination. [24]

Bimolecular recombination coefficients are calculated from the charge carrier concentrations measured using CELIV or charge extraction techniques close to V_{oc}. Away from

the open circuit condition, the nature of the recombination is usually determined from the relationship between J_{sc} and the incident light intensity, $J_{SC} \propto I^{\alpha}$. If α is much less than 1, this is indicative of strong bimolecular recombination [34]. A simple linear dependence is less clear but can be indicative of monomolecular recombination if the photogenerated carrier density is much larger than the dark carrier density [35, 54].

Although the above described techniques have generated a significant amountof information on transport and recombination within BHJ solar cells, more work is necessary to accurate characterize transport phenomena. We have developed a variety of novel experimental techniques utilizing lateral devices in order to characterize these materials and address these questions.

Chapter 2: Lateral Device Physics

2.1: Introduction

Due to the disordered and complex nature of organic bulk heterojunction (BHJ) materials, their photovoltaic performance is highly dependent on their nanoscale morphology, which can be affected by a variety of factors including the chemical structure of the organic semiconductors, the solvent and solvent additives, fabrication methodology, and environmental exposure. New measurement techniques and tools are needed to clarify the interaction between these factors affecting the morphology and the materials' electronic properties; such as the carrier mobilities, charge concentrations, and recombination rate constants. To study these properties, researchers have typically utilized vertical BHJ structures similar or equivalent to an OPV cell. A variety of techniques based on these vertical structures, including time-of-flight and photo-CELIV described in Chapter 1, as well as impedance spectroscopy [55, 56], time resolved terahertz spectroscopy [57], time resolved microwave conductivity [58], and dark-injection space charge limited current (DI-SCLC) [59], have been successfully employed by many research groups. To complement these studies, we have developed techniques that measure the transport and recombination properties of organic BHJs along the in-plane axis, or lateral direction. Schematic diagrams of a vertical and lateral structure are shown in Figure 2.1:

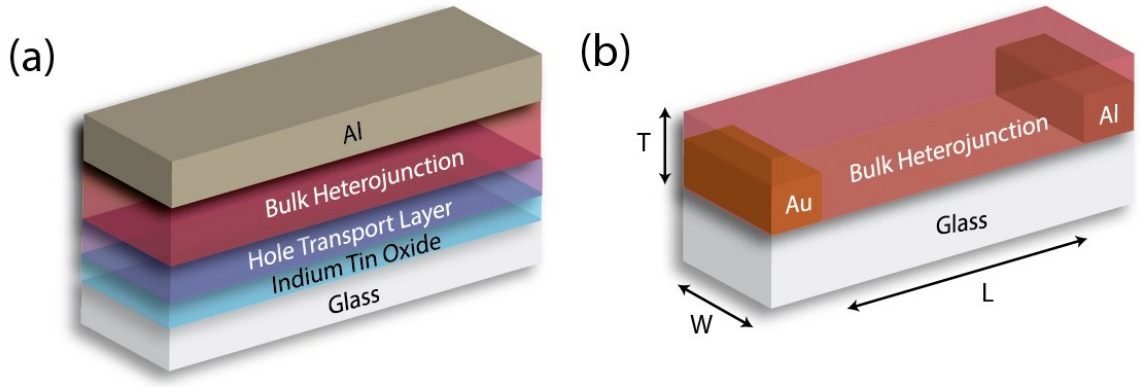

Figure 2.1: a) Structure of a conventional, bottom illuminated vertical OPV cell. b) Structure of a lateral BHJ device illuminated from the top. Device width (W), length (L), and semiconductor thickness (T) are labeled.

*Contains material previously published in References [64, 70, 71]

The conventional vertical cell is bottom illuminated through a transparent substrate and electrode. The transparent electrode is usually a high work function oxide such as indium tin oxide (ITO) and operated as the anode. To prevent recombination at the anode, an optically transparent hole transport layer (typically made of the polymer PEDOT:PSS) is deposited via a solution coating technique to a thickness of 10-100 nm. The BHJ active layer is also deposited from solution (via spin coating, inkjet printing, doctor blading, etc.) to a thickness of 50-200 nm. Lastly, a low work function metal such as aluminum is deposited on top as the cathode. These devices can be operated as OPV cells or used in the materials characterization techniques listed previously.

In a lateral BHJ device, the two electrodes are defined on the same plane and the BHJ material is deposited from above. One electrode is made of a high work function metal such as gold, and the other a low work function metal such as aluminum. The photoactive region, defined by the channel between the two electrodes, is illuminated from above to achieve uniform charge generation throughout the device. This configuration is a poor geometry for OPV efficiency but is a useful platform for materials diagnostics. Key charge transport and recombination parameters in organic BHJ systems can be anisotropic. This is particularly true for some of the materials that are in use in high efficiency solar cell devices. While values of these parameters along the direction of charge transport in solar cells are especially important, it is also very useful to study the values of these parameters in a perpendicular direction. We note that while carrier densities and recombination coefficients are scalar quantities, their experimentally determined values depend on the direction of charge flow during a measurement. It is therefore important to measure such parameters along multiple directions. Lateral devices can also be measured under steady state, rather than transient, light conditions; more similar to OPV cell operation. In addition, lateral BHJ devices allow for these types of measurements over a wide range of length scales (from 10s of nm to 100s of μm), are more amenable to device modeling

due to their uniform photogeneration profile, and permit direct access to the active layer for spatially resolved measurements.

2.2 Unipolar Lateral Device Modeling

The device physics of lateral BHJ devices are a combination of photovoltaic and photoconductor physics as a result of the device geometry and mode of electrical operation. Under illumination, lateral BHJ devices are analyzed under high reverse bias in order to simulate the direction and magnitude of the electric field within an OPV cell under operation. The efficiency of photocurrent generation depends on the processes of charge generation, recombination, and transport. Assuming non-injecting contacts, the photocurrent becomes saturated when all photogenerated carriers are extracted from the semiconductor [60]. This implies that the electron and hole drift lengths are greater than or equal to the device thickness L. With no recombination, the saturated photocurrent density is simply given by:

$$J_{ph}^{sat} = qGL \tag{2.1}$$

where G is the generation rate and q is the fundamental charge [60]. However, if the carrier drift lengths are smaller than L, space charge will form and recombination becomes significant. Suppose that we have a strongly imbalanced material system, in which the drift length for holes, λ_h, is much shorter than L and the drift length for electrons, λ_e. Holes accumulate in the device near the anode and are not neutralized by an equal density of electrons, which results in a buildup of space charge and distorting the applied electric field. Under steady state conditions, the electric field increases in this region, enhancing the extraction of holes so that the external hole current equals the external electron current. This is shown schematically in Figure 2.2 below in the region L_1.

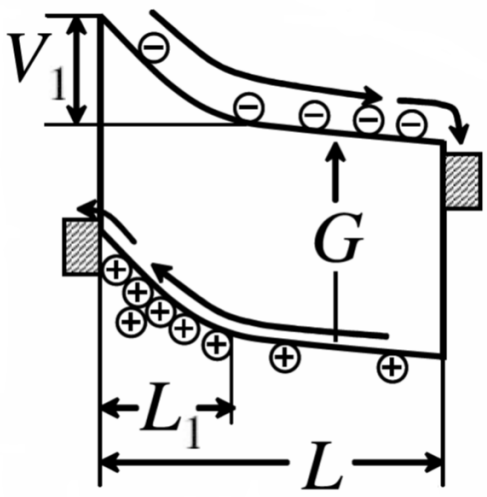

Figure 2.2: Schematic energy level diagram of a photovoltaic device under illumination, in which $\mu_h << \mu_e$. [61]

The length of region L_1 is given by the mean hole drift length and limits the saturated photocurrent to $J_{ph}^{sat} = qGL_1$. Goodman and Rose determined that there is a fundamental limit for the buildup of space charge, reached when this saturation photocurrent is equal to the space-charge limited current:

$$J_{SCL} = \frac{9}{8}\varepsilon\mu_h \frac{V_1^2}{L_1^3} \tag{2.2}$$

therefore

$$J_{ph} = \left(\frac{9}{8}\varepsilon\mu_h\right)^{\frac{1}{4}} (qG)^{\frac{3}{4}} V_1^2 \tag{2.3}$$

where ε is the dielectric constant of the BHJ layer and V_1 is the voltage across the region L_1, which can be very close to the total applied voltage [60, 61]. Space charge limited (SCL) photocurrent is distinguished by the dependence on the square root of the applied voltage and the slowest charge carrier mobility. SCL behavior is also expected in lateral BHJ devices due to their long channel lengths and uniform illumination across the channel, as well as the unbalanced transport, high charge carrier generation, and low mobilities in organic BHJ materials. SCL photocurrents have been previously observed in organic BHJ materials from vertical OPV measurements [61], but we need to derive the equivalent of Equation 2.3 for the lateral geometry.

To this end, we numerically simulated a 5 μm channel length lateral BHJ device with mobilities typically found in P3HT:PCBM blends: hole and electron mobility values of 10^{-4} and 10^{-5} cm^2/Vs, respectively [62]. The device was simulated under an applied reverse bias field of -100 V and under AM1.5 illumination. Modeling treated the BHJ as a composite semiconductor with fixed mobilities and homogeneous carrier photogeneration throughout the device independent of the electric field strength. Charge carrier and electric field profiles of lateral devices are developed from a system of equations consisting of the drift-diffusion equation for electrons and holes, the steady state continuity equation, and Poisson's equation for electrostatics:

$$J_{ph,p} = e\mu_p p(x)E(x) - \mu_p kT\frac{dp(x)}{dx} \tag{2.4}$$

$$J_{ph,n} = e\mu_n n(x)E(x) + \mu_n kT\frac{dn(x)}{dx} \tag{2.5}$$

$$\frac{dJ_{ph,p}}{dx} = -\frac{dJ_{ph,n}}{dx} = eG - eR(x) \tag{2.6}$$

$$-\frac{d^2\phi}{dx^2} = \frac{e}{\varepsilon}[p(x) - n(x)] \tag{2.7}$$

where $J_{ph,n,p}$ are the photogenerated electron and hole current densities, $n(x)$ and $p(x)$ are the photogenerated electron and hole concentrations, $\mu_{n,p}$ are the electron and hole mobilities, ϕ is the electric potential, E is the electric field, G is the generation rate, and $R(x)$ is the recombination rate, which is modeled as bimolecular with a fixed coefficient of $\beta = 10^{-12}\ cm^3/s$ [62]. A generation value of $G = 10^{21}\ m^{-3}s^{-1}$ was assumed to represent typical light intensities under AM1.5 illumination. Electrical contacts in this device model are considered to be non-injecting and with no barrier for charge extraction. Carrier traps and trap-assisted recombination mechanisms are also not included in the model.

This system of equations was solved in 1-dimension and used to generate carrier concentration, electric field, potential, and recombination profiles across the simulated 5 μm lateral BHJ device. These profiles are shown Figure 2.3.

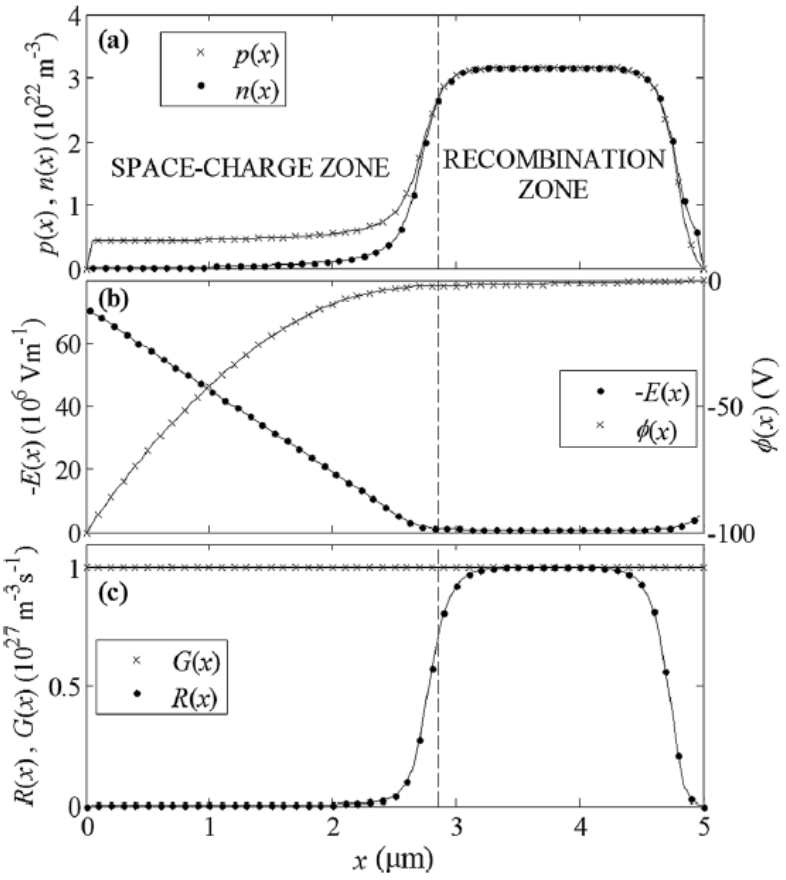

Figure 2.3: Plots of (a) photogenerated hole and electron concentrations, (b) electric field and potential profiles, and (c) recombination and generation rate profiles from a numerically simulated illuminated lateral BHJ device with imbalanced mobilities. [62]

The device can be divided into two distinct zones: (1) a space charge region (SCR), with excess hole concentrations due to lower hole mobility, and (2) a recombination zone, where both carrier concentrations are high but equal such that recombination exactly negates photogeneration. The electric field decreases linearly within the SCR and the majority of the applied bias is dropped across this region. There is negligible recombination within the SCR due to the imbalanced carrier concentrations. The recombination zone has a constant small, but non-zero, electric field. From integrating the electric field over the device length and using the continuity and Poisson's equation, we can solve for the length L_1 of the space charge region:

$$L_1 = \left(4\varepsilon\mu_p\right)^{\frac{1}{4}}(eG)^{-\frac{1}{4}}(V + E_r d)^{\frac{1}{2}} \tag{2.8}$$

where E_r is the recombination zone electric field and d is the total channel length of the device [62]. The SCL photocurrent is therefore:

$$J_{ph} = eGL_1 = \left(4\varepsilon\mu_p\right)^{\frac{1}{4}} (eG)^{\frac{3}{4}} (V + E_r d)^{\frac{1}{2}} \quad (2.9)$$

If the recombination zone field is small and the channel length is short, then Equation 2.9 reduces to:

$$J_{ph} = \left(4\varepsilon\mu_p\right)^{\frac{1}{4}} (eG)^{\frac{3}{4}} V^{\frac{1}{2}} \quad (2.10)$$

which is the equivalent expression as Equation 2.3 for the lateral geometry case. Using Equation 2.10, it is possible to calculate the slower carrier mobility from the SCL photocurrent behavior of small lateral BHJ devices.

2.3 Ambipolar Lateral Device Modeling

Unlike in vertical OPV devices, lateral BHJ devices also exhibit SCL photocurrent behavior in systems with equal electron and hole mobilities. If the channel length of the device is longer than both carrier drift lengths, there will be a buildup of positive space charge near the anode due to accumulating holes and a buildup of negative space charge close to the cathode. Holes generated near the cathode and electron generated near the anode will migrate to the center of the device, where carrier concentrations are high and under equilibrium. Under steady state operation, the device will therefore be divided into three distinct regions: (1) a space charge region (SCR) adjacent to the anode with excess hole concentration, (2) a central recombination zone, in which all photogenerated carriers recombine, and (3) a SCR adjacent to the dcathode with excess electron concentration [63]. When the applied electric field is increased, a larger amount of space-charge can accumulate, increasing the size of the SCRs and causing the recombination zone to contract [63]. This three zone model is supported by simulations of a 10 μm lateral BHJ device with equal electron and hole mobilities of 10^{-3} cm^2/Vs. These simulations were generated using the same procedure described above from solving the system of Equation

2.4-2.7 and assumed the same generation and recombination rates. The resulting carrier concentration, electric field, potential, and recombination profiles are shown in Figure 2.4.

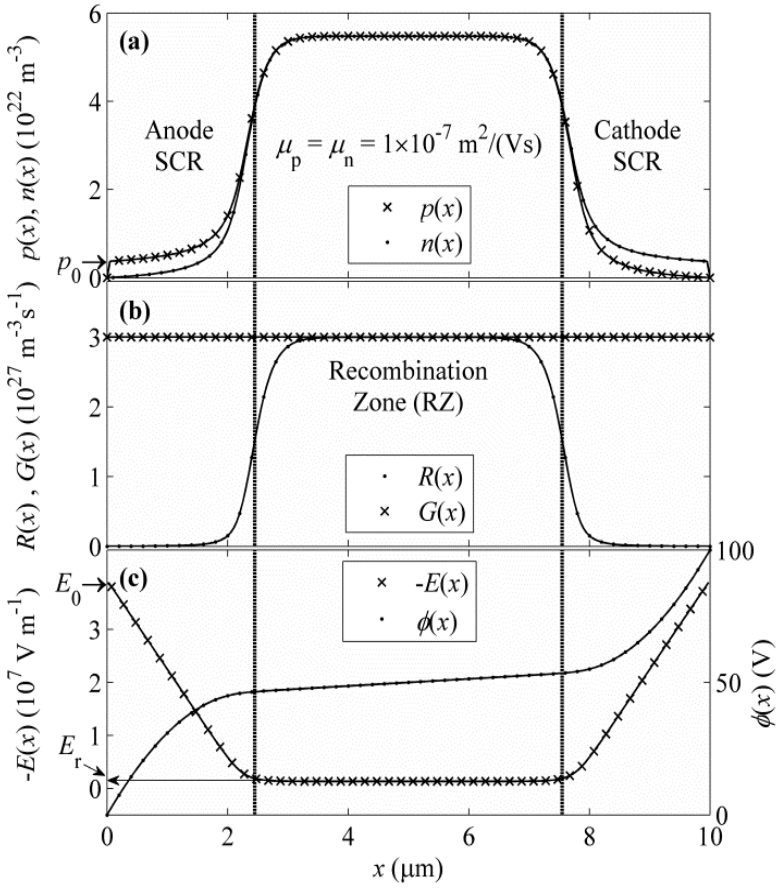

Figure 2.4: Plots of (a) photogenerated hole and electron concentrations, (b) recombination and generation rate profiles, and (c) electric field and potential profiles from a numerically simulated illuminated lateral BHJ device with equal mobilities. [63]

This three zone model has been confirmed using spatially resolved measurements of the photocurrent density [64, 65] and electric field strength [66, 67]. The electric field within both SCRs increases linearly and majority of the applied voltage is dropped across the two SCRs, with a small but nonzero recombination zone field. The voltages across both SCRs and the sizes of the two SCRs are equal due to the equal carrier mobilities. While the actual size of the SCRs is dependent on the generation rate, mobility, and applied electric field, their relative sizes are

related to the mobility through a simple relation derived from the continuity equations. Within the recombination zone, the hole current is given by:

$$J_p = q\mu_p E_r p_{equil} \tag{2.11}$$

where p_{equil} is the hole concentration in the recombination zone. The hole current extracted from the anode SCR is given by:

$$J_p = -qGL_A \tag{2.12}$$

where L_A is the length of the hole dominated SCR adjacent to the anode. Equivalent equations can be written for the electron dominated SCR with length L_C adjacent to the cathode and recombination zone electron concentration n_{equil}. From the charge continuity equation:

$$\frac{-qGL_C}{-qGL_A} = \frac{q\mu_p E_r p_{equil}}{q\mu_n E_r n_{equil}} \quad \Rightarrow \quad \frac{L_C}{L_A} = \frac{\mu_p}{\mu_n} \tag{2.13}$$

since electron and hole concentrations are equal in the recombination zone. As expected, the slower carrier builds up more space charge and occupies a larger SCR within a material system with imbalanced mobilities. By measuring the lengths of the SCRs, one can therefore distinguish the slower carrier and measure the mobility ratio even in an organic BHJ system with very similar carrier mobilities. We will discuss the relationship between the voltage across each SCR and the mobility ratio in the next chapter.

To calculate the carrier mobilities of an ambipolar lateral BHJ device, we derive the expression for the SCL photocurrent using the same method as for the unipolar case:

$$J_{ph} = 2eGL = 2(\varepsilon\mu)^{\frac{1}{4}}(eG)^{\frac{3}{4}}(V + E_r d)^{\frac{1}{2}} \tag{2.14}$$

where $L=L_A=L_C$ and $\mu=\mu_n=\mu_p$. If $E_r d$ is a negligible voltage drop compared to the total applied voltage, then the expression reduces to:

$$J_{ph} = 2(\varepsilon\mu)^{\frac{1}{4}}(eG)^{\frac{3}{4}}(V)^{\frac{1}{2}} \tag{2.15}$$

which is the equivalent expression as Equation 2.10 but for the ambipolar case [63]. These two equations for different mobility ratio conditions differ only by their constant coefficients. We therefore use the general equation:

$$J_{ph} = \chi\sqrt{2}(\varepsilon\mu)^{\frac{1}{4}}(eG)^{\frac{3}{4}}(V + E_r d)^{\frac{1}{2}} \qquad (2.16)$$

where χ is an ambipolarity factor that falls between 1 and $\sqrt{2}$, depending on the mobility ratio [63]. To determine the dependence of χ on the mobility ratio, simulations of lateral BHJ device behavior were run over a broad range of conditions selected to comprehensively cover typical properties of organic BHJ films. The photogeneration rates, recombination rates, and relative dielectric permittivities were varied for a range of mobility ratios between 1 and 1/10. χ was calculated from the photocurrent-voltage relationship and plotted versus the mobility ratio in Figure 2.5.

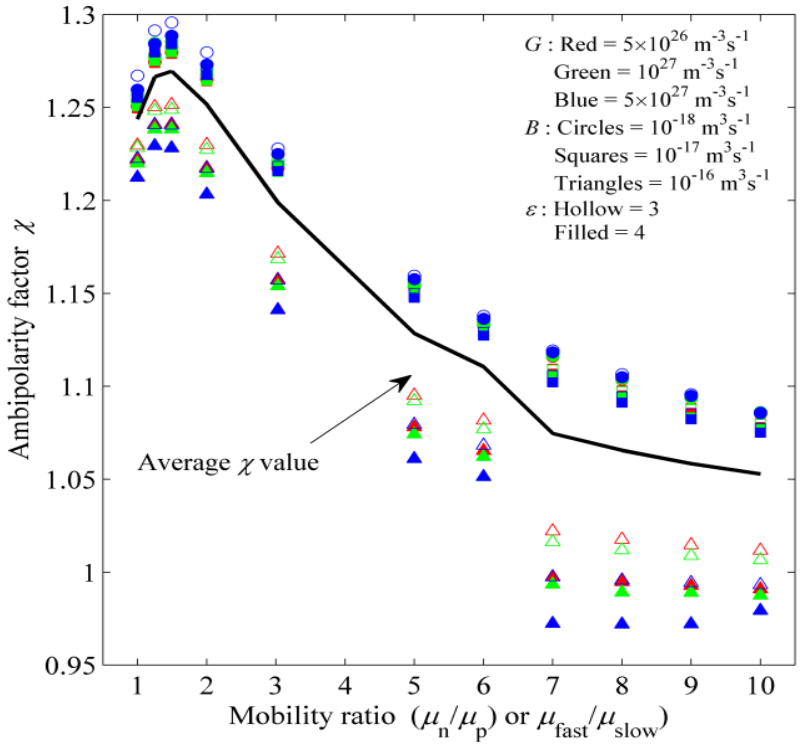

Figure 2.5: Plot of ambipolarity factor vs. mobility ratio based on 198 different simulations with different values of generation rate, recombination rate, and relative dielectric (inset). [63]

As expected, values of χ fall between 1 for the unipolar case and 1.4 for the ambipolar case. The solid line in Figure 2.5 represents an average value that can be used to estimate χ for Equation 2.16 based on knowledge of the mobility ratio.

2.4 Lateral Device Photocurrent Behavior

The SCL behavior of lateral BHJ devices has been confirmed through photocurrent measurement. Lateral BHJ devices were fabricated on a p-type silicon substrate with 2000 Å of thermally grown silicon dioxide. Asymmetric interdigitated electrodes of gold (Au) and aluminum (Al) were defined through sets of photolithography. These metals were chosen to suppress reverse bias carrier injection [68]. Each metal layer was deposited to a thickness of 500 Å. The device channel lengths ranged from 3 μm to 20 μm with a constant W/L = 1000. Before spin coating the organic BHJ layer, the substrate was dipped in a phosphoric acid solution to dissolve any aluminum oxide present on the electrodes and degreased with a solvent clean of acetone, methanol, and isopropyl alcohol. The BHJ absorber layer was deposited from a 20 mg/mL solution of P3HT:PCBM (1:1 by weight) dissolved in chloroform that had been heated and stirred at 50 °C for more than 12 h. This material is known to be close to ambipolar with a slightly slower hole mobility [68, 69]. The BHJ was spun cast on the prepared substrate at 1200 rpm for 60 s and annealed at 140 °C in a nitrogen atmosphere. The film was 220 nm thick as measured by profilometry. P3HT investigated in this work was purchased from Rieke Metals and was 90-94% regioregular (4002E). PCBM and $PC_{71}BM$ investigated in this work was purchased from American Dye Source, Inc. and had a purity >99.0%. Electrical measurements were performed in a *Desert Cryogenics* cryogenic probe station under vacuum better than 10^{-3} torr at 300 K. Electrical measurements were performed using an *Agilent 4155C Semiconductor Parameter Analyzer* and sample illumination was achieved using an *Oriel model 66912* 150 W xenon lamp. The optical spectrum was modified using an AM1.5 spectral filter and the light intensity was 100 mW/cm^2. The resulting photocurrent vs. voltage measurements are shown in Figure 2.6a.

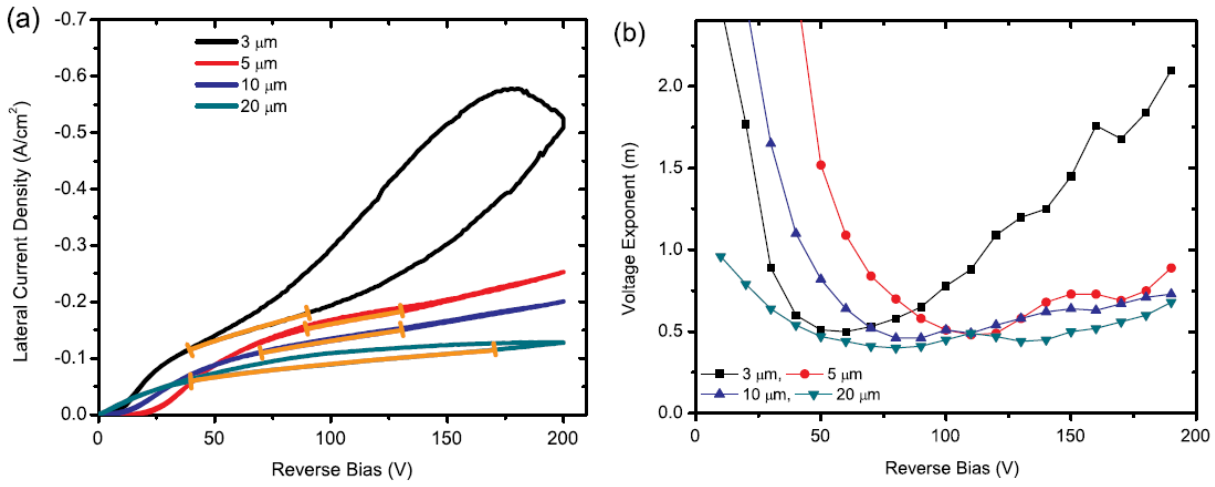

Figure 2.6: (a) Lateral photocurrent density vs. reverse bias voltage and (b) voltage exponent (m) vs. reverse bias voltage for lateral BHJ devices with channel lengths ranging from 3 μm to 20 μm under AM1.5 illumination. The orange lines in Figure 2.6a indicate the voltage range in which SCL transport is prevalent and the carrier mobility was calculated. [70, 71]

Lateral photocurrent density is defined as the difference between the dark and light currents divided by the device width and thickness. To analyze the current vs. voltage relationships, the functional form of the lateral current density was determined by finding the slope of the lateral current density vs. voltage curve on a log-log plot. This slope (m) is the functional dependence where $J_{ph}^{lat} \propto V^m$ [70, 71]. As the bias voltage increases, the voltage exponent decreases from large values of m to around 0.5. At low applied biases, this higher dependence on the voltage is due to contact resistance effects causing resistance to charge extraction [71]. Once the voltage exponent stabilizes to near 0.5, this indicates a regime where SCL photocurrent is present and Equation 2.15 is valid. With increasing bias, however, the exponent begins to increase due to the injection of charge carriers. In the non-ideal experimental situation with injection from the electrodes, carriers begins to be injected after sufficient energy barriers are overcome at high reverse biases [72]. This effect is more pronounced in smaller channel length devices where the applied electric fields are much higher. Using this voltage exponent analysis, we can fit the photocurrent vs. voltage plots to Equation 2.15 over the correct voltage range in order to calculate the SCL hole mobility. These calculated mobilities are listed in Table 2.1.

Table 2.1: Hole mobilities extracted from SCL current measurements using Equation 2.15 for various lateral BHJ device lengths. [71]

Device Length (μm)	Avg. applied bias (V)	Mobility (cm^2/Vs)
3	-65	7.0×10^{-5}
5	-110	8.2×10^{-5}
10	-100	2.7×10^{-5}
20	-105	1.9×10^{-5}

The hole mobilities calculated in Table 2.1 are in the expected range for these materials and are comparable to previous reports using SCL current and photo-CELIV methods to characterize the mobility within P3HT:PCBM OPV cells [28, 73-75]. However, there is significant variation between the calculated SCL mobilities with respect to the channel length of the lateral BHJ device. In lateral devices with longer channel lengths, $E_r d$ becomes a significant factor as the potential drop across the recombination zone becomes more significant. The total applied voltage is not equal to the voltage across the SCR and the calculated mobility is underestimated. Unfortunately, there is no way to determine $E_r d$ from only photocurrent vs. voltage measurements.

To ensure that lateral SCL measurements are consistent across different lateral BHJ devices, these photocurrent experiments were repeated using devices with much smaller channel lengths and with more imbalanced BHJ materials. Devices with channel lengths much smaller than 3 μm will be dominated by one SCR that spans the entire channel under SCL operation mode. Using electron beam lithography, interdigitated asymmetric electrodes of gold and aluminum were defined on p-type silicon substrate with 2000 Å of thermally grown silicon dioxide. The channel lengths of these devices ranged from 1 μm to 300 nm with a constant W/L = 1000. The BHJ absorber layer was deposited from a 20 mg/mL solution of P3HT:PCBM (0.5:1 by weight) dissolved in 1,2-dichlorobenzene that had been heated and stirred at 50 °C for more than 12 h. The sample was prepared and measured as described above, except at a variety of incident light intensities from 11 to 100 mW/cm^2 modulated using neutral density filters. The photocurrent and voltage exponent (m) behavior with respect to light intensity and applied voltage per unit length are shown in Figure 2.7.

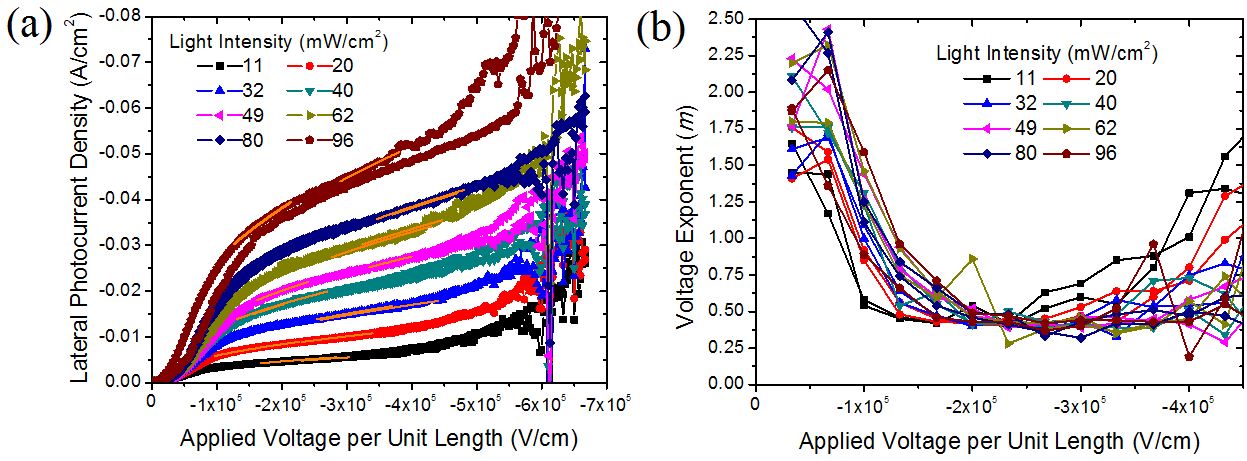

Figure 2.7: (a) Lateral photocurrent density and (b) voltage exponent (m) vs. applied voltage per unit length for a 300 nm lateral BHJ device illuminated by varying AM1.5 light intensities ranging from 11 to 100 mW/cm^2. The orange lines in Figure 2.7a indicate the range in which SCL transport is prevalent and the carrier mobility was calculated.

As the internal electric field of lateral devices can vary, we define a normalized voltage as the applied bias divided by the device length (V/L). SCL photocurrents are observed over all light intensities over a particular applied voltage per unit length range from approximately 1×10^5 to 3×10^5 V/cm. This was consistent with photocurrent measurements of larger devices with channel lengths of 1 μm and 500 nm. At lower light intensities, the SCL range shifts to lower applied biases and is over a shorter voltage range. Injection occurs at lower applied biases due to the reduced number of photogenerated carriers present within the device [71]. SCL mobilities were calculated from the photocurrent data of three devices over the intensity range, using Equation 2.10. The unipolar condition was assumed due to the relative lack of P3HT within the BHJ material, which would selectively inhibit hole transport. The mobilities are plotted versus incident light intensity in Figure 2.8.

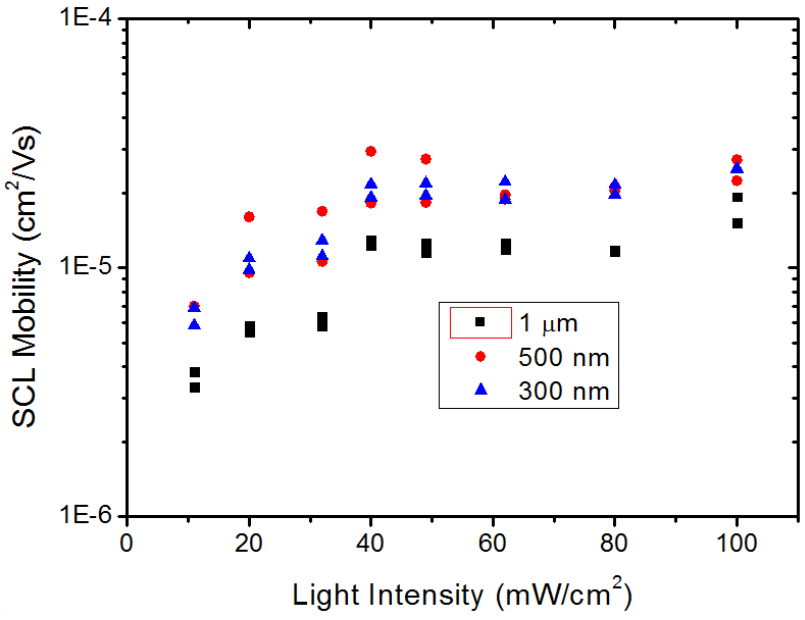

Figure 2.8: Hole mobilities calculated from lateral SCL photocurrents of three lateral BHJ devices illuminated by varying AM1.5 light intensities ranging from 11 to 100 mW/cm^2.

The calculated hole mobilities are relatively stable at high intensities and consistent between calculations from different device photocurrents. Low photogenerated carrier concentrations lead to a decrease in the mobility at the lowest light intensities. Hole mobilities are slower than those observed in the ambipolar P3HT:PCBM, which is expected given the effect of the low amount of P3HT on the nanomorphology of the BHJ material. Without an accurate measurement of $E_r d$, it is best to use small channel length devices to calculate mobilities from SCL photocurrents.

However, measuring the photocurrent from devices with a range of channel lengths can provide valuable insights into the drift lengths of BHJ materials. An important feature of lateral BHJ devices is the ease at which their channel length can be modified, which enables us to examine charge transport over a wide range of length scales. The reverse bias photocurrent vs. device length from P3HT:PCBM (from a 1:1 by weight solution) lateral BHJ devices with channel lengths ranging from 100 nm to 20 μm is shown on a log-log scale in Figure 2.9.

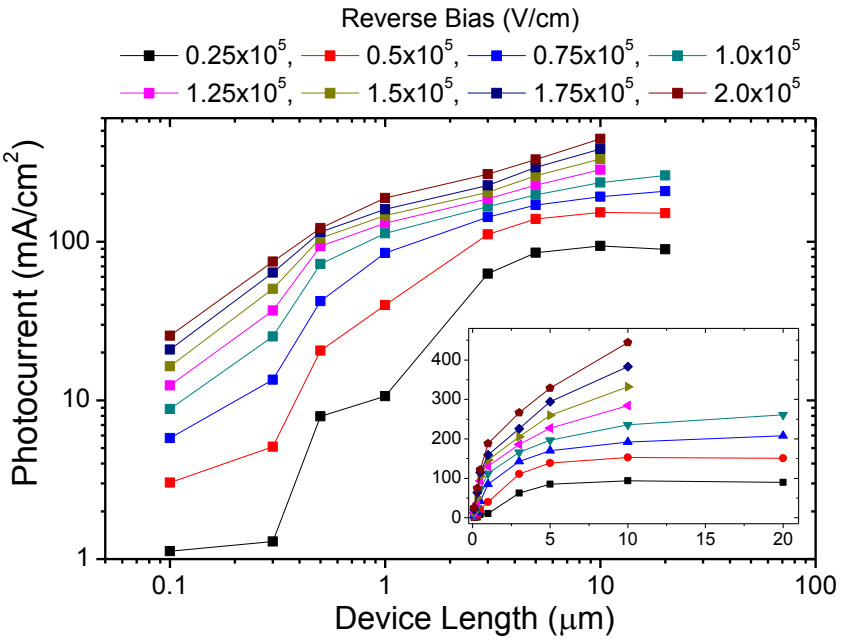

Figure 2.9: Lateral photocurrent density vs. device length (log-log scale) for P3HT:PCBM lateral BHJ devices. (Inset) Lateral photocurrent density vs. device length (linear) for the same devices. [64]

The photocurrent increases as a function of reverse bias and device length until approximately 5 μm. Previous scanning photocurrent and modeling studies have shown that SCR lengths in these materials under the experimental conditions range from 2-5 μm [62, 63, 65]. The majority of carriers that are photogenerated in the SCRs will be efficiently extracted and contribute to the measured photocurrent. Therefore increases in the device channel length up to this point will have a significant effect on the photocurrent. In larger channel length devices, the size of the SCRs remains the same and only the recombination zone significantly increases in size, which does not contribute to the photocurrent. This is shown in the inset to Figure 2.9, where the photocurrent and device length are plotted on a linear scale. Beyond a device length of 5 μm, the photocurrent saturates as the additional photogenerated carriers are formed in the recombination zone of the larger devices. At higher field strengths the photocurrent saturation is less pronounced due to additional contribution to the photocurrent from injection. These trends support the existence of long carrier drift lengths in organic BHJ materials as well as SCRs and a recombination zone within lateral BHJ devices and their behavior as described in Sections 2.2 and 2.3

Chapter 3: *In Situ* Potentiometry

3.1 Introduction

In a lateral bulk heterojunction (BHJ) device under illumination, the internal electric field is enhanced within the space charge regions (SCRs) close to the electrodes in order to enhance carrier extraction. The increase in the electric field can also be interpreted as an increase in the voltage dropped across the SCRs, which is much larger for their small size compared to the rest of the lateral device channel. This can be clearly seen in the theoretical device models shown in Figures 2.3 and 2.4, in which the majority of the applied voltage across the lateral BHJ device is dropped across the device SCRs. For the case of unipolar carrier mobilities, this is across only one SCR dominated by the slower carrier, while in the ambipolar case, the voltage is divided equally across both SCRs. In both device model cases, the voltage across the central recombination zone is relatively small. The proportion of the total applied bias dropped across each SCR is dependent on the carrier mobility ratio. As the slower carrier will build up more space charge within its SCR, a larger field enhancement will occur within that SCR, and therefore a larger proportion of the total applied voltage will be dropped across that SCR. Although there is a consistent relationship between these SCR voltages and the mobility ratio, it is not as simple as the simple inverse relationship between the mobility ratio and the length of the SCRs, as expressed in Equation 2.13. Figure 3.1 shows the simulated potential profile of a 10 μm lateral BHJ device under a reverse bias of 50 V, assuming carrier mobilities of $\mu_p = 5\times10^{-4}$ cm^2/Vs and $\mu_n = 10^{-3}$ cm^2/Vs. The simulation procedure was the same as described in Chapter 2, but assuming a larger bimolecular recombination coefficient of $\beta = 10^{-11}$ cm^3/s.

*Contains material previously published in Reference [76]

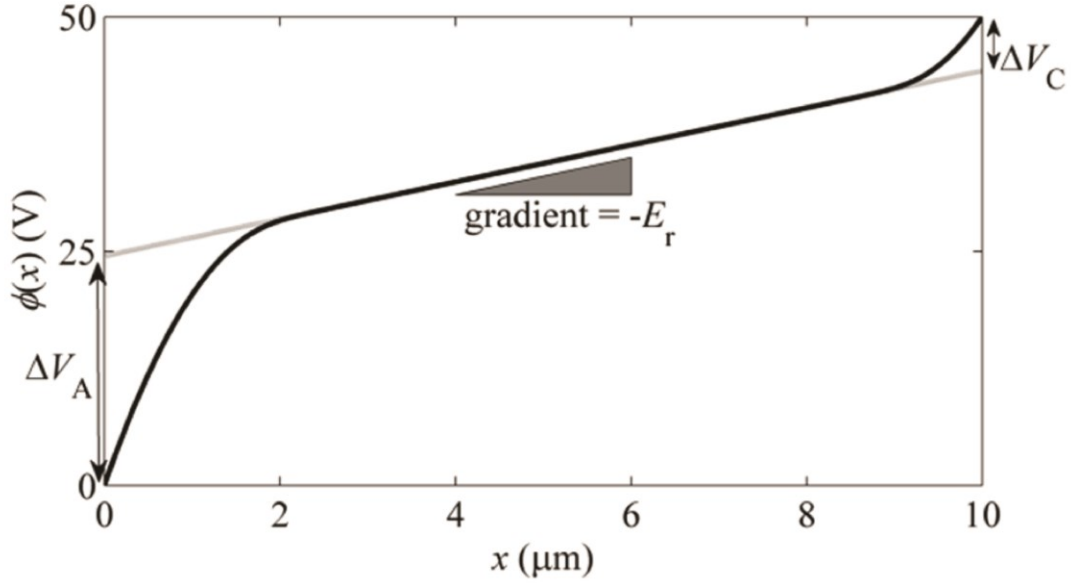

Figure 3.1: The simulated voltage profile of a 10 μm lateral BHJ device under a reverse bias of 50 V. [63]

Under these simulation conditions with a larger recombination coefficient, the central recombination zone has a non-negligible electric field E_r. Therefore the sum of the voltage across the two SCRs is not the total applied bias, and we must extrapolate E_r to the contacts to obtain the anode and cathode SCR voltage drops. ΔV_A and ΔV_C correspond to the voltages across the anode and cathode, from the SCRs dominated by holes and electrons, respectively. As expected, a larger amount of the applied voltage is dropped across the slower hole dominated SCR at the anode.

Potential profile simulations such as this were run for a broad range of photogeneration rates, recombination coefficients, and relative dielectric permittivities, selected to cover the variation in the properties of organic BHJ materials. Under each permutation of these material parameters, 11 pairs of ΔV_A and ΔV_A values were calculated from 11 pairs of electron and hole mobility ratios, ranging from the unipolar to ambipolar conditions described in Chapter 2 [63]. The ratio $\Delta V_A/\Delta V_C$ was then plotted versus the mobility ratio μ_n/μ_p, shown in Figure 3.2.

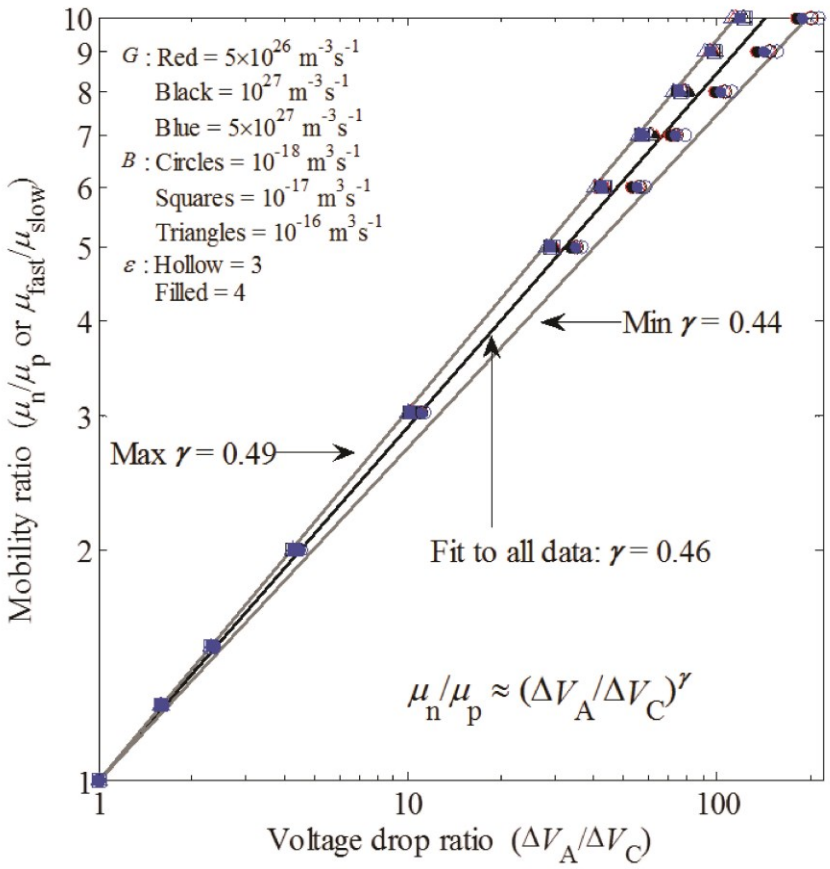

Figure 3.2: A plot of SCR voltage drop ratio vs. carrier mobility ratio based on 198 different simulations with varying generation, recombination, and permittivity conditions. [63]

Despite the broad range of simulation parameters, the carrier mobility ratio and the voltage drop ratio roughly follow an empirical power law. From the on Figure 3.2, the relationship is best described by the following equation, although there is a narrow spread in the power values:

$$\frac{\mu_n}{\mu_p} = \left(\frac{\Delta V_A}{\Delta V_C}\right)^{0.46} \tag{3.1}$$

Both the size and voltage across the SCRs in a lateral BHJ device can therefore be used to calculate the carrier mobility ratio, even in ambipolar material systems.

3.2 *In Situ* Potentiometry Methods

The open geometry of lateral BHJ devices allows for a variety of spatially resolved measurements across the channel. These include scanning photocurrent microscopy (SCPM) [64, 65] and electric field induced second harmonic generation (EFISH) microscopy [66, 67] techniques, which have been previously used to map the photocurrent and electric field profiles of lateral BHJ devices. These methods have supported the 3-zone model space charge limited (SCL) behavior in lateral devices and can be used to calculate the mobility ratio from the SCR lengths, which can be measured from changes in the photocurrent or electric field strength. The slower carrier mobility can then be calculated from Equation 2.16, reproduced here for convenience:

$$J_{ph} = \chi\sqrt{2}(\varepsilon\mu)^{\frac{1}{4}}(eG)^{\frac{3}{4}}(V + E_r d)^{\frac{1}{2}} \tag{3.2}$$

However, these techniques (SCPM and EFISH) require complex experimental setups and rely on laser excitation of the BHJ material. By constructing multiple *in situ* voltage probes in the lateral BHJ device channel, we gain a direct method to construct its potential profile

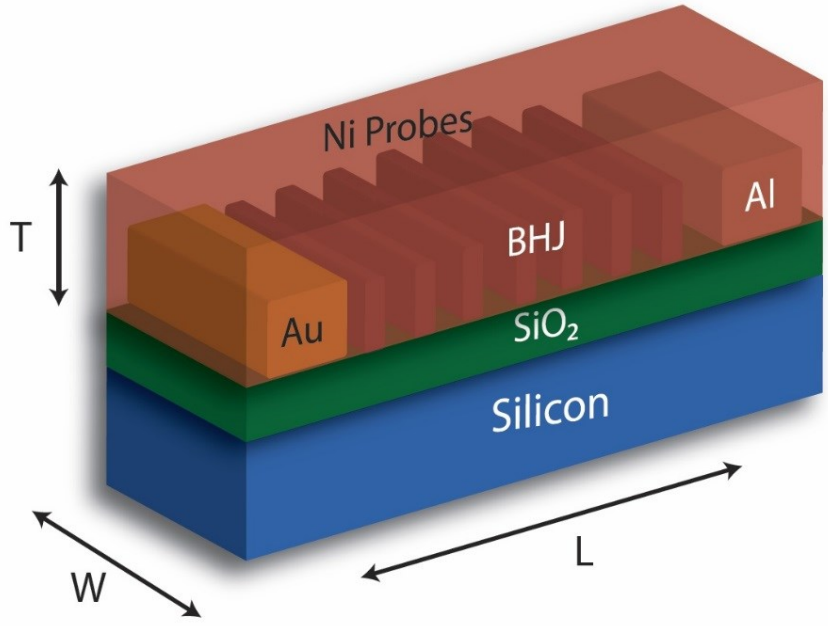

Figure 3.3: A schematic illustration of a lateral BHJ device with in situ voltage probes.

The changes in the slope of the potential profile can be used to distinguish the two SCRs from the central recombination zone, allowing us to investigate charge transport within different regions of a lateral BHJ device. The magnitude of the SCR voltage drops and the recombination zone field, E_r, can also be easily calculated from the potential profile.

Lateral BHJ devices with *in situ* voltage probes were fabricated on a p-type silicon substrate with 2600 Å of thermally grown silicon dioxide, as shown in Figure 3.3. Interdigitated electrodes and voltage probes were defined using a JEOL JBX-6000 electron beam lithography tool in three separate steps. Aluminum (Al) was used for the cathodes, gold (Au) for the anodes, and nickel (Ni) for the voltage probes and device pads, due to its mechanical robustness. The device channel lengths were 10 or 20 μm with a W/L of 1000. For the 20 μm devices, 24 Ni voltage probes extended 60 μm into the channel and were 200 nm wide with an average spacing of 600 nm. 12 Ni voltage probes 30 μm long were used for the 10 μm devices. All metal layers were deposited under thermal evaporation to a thickness of 500 Å. An SEM image of a 20 μm *in situ* potentiometry device is shown in Figure 3.4.

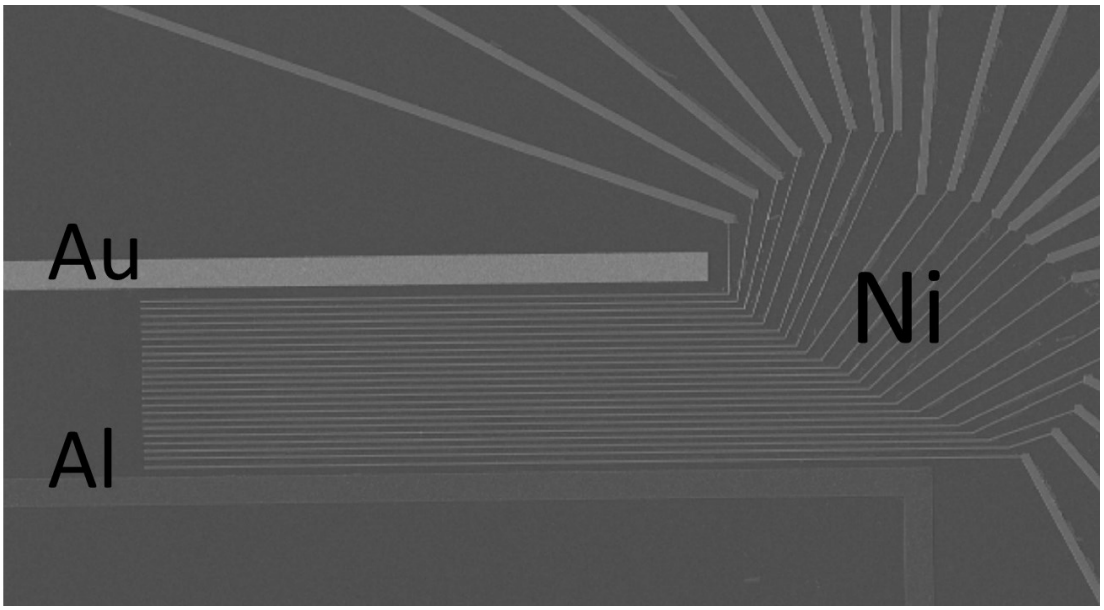

Figure 3.4: SEM image of the corner of a 20 μm lateral device with 24 voltage probes extending into the channel for in situ potentiometry. The thickness of the volage probes is 200 nm and their average spacing is 600 nm.

Before the deposition of the BHJ layer, the substrate was dipped into a phosphoric acid solution for 10 seconds to remove any oxide on the surface of the Al electrodes. This was followed by a solvent rinse procedure to degrease the substrate, which consisted of acetone, methanol, and isopropyl alcohol. The BHJ absorber layer was deposited from a 20 mg/mL solution of P3HT:PCBM (1:1 by weight) in chloroform that had been heated to 50 ºC and stirred for over 16 h. The BHJ was spun cast at 1200 rpm for 60 s, followed by annealing at 140 ºC for 15 min in a nitrogen atmosphere. The film was 165 nm thick as measured by profilometry.

Electrical measurements were performed in a *Desert Cryogenics* cryogenic probe station under vacuum better than 5×10^{-3} torr at 300 K. Four-terminal measurements were made in the dark and under illumination using an *Agilent 4155C Semiconductor Parameter Analyzer*. These measurements were repeated sequentially for the different voltage probes across the channel. The electric field generated due to the work function difference between the electrodes and the Ni probes were negligible compared to the overall field. Sample illumination was achieved using an *Oriel model 66912* 150 W ozone-free xenon lamp, modified with an AM1.5 spectral filter.

3.3 Lateral Device Potential Profiles

The voltage probe measurements yield linear voltage sweeps throughout the entire applied bias range, as shown in Figure 3.5. Only data from reverse bias conditions was analyzed, in order to reduce carrier injection effects and simulate the average internal electric field magnitudes found in OPV devices. In Figure 3.6, the probe voltages measured at a particular applied bias are plotted spatially, constructing the channel voltage profiles. The slope of the potential profile is the magnitude of the electric field in the channel. In the central recombination zone, the slope is lower than in the SCRs, indicating increased electric field strength in the SCRs. This is expected from our three zone lateral device model. The measured overall photocurrent was consistent between individual voltage probe measurements.

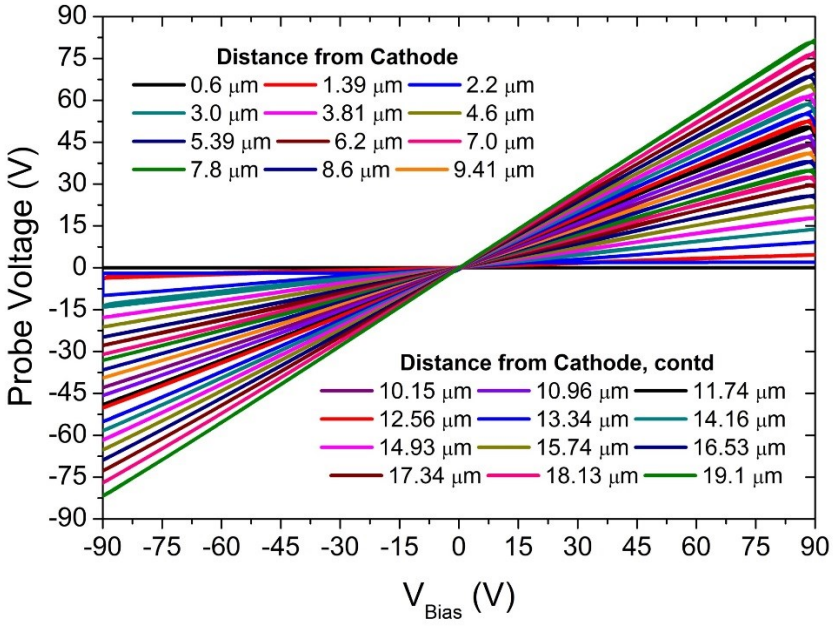

Figure 3.5: Voltage sweeps for a 20 μm P3HT:PCBM lateral BHJ device under 100 mW cm^{-2} AM1.5 illumination.

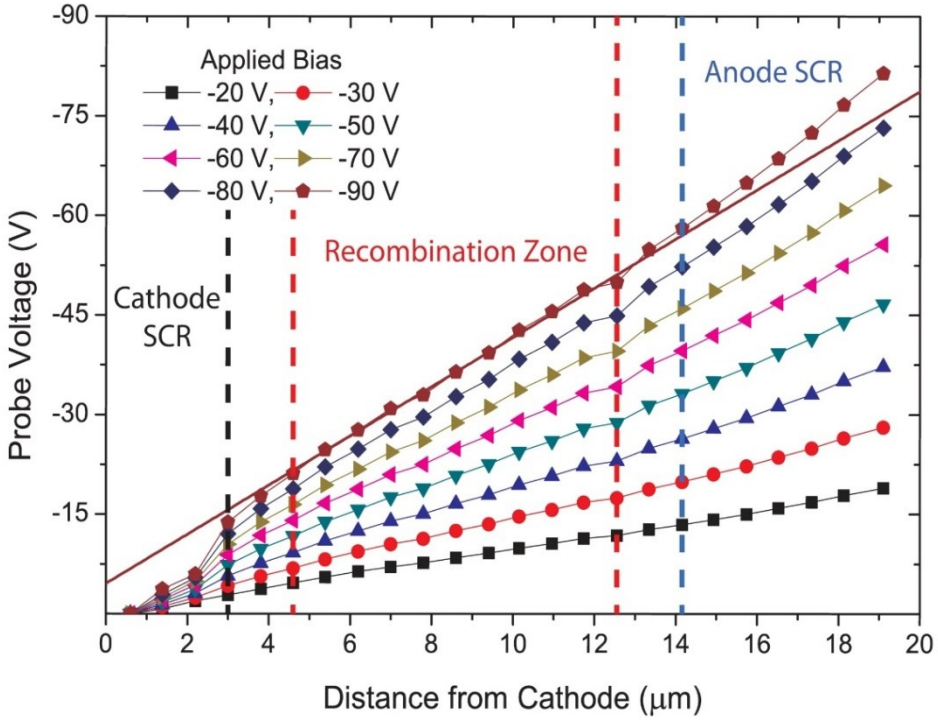

Figure 3.6: Potential profiles constructed from voltage measurements shown in Figure 3.5 at particular total applied biases. Demarcation of the different zones is based on voltage exponent analysis. The projected line from the recombination zone at an applied reverse bias of 90 V shows the increased electric field in the SCRs adjacent to the electrodes. [76]

The spatial extent of the two SCRs and the recombination zone was determined by calculating the slope of the lateral current density vs. voltage curve on a log-log plot for different regions of the device. This slope (m) is the functional dependence in $J_{lat} \propto V^m$ and is plotted as a function of the applied voltage for different regions of the device in Figure 3.7.

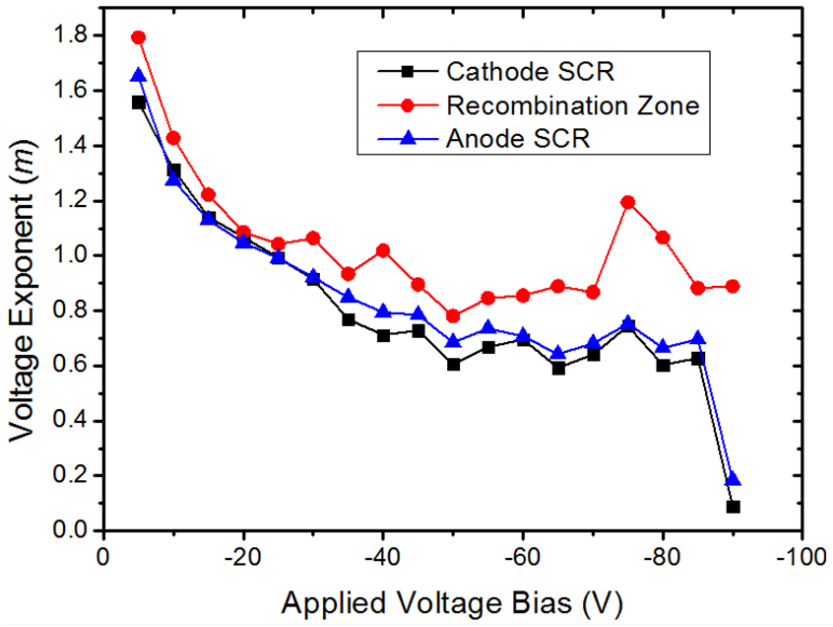

Figure 3.7: Voltage exponent (m) vs. applied bias for the same 20 µm P3HT:PCBM lateral BHJ device under 100 mW cm^{-2} AM1.5 illumination.

At low applied biases, contact resistance causes a high dependence of the photocurrent on the voltage. As the voltage increases, the exponent begins to stabilize at different values for different regions of the device. From data from probes close to the electrodes, m stabilizes close to 0.5, indicative of SCL photocurrent behavior and a regime where Equation 3.2 is valid. This behavior is observed in the channel from 0-3 µm and 14.1-20 µm, defining the extent of the SCRs. From data from probes in the center of the device, m stabilizes closer to 1, as the recombination zone exhibits ohmic behavior. This behavior is observed from 4.6-12.6 µm within the device channel. Although spatial resolution of the different regions is limited due to the size and spacing of the voltage probes, *in situ* potentiometry is capable of determining the approximate extent of these regions within the device and examining their different charge transport properties.

Once the extent of the different regions is known, data from probes within the recombination zone can be used to calculate E_r at different applied voltages. In Figure 3.6, the projected line indicates E_r at -90 V. The voltage drops over the cathode and anode SCRs at this applied bias are -4.54 V and -11.3 V, respectively, as shown by the intersection of the projected line at 0 μm and 20 μm. The larger anode SCR voltage drop indicates that holes are the slower mobility carrier. The larger size of the anode SCR is also a sign of carrier mobility asymmetry [64, 65]. From Equation 3.1, the carrier mobility ratio μ_n/μ_p is approximately 1.50. This calculation was repeated for the different applied biases in which SCL transport is dominant and the mobility ratio is consistent over this range. From Figure 2.5, we estimate a χ value of approximately 1.27 for the calculated mobility ratio.

As the recombination field in this device is large, Equation 3.2 is used to calculate the slower hole mobility from the slope of the fitted line in Figure 3.8. On this plot, $(V+E_rd)^{1/2}$ can be defined as the square root of the voltage dropped only across the SCRs. The non-negligible contribution from the recombination zone is subtracted out. The SCL photocurrent equation is a good fit to the data, though there is some divergence at low voltages. This divergence is likely due to the contact resistance effects dominant at these low voltages, as shown in Figure 3.7.

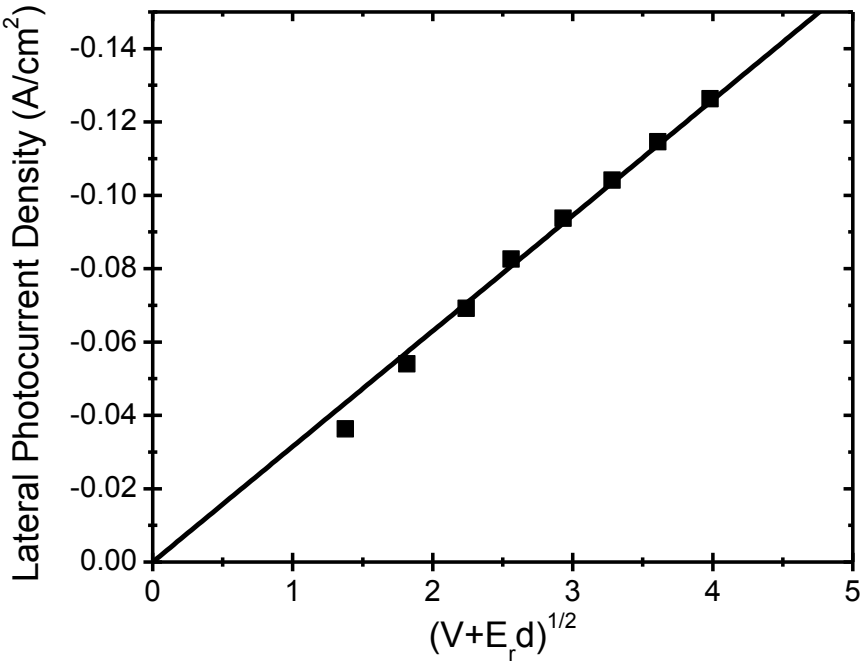

Figure 3.8: Lateral photocurrent density vs. the square root of the sum of the voltage drops measured in both SCRs of the same lateral BHJ device under 100 mW cm^{-2} AM1.5 illumination. [76]

The electron mobility can now be found from the previously calculated mobility ratio. The resulting mobility values of $\mu_h = 3.65 \times 10^{-4}$ cm^2/Vs and $\mu_e = 5.49 \times 10^{-4}$ cm^2/Vs are comparable with literature values for vertical P3HT:PCBM solar cells.

From the two carrier mobilities, we can also calculate the carrier concentration and bimolecular recombination coefficient for the BHJ material. As the electron and hole carrier concentrations are equal in the recombination zone, the conductivity within this region can be defined as:

$$\frac{J_{ph}}{E_r} = e\Delta n(\mu_h + \mu_e) = e\sqrt{\frac{G}{\beta}}(\mu_h + \mu_e) \qquad (3.3)$$

where Δn is the electron (or hole) concentration in the recombination zone and β is the bimolecular recombination coefficient. These parameters are listed in Table 3.1 below and are consistent with previous P3HT:PCBM measurements using photo-CELIV and SCL methods [28, 74, 75]. Recombination is assumed to be bimolecular from conductivity vs. light intensity

measurements which will be described in the next chapter [76]. Similar to earlier reports on vertical P3HT:PCBM solar cells [29, 77], the bimolecular recombination coefficient is orders of magnitude smaller than the Langevin recombination coefficient; in this case, B/B_L is approximately 0.0068. This indicates that non-Langevin recombination is dominant in this organic BHJ material.

Table 3.1. Charge transport parameters of the lateral P3HT:PCBM BHJ device from Figure 3.6 under 100 mW cm^{-2} AM1.5 illumination. [76]

μ_h (cm^2/Vs)	μ_e (cm^2/Vs)	Δn (cm^{-3})	β_r ($cm^3\ s^{-1}$)
3.65×10^{-4}	5.49×10^{-4}	2.34×10^{16}	1.13×10^{-11}

In most disordered organic semiconductors there is also an electric field dependence of carrier mobility; *in situ* potentiometry is also capable of evaluating this relationship. Figure 3.9 plots the measured photocurrent vs. the combined SCR voltage drop from a 10 μm P3HT:PCBM lateral device.

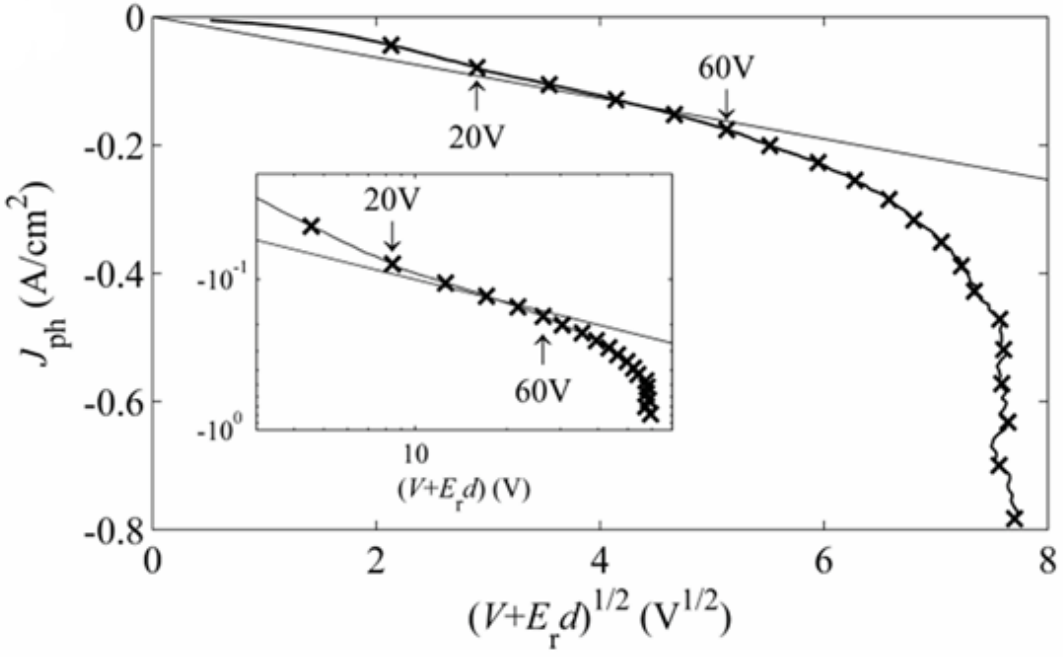

Figure 3.9: Measured photocurrent vs. $(V+E_rd)^{1/2}$ of a 10 μm P3HT:PCBM lateral device under 100 mW cm^{-2} AM1.5 illumination. The solid line is a linear fit according to Equation 3.2. The inset shows the same data and fit in a double-logarithm plot. [63]

This lateral BHJ device was prepared using the same procedure described above on a separate substrate and with a new P3HT:PCBM solution. The analysis technique described above was used to calculate an electron mobility of 3.8×10^{-4} cm^2/Vs and a hole mobility of 4.6×10^{-4} cm^2/Vs. These values were extracted from a fit to Equation 3.2, shown as a solid line in Figure 3.9 over the range in which SCL transport was observed. In Figure 3.9, the low voltage data below ~20 V diverges from the SCL photocurrent fit due to carrier extraction barriers at the contacts. At voltages above 60 V, the photocurrent increases dramatically due to carrier injection. However, the experimental photocurrent curve over the voltage range where SCL behavior is dominant has a steeper gradient that what is predicted by the theoretical straight line. This may be caused by a small increase in carrier mobilities with increasing electric field. We calculate a series of best fit lines from Equation 3.2 with different, increasing slopes, over the entire voltage range from 20 to 60 V to obtain the change in carrier mobilities. From these slopes, the series of recalculated electron and hole mobilities over the voltage range from 20 to 60 V are plotted with the square root of the recombination zone field in Figure 3.10.

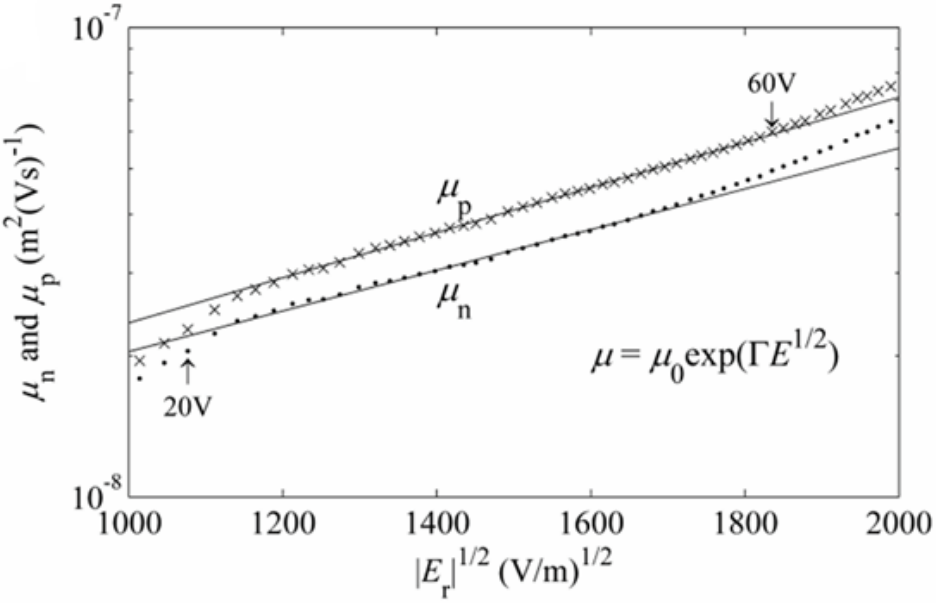

Figure 3.10: Plot of electron (•) and hole (×) mobilities versus recombination zone electric field for the same 10 μm P3HT:PCBM lateral device under 100 mW cm^{-2} AM1.5 illumination. [63]

If we consider that the recombination zone occupies the majority of the device length, most charge carriers within the device experience an electric field similar to the recombination zone electric field. In disordered organic semiconductor systems, charge transport mainly occurs by hopping between localized states. These states are separated by Coulombic potential barriers. The Poole-Frenkel model describes how the applied electric field reduces this potential barrier to hopping transport [78]. The hopping probability, and therefore the charge carrier mobility, will be dependent on the electric field via the following equation:

$$\mu = \mu_0 exp\left(\Gamma\sqrt{|E_r|}\right) \tag{3.4}$$

where μ_0 is the zero field mobility and Γ is a temperature-dependent activation factor [78-80]. Previous measurements on vertical structures have shown Poole-Frenkel behavior in P3HT:PCBM [39]. The close fit to the data in the SCL range in Figure 3.10 suggests that Poole-Frenkel like transport behavior also occurs in the lateral direction for P3HT:PCBM. We extract zero field mobilities of 7.8×10^{-5} cm^2/Vs and 7.5×10^{-5} cm^2/Vs for holes and electrons, respectively [63]. In summary, *in situ* potentiometry measurements on lateral devices can be used to find several important charge transport parameters of BHJ materials based on simple four terminal measurements and compare them to values obtained from vertical OPV cell techniques.

Chapter 4: Use of Lateral Devices for Materials Characterization

4.1 Introduction

Although using *in situ* potentiometry to measure key charge transport parameters of organic bulk heterojunction (BHJ) materials is a promising technique, constructing a detailed potential profile from four terminal measurements is difficult and time consuming. A single potential profile such as in Figure 3.6, with 24 points of measurement across a 20 μm channel, can take up to 1 hour to measure. This makes monitoring the changes in BHJ material parameters with time or environmental conditions using *in situ* potentiometry very difficult, due to the long time scales of the measurements. Lateral BHJ devices with large numbers of thin voltage probes are also difficult to fabricate using electron beam lithography, and these complicated structures can be easily damaged. This procedure can be simplified by only probing a few points in the center of the device to measure the recombination zone field. While constructing a detailed profile does allow us to visualize the different charge transport regions of the lateral BHJ device, the size of the voltage probes limits the resolution of these measurement, especially when compared to scanning photocurrent (SCPM) [64, 65] or electric field induced second harmonic generation (EFISH) microscopy [66, 67]. In these techniques, high precision measurements of the sizes of the space charge regions (SCRs) allow us to determine the carrier mobility ratio of the organic BHJ material. With *in situ* potentiometry, only the measurement of the recombination zone field is necessary for this calculation. Extrapolation of this field out to the device contacts defines the voltage drops over the cathode and anode SCRs, ΔV_A and ΔV_C. Equation 3.1, reproduced here for convenience, is then used to calculate the mobility ratio:

$$\frac{\mu_n}{\mu_p} = \left(\frac{\Delta V_A}{\Delta V_C}\right)^{0.46} \tag{4.1}$$

To measure this field, we used large lateral BHJ devices fabricated on glass substrates using a JEOL JBX-6000 electron beam lithography tool. In our studies, lateral BHJ devices were originally fabricated on Si:SiO_2 substrates to compare traditional field effect transistor

(FET) mobility measurements with our SCL based techniques, but this was found to be unnecessary as our lateral measurement techniques matured. Glass substrates were used in later fabrication steps to remove the influence of FET behavior. These new lateral devices had channel lengths of 50 μm with a W/L = 500 and 5 voltage probes extending 150 μm into the channel. Aluminum (Al) was used as the cathode, gold (Au) as the anode, and nickel (Ni) for the voltage probes and device pads, due to its mechanical robustness. All metal layers were deposited via thermal evaporation to a thickness of 500 Å. The voltage probes were placed at least 5 μm away from either electrode to ensure that they were inside the recombination zone during device operation. As shown previously from photocurrent measurements of lateral devices with different channel lengths [64], SCPM [65], and EFISH microscopy [66], the lengths of the SCRs in organic BHJ materials are of order 1-5 μm due to the high voltage biases employed and the large carrier drift lengths. An SEM image of a 50 μm *in situ* potentiometry device is shown in Figure 4.1:

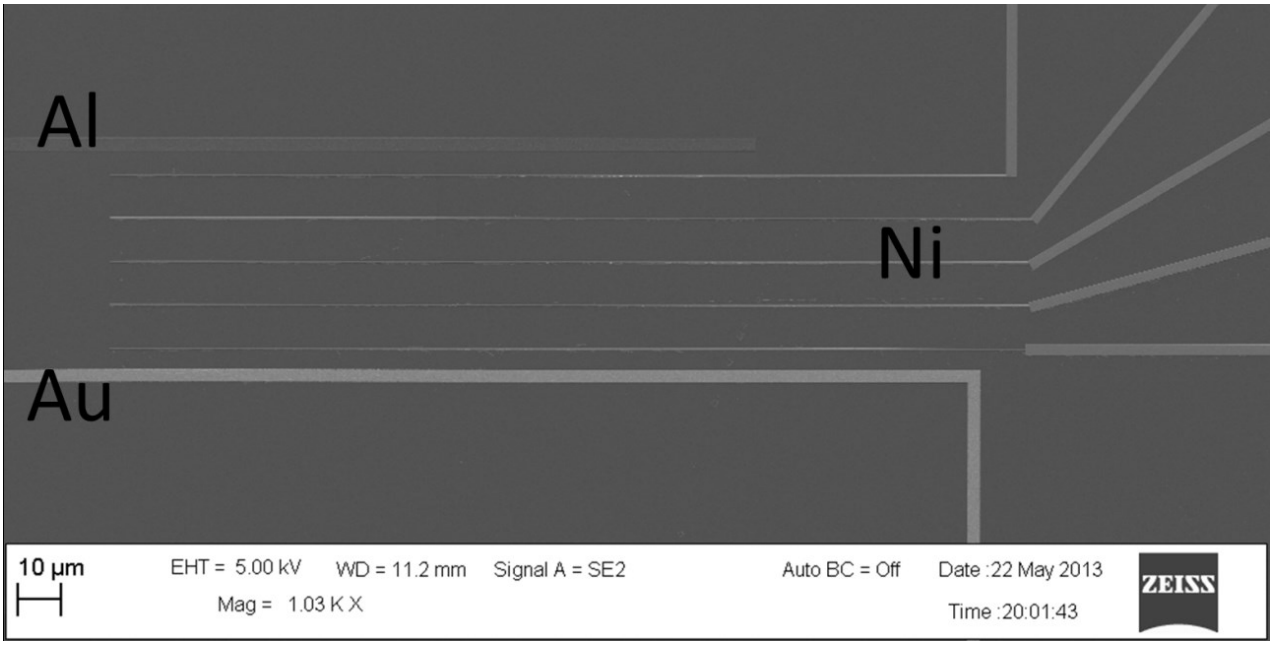

Figure 4.1: SEM image of the corner of a 50 μm lateral device with 5 voltage probes extending into the channel for simplified in situ potentiometry. The thickness of the volage probes is 200 nm and their average spacing is 10 μm.

Before the deposition of the BHJ layer, the substrate was dipped into a phosphoric acid solution for 10 seconds to remove any oxide on the surface of the Al electrodes. This was followed by a solvent rinse procedure to degrease the substrate, which consisted of acetone, methanol, and isopropyl alcohol. Unless otherwise stated, the preparation and measurement of the BHJ material was performed in the following manner: The BHJ absorber layer was deposited from a 20 mg/mL solution of P3HT:PCBM (1:1 by weight) in chloroform that had been heated to 50ºC and stirred for over 16 h. The BHJ was spun cast at 1200 rpm for 60 s, followed by annealing at 140ºC for 15 min in a nitrogen atmosphere. Film thicknesses were between 100-200 nm and measured using profilometry. Electrical measurements were performed in a *Desert Cryogenics* cryogenic probe station under vacuum better than 5×10^{-3} torr at 300 K. Four-terminal measurements were made in the dark and under illumination using an *Agilent 4155C Semiconductor Parameter Analyzer*. These measurements were repeated sequentially for the different voltage probes across the channel. The electric field generated due to the work function difference between the electrodes and the Ni probes were negligible compared to the overall field. Sample illumination was achieved using an *Oriel model 66912* 150 W ozone-free xenon lamp, modified with an AM1.5 spectral filter. The intensity was 100 mW/cm^2 and modified using neutral density filters.

The voltage probe measurements yield linear voltage sweeps throughout the entire applied bias range. As before, voltage exponent analysis was used to calculate the functional dependence in $J_{lat} \propto V^m$ from the slope of the lateral current density vs. voltage curve on a log-log plot for different regions of the device. The current vs. voltage relationship was examined for the region between the Al electrode and the closest Ni voltage probe, the region between the two Ni voltage probes furthest from each other, and the region between the Au electrode and the closest Ni voltage probe. Although the SCRs did not always make up the entirety of these regions between the closest voltage probes and the electrodes, this exponent analysis was needed to determine at what applied reverse biases space charge limited (SCL) photocurrent behavior

was dominant. The behavior of the exponent (*m*) with applied voltage per unit length for a 50 μm lateral P3HT:PCBM device is shown in Figure 3.2:

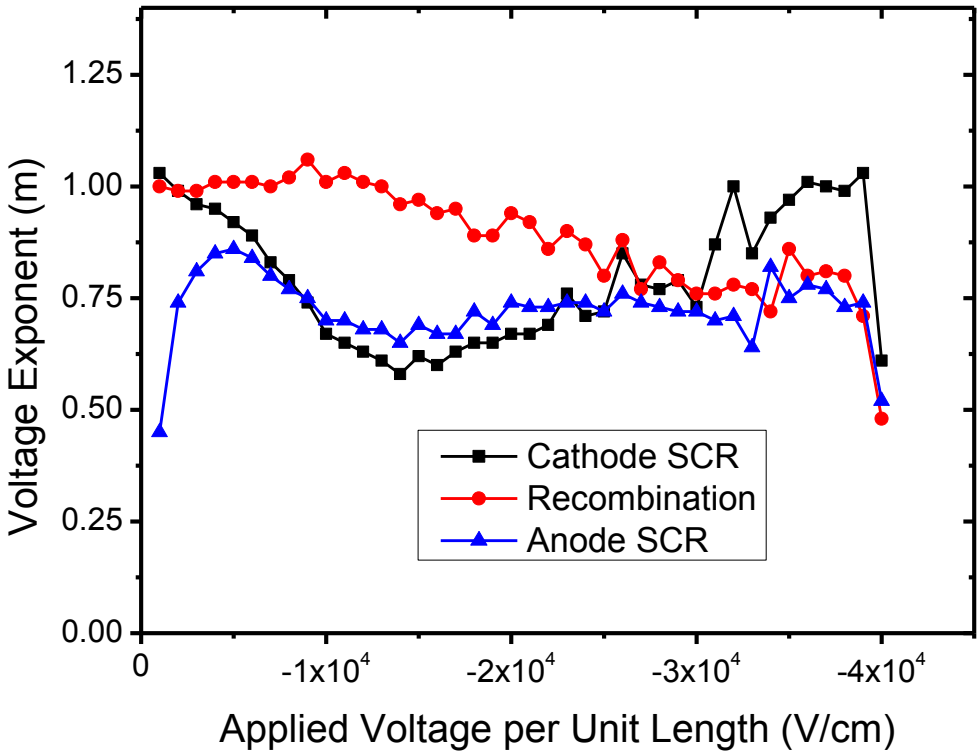

Figure 4.2: Voltage exponent (m) vs. applied voltage per unit length for a 50 μm P3HT:PCBM lateral BHJ device under 100 mW cm^{-2} AM1.5 illumination.

Due to the larger separation between the voltage probes, the differences in the charge transport behavior of the different regions can be more clearly seen. The exponent in the SCRs stabilizes close to 0.5, indicative of SCL behavior. The exponent *m* does not entirely reach 0.5 because the 5 μm regions between the electrodes and their closest probe are divided between the SCR and some small part of the recombination zone. This is also because of the Poole-Frenkel dependence of the mobility on the electric field, which can enhance the value of the voltage exponent. In the center of the device, the recombination zone exhibits ohmic behavior, as shown by the stable exponent close to 1.0. This is in agreement with our three zone model for lateral BHJ devices. As the applied electric increases, the distinction in the charge transport behavior between the different regions disappears as the SCL photocurrent is overcome by the injection of

charge carriers. If a stronger electric field was applied, the exponents for the different regions would uniformly increase past 1.0 due to this carrier injection from the contacts. However, in these larger devices we are usually unable to apply an electric field large enough to cause this.

From the exponent analysis, we know over what applied bias range SCL photocurrents are dominant and our three zone model of lateral BHJ devices is applicable. We construct a simplified potential profile from the four terminal measurements, shown in Figure 4.3:

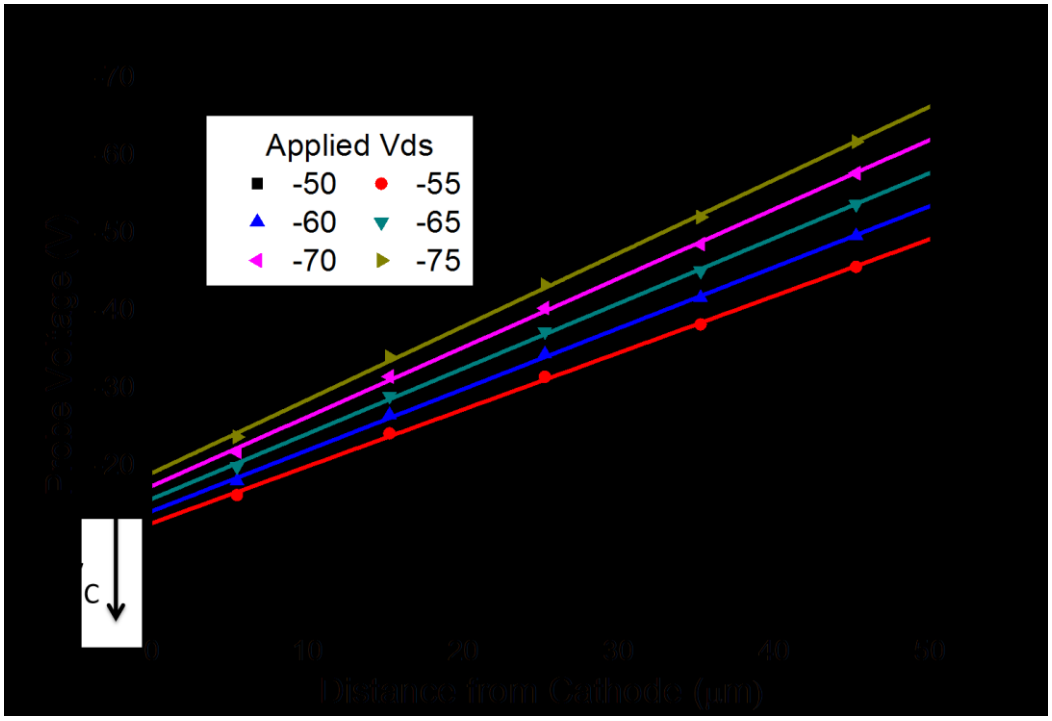

Figure 4.3: Potential profiles for a 50 μm P3HT:PCBM lateral BHJ device under 100 mW cm^{-2} AM1.5 illumination. All voltage probes lie within the recombination zone of these devices, therefore the fitted lines indicate the recombination zone field, E_r. ΔV_A and ΔV_C for an applied bias of -75 V are indicated on the Figure.

The intercepts of the fitted recombination zone field are then used to measure ΔV_A and ΔV_C. For this measurement, the larger voltage drop over the cathode SCR indicates a slower electron mobility; from Equation 3.1, we calculate a mobility ratio, μ_n/μ_p, of approximately 0.63. From this simplified technique, we can quickly measure the mobility ratio of organic BHJ materials, even if they are close in magnitude, and monitor the change in the ratio in response to various environmental conditions. This is especially important for BHJ materials, as the electron

donating and electron accepting organic materials may react differently to environmental effects such as water, oxygen, ultraviolet light, and increased temperature. Monitoring the change in mobility ratio with respect to these conditions can inform the design of better material systems for organic photovoltaic (OPV) applications.

In order to calculate the actual carrier mobilities, we measure the photocurrent from these lateral BHJ devices and fit it to our modified SCL photocurrent equation:

$$J_{ph} = \chi\sqrt{2}(\varepsilon\mu)^{\frac{1}{4}}(eG)^{\frac{3}{4}}(V + E_r d)^{\frac{1}{2}} \qquad (4.2)$$

where χ is the ambipolarity factor that is estimated from the mobility ratio and Figure 2.5, and μ is the slower carrier mobility. Although μ can be calculated from the measured photocurrent of the large 50 μm device, more accurate measurements can be obtained from measuring the photocurrent of small lateral BHJ devices. These devices are fabricated on the same substrate as the larger devices with voltage probes using the same electron beam lithography techniques.

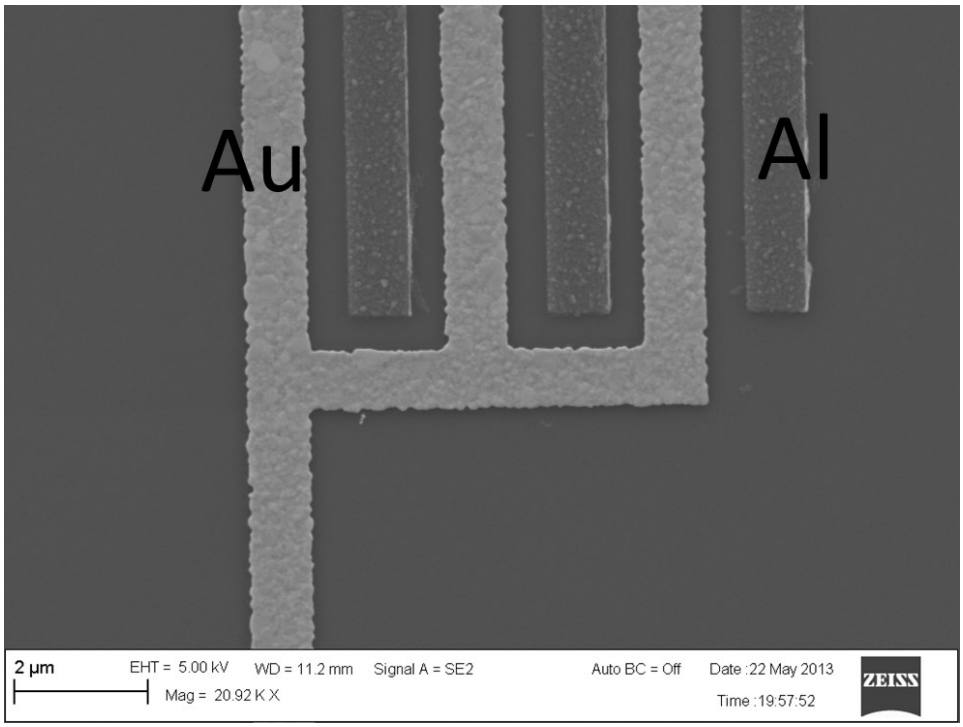

Figure 4.4: SEM image of part of a 500 nm channel length lateral BHJ device.

In devices with channel lengths smaller than a few microns, the channel is primarily composed of one SCR dominated by the slower carrier. This simplified behavior allows for better fits of the photocurrent behavior of small lateral devices to the SCL equation and gain more accurate measurements of the slower carrier mobility. Multiple I-V measurements on many small devices can also be performed quickly in order to obtain multiple slow carrier mobility estimates, providing a rough estimate of the error in the SCL mobility calculation from the scatter in measurements. For these small devices, there is a negligible voltage drop over the recombination zone, therefore the following SCL equation applies:

$$J_{ph} = \chi\sqrt{2}(\varepsilon\mu)^{\frac{1}{4}}(eG)^{\frac{3}{4}}(V)^{\frac{1}{2}} \tag{4.3}$$

where V is the total applied voltage. From this combination of measurements, we calculate both carrier mobilities. From the two carrier mobilities and the conductivity in the recombination zone of the large devices, we can also calculate the carrier concentration and bimolecular recombination coefficient for the BHJ material. Assuming bimolecular recombination:

$$\frac{J_{ph}}{E_r} = e\Delta n(\mu_h + \mu_e) = e\sqrt{\frac{G}{\beta}}(\mu_h + \mu_e) \tag{4.4}$$

where Δn is the electron (or hole) concentration in the recombination zone and β is the bimolecular recombination coefficient.

4.2 Recombination Mechanisms

The relationship between conductivity and the incident light intensity is indicative of the dominant nongeminate recombination type in the central region [76]. Since there is no net photogeneration within the recombination zone, the recombination rate and generation rate are approximately equal:

$$R \approx G \propto P \tag{4.5}$$

*Contains material previously published in Reference [76]

where R is the recombination rate, G is the generation rate, and P is the incident light intensity. The conductivity in the recombination zone (σ_R) is given by:

$$\sigma_R = q\,\Delta n\,\mu_n + q\,\Delta p\,\mu_p = q\,\Delta n(\mu_n + \mu_p) \tag{4.6}$$

where Δn and Δp are the electron and hole concentrations, and μ_n and μ_p are their mobilities. As stated previously, the photogenerated carrier concentrations in the recombination zone are equal. Bimolecular recombination is a process in which the recombination rate is linearly proportional to the square of the carrier concentration: $R \propto \Delta n \Delta p \propto \Delta n^2$ [76]. Conductivity is proportional to the carrier concentration (Equation 4.6), therefore, for the case of bimolecular recombination in the central recombination zone the square of the conductivity must be proportional to the incident light intensity:

$$\sigma_R^2 \propto P \tag{4.8}$$

In materials in which trap-assisted or other monomolecular recombination mechanisms are dominant, we predict that the recombination zone conductivity will be proportional to the light intensity [76]. This assumes that the carrier mobilities are roughly constant with light intensity, which is a limitation of this model. In addition, when the bimolecular recombination coefficient β is not a constant and depends on the carrier concentration, then $\sigma_R^{2+x} \propto P$, where x is a small positive number close to 0.6 in P3HT:PCBM at 300 K [49].

The conductivity (Figure 4.5a) and the square of the conductivity (Figure 4.5b) were calculated from potentiometry measurements made within the recombination zone of a lateral P3HT:PCBM device under AM1.5 illumination with light intensities ranging from 6 mW/cm^2 to 100 mW/cm^2. In the recombination zone, the square of the condutivity is linear with respect to the light intensity, indicating that bimolecular recombination is present. Bimolecular recombination is therefore a bulk material property of P3HT:PCBM.

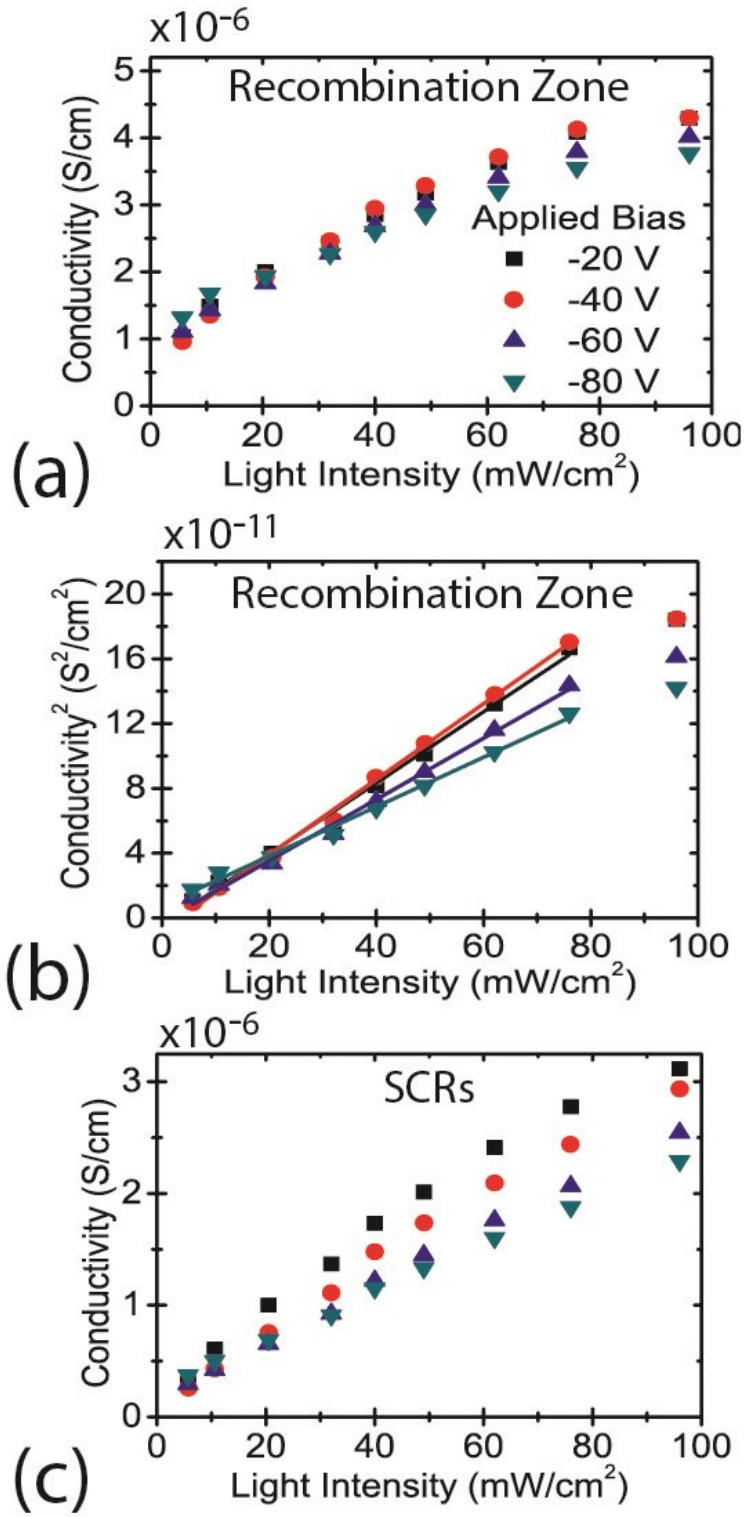

Figure 4.5: Conductivity (a) and conductivity^2 (b) vs. incident light intensity in the recombination zone of a P3HT:PCBM lateral BHJ device under AM1.5 illumination. Linear fits are indicated by the solid lines. Conductivity (c) vs. incident light intensity in the SCRs.

However, the square of the conductivity stabilizes at the highest intensities (Figure 4.5b), showing sub-linear behavior. This is due to the effect of the high carrier concentrations at these intensities on the bimolecular recombination coefficient. This method does not allow us to identify the recombination type prevalent in the SCRs, as the generation rate is not equal to the recombination rate in these regions. The conductivity vs. intensity relationship is more linear in the SCRs than in the recombination zone, as shown in Figure 4.5c. This valuable insight cannot be easily obtained from conventional vertical devices. It is likely that the recombination in the SCRs is of a more unimolecular nature, due to the imbalanced carrier densities in these regions. Bimolecular recombination from the central recombination zone, and not from the SCRs, is the dominant mechanism for nongeminate recombination loss in this lateral P3HT:PCBM device.

The dominant recombination mechanism, however, can vary between organic BHJ material systems and change due to environmental conditions. In addition, multiple mechanisms may be significant during device operation [24, 35]. Lateral devices offer a unique characterization method that enables us to alter the recombination mechanism in the device and measure the resulting change in charge transport parameters of the BHJ material. When an organic semiconductor is exposed to a polar molecule such as ethanol, there is enhanced self-trapping of charges, which cause a reduction the current [81]. The polar molecule is absorbed on to the surface of the semiconductor, where its dipole induces a local field through polarization of the semiconductor. The dipole in the polar molecule may also shift in response to charge carriers at material interfaces in the BHJ material. This effect has been previously utilized in sensing applications for organic FETs [81, 82], and we use a similar procedure to measure the effect of the increased charge trapping on lateral BHJ devices.

The BHJ absorber layer was deposited from a 20 mg/mL solution of P3HT:$PC_{71}BM$ (1:1 by weight) in chloroform that had been heated to 50ºC and stirred for over 24 h. The BHJ was spun cast at 1200 rpm for 60 s, followed by annealing at 145ºC for 15 min in a nitrogen atmosphere. Electrical measurements were performed in a *Desert Cryogenics* cryogenic probe

station initially under vacuum better than 5×10^{-5} torr at 300 K. The probe station was then filled with nitrogen containing 2000 ppm of ethanol vapor (dipole moment = 1.69 D) to approximately 100 torr and the lateral BHJ devices were measured again. Finally, the cryo station was pumped back down to vacuum better than 5×10^{-5} torr and the devices measured again. The sample was kept at 300 K for the entire procedure. Figure 4.6 illustrates the change in recombination zone conductivity behavior with respect to incident light intensity, for these three conditions.

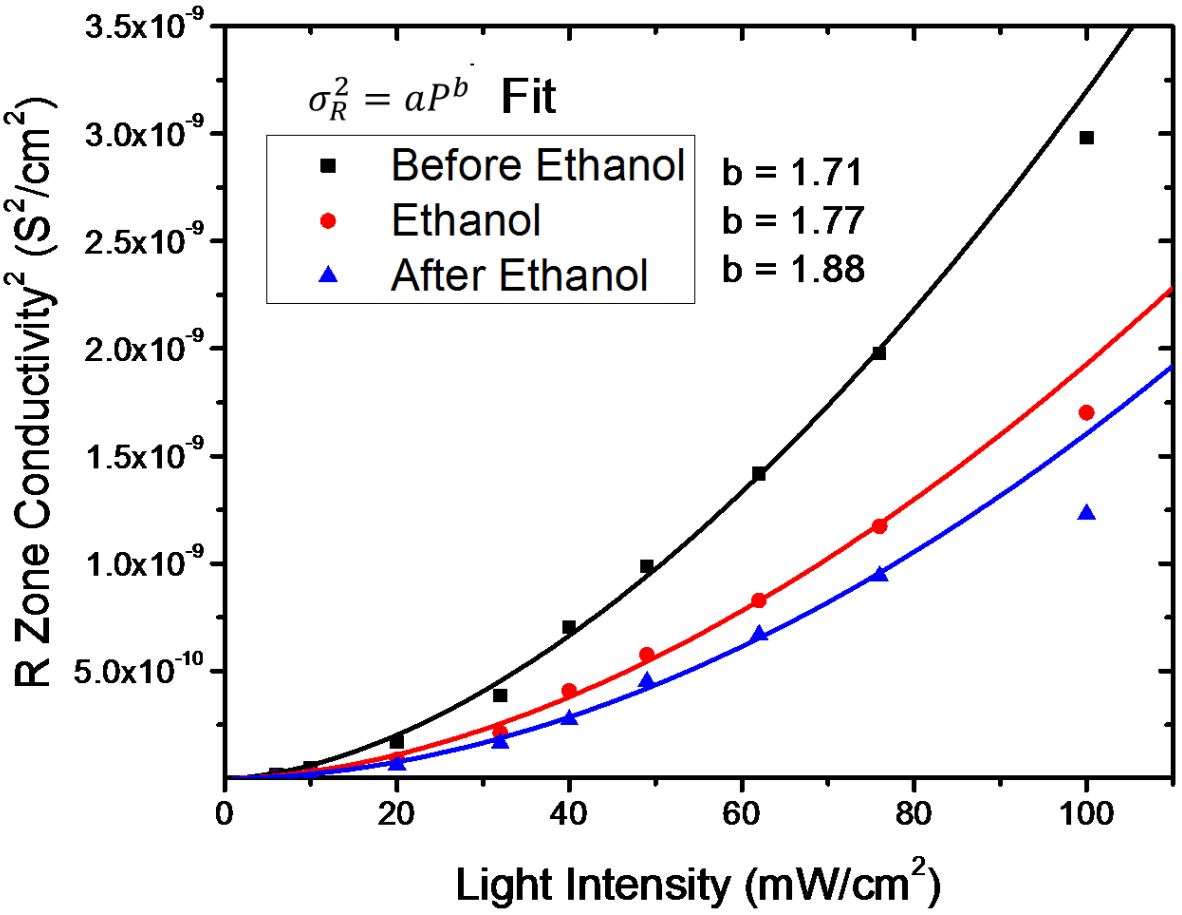

Figure 4.6: Conductivity^2 vs. incident light intensity in the recombination zone of a 50 µm P3HT:$PC_{71}BM$ lateral BHJ device under AM1.5 illumination, before, during, and after exposure to ethanol vapor. Fits are indicated by the solid lines.

The conductivity^2 data within the recombination zone is fitted to a function of the form: $\sigma_R^2 = aP^b$, where P is the incident light intensity. Initially, the fitted exponent b is at a value of 1.71, indicating the presence of both unimolecular and bimolecular recombination mechanisms.

A purely unimolecular recombination process would show a quadratic dependence of the recombination zone conductivity on the light intensity, as the electron and hole concentrations in the recombination zone are equal. After the sample is exposed to the ethanol vapor, the exponent increases, indicating a shift to more unimolecular dominated recombination as traps are introduced into the BHJ system. This shift is not reversible by pumping to low vacuum, and the increase in unimolecular recombination increases even after the removal of the ethanol vapor. It is likely that the introduced trap states remain in the system without additional treatment, such as annealing, to remove them. The effect of the introduced dipole can also been seen in the measured SCL mobility of the BHJ material, shown in Figure 4.7:

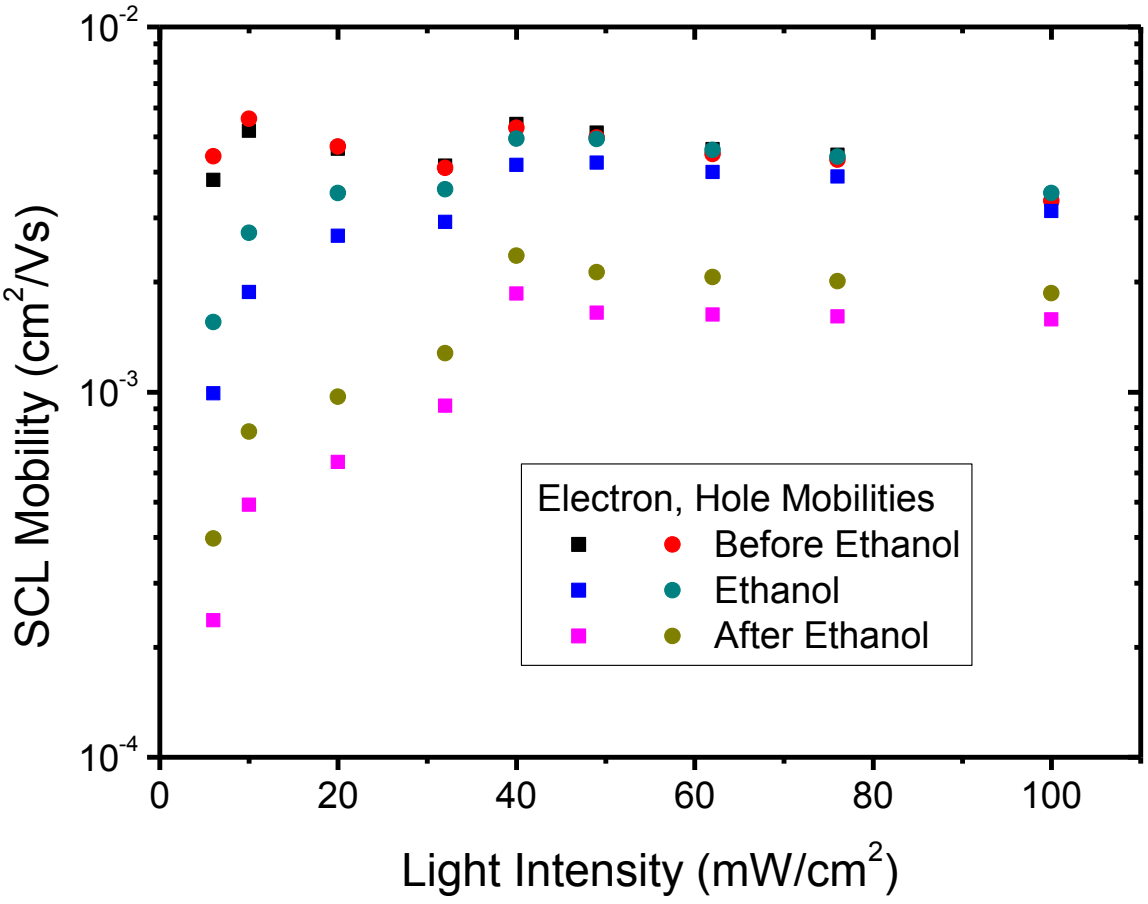

Figure 4.7: SCL electron (square) and hole (circle) mobilities vs. incident light intensity measured from small P3HT:$PC_{71}BM$ lateral devices under AM1.5 illumination, before, during, and after exposure to ethanol vapor.

Initially, the measured SCL mobilities are consistently high (~3.5 × 10^{-3} cm^2/Vs) for all measured incident light intensities. The mobility ratio μ_n/μ_p is close to 1.0, determined from potentiometry measurements on large devices. Upon introduction of the ethanol vapor, the SCL mobilities at low intensities begin to decrease, and the mobility ratio diverges from 1.0 at these low intensities as well, with electrons as the slower carrier. At higher intensities there is little change. The increased number of traps would have the most noticeable effect on the SCL mobilities at low intensities, where the low photogenerated carrier concentrations fill a smaller proportion of the trap states. After the ethanol vapor is removed and the cryo station has been pumped back down to low pressures, the material has deteriorated further. Much of the absorbed ethanol remains in the film and increases the self-trapping of charges. The SCL mobility at high intensities decreases, and there is a more significant drop in mobility and the mobility ratio at low intensities. The larger effect on the electron mobility may indicate the higher number of electron trap states introduced upon exposure to ethanol vapor.

4.3 Degradation Monitoring

A major advantage of using the combined measurement strategy described in Section 4.1 is a drastic reduction in the measurement time, in contrast to the work described in Chapter 3, utilizing devices with up to 24 *in situ* voltage probes. This technique can therefore be used to actively monitor the degradation of BHJ materials, and determine the effect of degradation on parameters such as the carrier mobilities and recombination coefficient. The primary degradation mechanisms of P3HT:PCBM are known to be photo-oxidation processes that lead to a breaking of the macromolecular backbone [83-85]. To investigate processes that operate over shorter time scales, we prepared P3HT:PCBM lateral BHJ devices and measured them under high background pressure conditions (≥ 5 × 10^{-3} torr) in our cryogenic probe station at 300 K. The change in the potential profiles of large 50 μm devices over an hour under these conditions is shown in Figure 4.8:

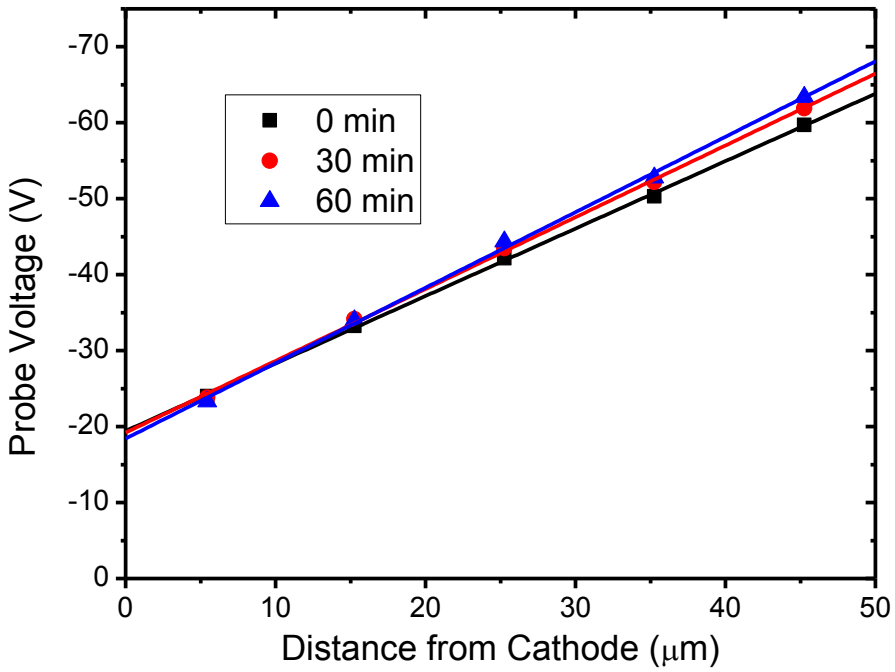

Figure 4.8: Potential profiles of a lateral P3HT:PCBM device under 100 mW/cm^2 AM1.5 illumination at a reverse bias of 75 V, measured at various times after insertion into a high background pressure environment.

The change in slope of the potential profile indicates a change in the mobility ratio of the BHJ film. Over the course of the measurement, a proportionally smaller amount of voltage is dropped across the hole dominated SCR at the anode. The electron mobility therefore decreases relative to the hole mobility over the measurement time. The higher slope can also imply a higher recombination rate, due to the increase in voltage across the recombination zone. The actual mobility and recombination values are calculated from the photocurrent measurements:

Table 4.1: Charge transport parameters of a lateral P3HT:PCBM device under 100 mW/cm^2 AM1.5 illumination.

P3HT:PCBM	μ_n/μ_p	μ_n (cm^2/Vs)	μ_p (cm^2/Vs)	Δn (cm^{-3})	β_r (cm^3 s^{-1})
0 min	0.76	8.39×10^{-4}	1.10×10^{-3}	8.34×10^{16}	8.90×10^{-13}
30 min	0.69	5.42×10^{-4}	7.87×10^{-4}	9.41×10^{16}	6.98×10^{-13}
60 min	0.63	2.57×10^{-4}	4.08×10^{-4}	7.72×10^{16}	1.04×10^{-12}

Although a decrease in the recombination zone conductivity was observed over time, we attribute this to a significant decrease in mobility rather than a change in the recombination characteristics. The carrier concentration and recombination coefficient remain relatively constant over the course of the experiment, while both carrier mobilities decrease significantly. The mobilities also become more imbalanced over time, with the electron mobility more severely affected. This observed imbalance is consistent with EFISH measurements of P3HT:PCBM made on similar time scales [66]. A rapid increase in the voltage across the electron dominated SCR was noted and attributed to photo-oxidation introducing negatively charge electron traps, resulting from moisture within the device [66, 86].

This time dependent measurement was repeated with the same P3HT:PCBM solution, but with 5% by volume of the solvent additive DIO (1,8-diiodooctane). DIO is known to produce better phase separation and structural order within the BHJ film, resulting in higher performance of OPV cells [87, 88]. We repeated this experiment with the solvent additive in an attempt to mitigate the mobility imbalance in the material. Table 4.2 lists the charge transport parameters with respect to time of this modified P3HT:PCBM solution.

Table 4.2: Charge transport parameters of the same lateral P3HT:PCBM device with 5% of DIO under 100 mW/cm^2 AM1.5 illumination.

P3HT:PCBM w/DIO	μ_n/μ_p	μ_n (cm^2/Vs)	μ_p (cm^2/Vs)	Δn (cm^{-3})	β_r (cm^3 s^{-1})
0 min	0.67	3.54×10^{-4}	5.29×10^{-4}	1.46×10^{17}	2.90×10^{-13}
120 min	0.48	2.74×10^{-4}	5.65×10^{-4}	8.69×10^{16}	8.21×10^{-13}
240 min	0.44	1.72×10^{-4}	3.93×10^{-4}	1.10×10^{17}	5.16×10^{-13}

Addition of DIO does not eliminate the mobility imbalance in favor of the hole mobility or the decreasing trend of the mobility ratio. The initial measured mobilities are lower but more

stable over time. The mobility ratio gradually reaches a stable point of approximately 0.4 over several hours. Although it does not correct the mobility asymmetry, the addition of DIO does improve the other charge transport parameters of the P3HT:PCBM film. The carrier concentration within the bulk P3HT:PCBM increases and the bimolecular recombination coefficient decreases with respect to the normal film. This technique offers a novel method to monitor degradation within BHJ films and relate degradation to changes in the charge transport parameters of the film.

4.4 Effect of Solvents and Annealing

Due to the different steps in the photovoltaic process in organic BHJ solar cells, there are several morphological parameters that need to be adjusted for an optimum solar cell. These include maximizing the surface area between the donor and acceptor material, as well as maintaining continuous material pathways for the separated charges to reach the electrodes. In cases of materials with unbalanced mobilities, for ideal performance it is necessary for the slower carrier to have a larger volume available for charge conduction. Greater control over the nanomorphology during device fabrication is therefore essential in manufacturing high performance organic solar cells.

The most common technique for controlling the phase separation and organization of the nanomorphology in P3HT:PCBM, or any other organic bulk heterojunction, is to anneal the bulk heterojunction layer after deposition. A pristine P3HT:PCBM coating is too intimately mixed to form efficient percolation paths and minimize bulk recombination [89]. Thermal annealing enables the P3HT and PCBM domains to increase in size up to optimal values corresponding with the exciton diffusion lengths in each material. The precise treatment necessary varies depending on the solvent used, ratio of electron donating and accepting material in the blend, and the environmental conditions [89, 90]. The most commonly used solvents in P3HT:PCBM OPV

fabrication are halogenated solvents such as chlorobenzne (CB), 1,2-dichlorobenzene (DCB), and chloroform. However, due to their toxicity, these solvents are unlikely to be used in mass manufacturing of organic BHJ solar cells. This has motivated researchers to experiment with novel solvent systems and utilize a variety of solvent additives to control the nanomorphology of organic BHJs for higher performance [87, 91-95].

Lateral devices can be used as material diagnostic platforms to efficiently characterize this wide variety of materials. Here we present a small sample of possible fabrication procedures, varying the solvent system used and annealing time to determine the effect on the measured charge transport parameters. The BHJ films were deposited from 20 mg/mL solutions of P3HT:$PC_{71}BM$ (1:1 by weight) in chloroform, 1,2-dichlorobenzene, or o-xylene that had been heated to 50 ºC and stirred for over 16 h. The BHJ was spun cast at 1200 rpm for 60 s, followed by annealing in a nitrogen atmosphere. The solutions prepared in DCB were either annealed at 120°C (DCB^1) or 145°C (DCB^2) for 15 min; the solution prepared in o-xylene was annealed at 200°C for 2 min; and the solution prepared in chloroform was annealed at 145°C for 15 min. These solvents and annealing procedures were chosen based on a literature survey of P3HT:PCBM solar cells[84, 89]. Table 4.3 lists the charge transport parameters for this group of BHJ solutions.

Table 4.3: Charge transport parameters of lateral P3HT:$PC_{71}BM$ devices under 100 mW/cm^2 AM1.5 illumination, prepared using different solvents and annealing procedures.

Solvent System	μ_n/μ_p	μ_n (cm^2/Vs)	μ_p (cm^2/Vs)	Δn (cm^{-3})	β_r (cm^3 s^{-1})
DCB^1	0.53	2.66×10^{-4}	5.01×10^{-4}	6.35×10^{16}	2.66×10^{-12}
DCB^2	0.45	8.53×10^{-4}	1.89×10^{-3}	2.68×10^{16}	8.59×10^{-12}
o-xylene	1.35	2.00×10^{-4}	1.48×10^{-4}	2.10×10^{17}	1.41×10^{-13}
Chloroform	1.01	2.91×10^{-3}	2.89×10^{-3}	1.14×10^{17}	4.68×10^{-13}

The DCB solutions exhibit the most severe mobility imbalance, with consistently lower electron mobilities. Using a higher annealing temperature does improve the measured SCL mobilities, but the conductivity within the film does not change significantly, as shown by the decrease in carrier concentration and the increase in recombination coefficient. DCB has a boiling point of ~180°C, and small quantities of the solvent may remain within the film after annealing at these temperatures. When heat is applied to the film in a stable atmosphere, DCB slowly evaporates from the film until an equilibrium is reached with the vapor phase of DCB in the glove box environment [93, 94]. Some solvent remains within the film and can allow $PC_{71}BM$ to diffuse and form aggregates, preventing good electron transport by disrupting the formation of the continuous BHJ network. Higher temperatures or lower boiling solvents are needed to effectively drive out the excess solvent within the film after spin coating [93]. Solutions prepared using o-xylene, which has a lower boiling point of ~140°C, were annealed at higher temperatures in order to drive out the solvent rapidly, but for a shorter period of time so that the BHJ network would not be damaged. The o-xylene devices exhibited more balanced carrier mobilities and higher recombination zone conductivities, but the individual carrier mobilities were lower by an order of magnitude in comparison to the DCB films. The hole mobility was lower when using o-xylene, which is consistent with previous OFET measurements [96]. The best charge transport parameters were found in P3HT:$PC_{71}BM$ films prepared using chloroform (BP = 61°C) and annealed at 145°C. Although the fabrication procedure is identical to previous results shown using P3HT:PCBM, the lower band gap of $PC_{71}BM$ results in higher absorption for improved OPV device performance. These films show good ambipolar transport of both electrons and holes at mobilities higher than those measured for P3HT:PCBM. The carrier concentration and recombination coefficient within the bulk BHJ are comparable to values from P3HT:PCBM films, as well as those prepared with o-xylene.

4.5 Temperature Dependent Measurements

Disordered semiconductor systems such as organic BHJ do not exhibit extended band transport, and the exact charge transport mechanism is still controversial. However, the process can be simplified by using the multiple trap and release (MTR) model, which was originally developed to describe charge transport in amorphous Si. MTR assumes quasi band transport and the existence of a mobility edge, which separates the extended from localized states. Charge carriers above the mobility edge can move freely within the semiconductor, while states below the mobility edge are treated as trap states for the charges. Transport among the trap states is forbidden; therefore trapped carriers must be thermally activated above the mobility edge to contribute to charge transport. An individual charge carrier, therefore, can be trapped and released due to thermal effects multiple times as it moves through the semiconductor. In polymer:fullerene materials, this model works well for describing transport in the polymer donor, but for the fullerene acceptors, the mobility will also depend on the percolation pathways between domains of fullerene in the film. Previously we have discussed induced trap states from exposure to ethanol, but the trap states inherent in organic BHJs from structural defects or chemical impurities can also have a large effect on the mobility and recombination rate in these materials. When used for power generation, OPV cells will experience a range of temperatures, and it is important to characterize the performance of these materials under these conditions.

We prepared lateral BHJ devices using a 20 mg/mL solution of P3HT:$PC_{71}BM$ (1:1 by weight) in chloroform that had been heated to 50ºC and stirred for over 16 h. The BHJ was spun cast at 1200 rpm for 60 s, followed by annealing at 145ºC for 15 min in a nitrogen atmosphere. The film thickness was 205 nm and measured using profilometry. Electrical measurements were performed in a *Desert Cryogenics* cryogenic probe station under vacuum better than 5×10^{-5} torr and at multiple temperatures (300, 315, 330, and 345 K). The substrate was then cooled using liquid nitrogen (LN_2) over a period of several hours back down to 300 K, and the measurements were repeated at that temperature. The measured mobility ratio (μ_n/μ_p) from the potential profiles

of large devices was 1.05 and very stable over the measured temperature range. The measured SCL mobilities from several small devices are plotted with respect to 1/T in Figure 4.9a:

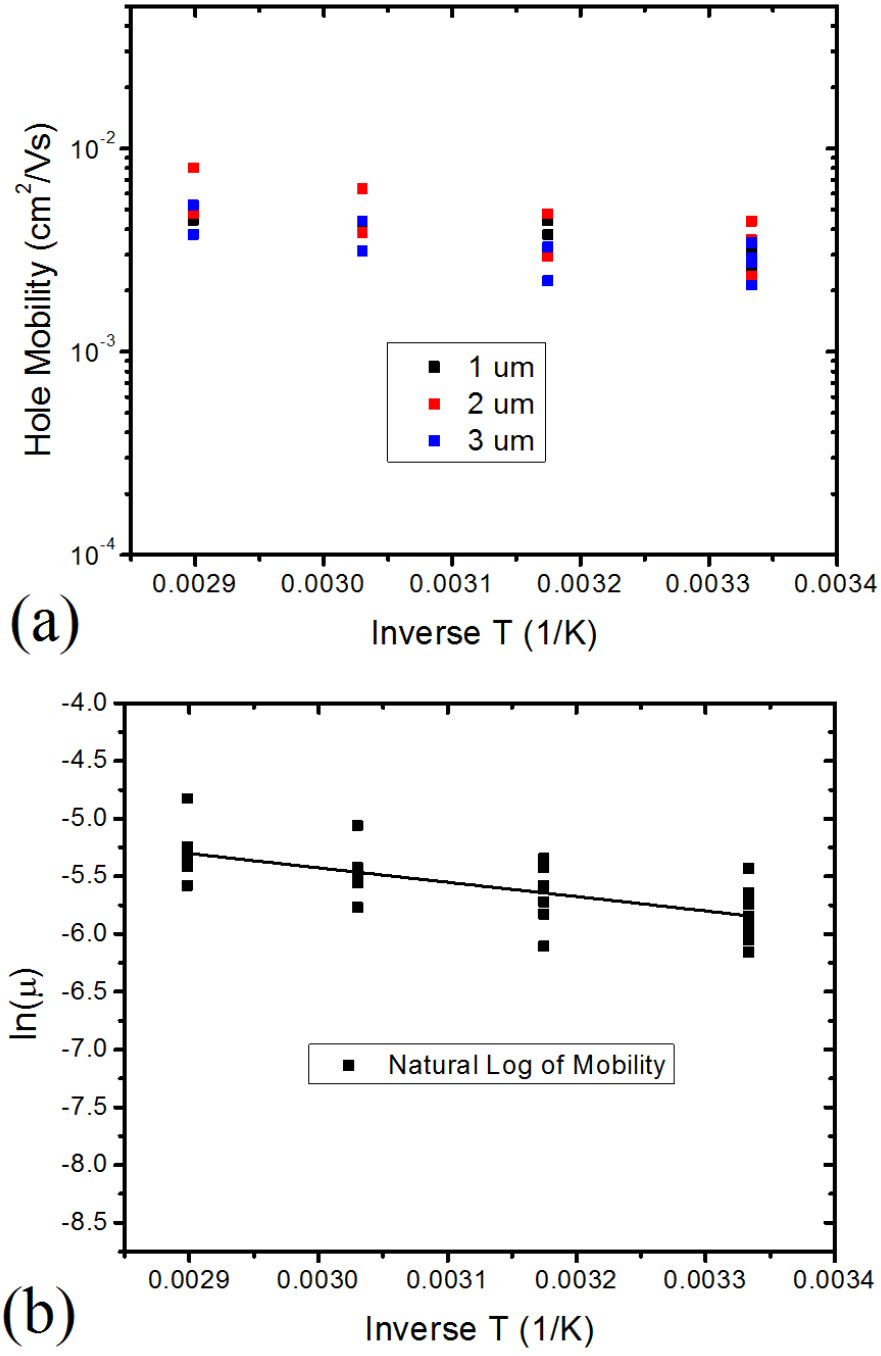

Figure 4.9: Measured SCL hole mobility (a) and its natural logarithm (b) with respect to inverse temperature for P3HT:$PC_{71}BM$ lateral devices under 100 mW/cm^2 AM1.5 illumination.

The calculated hole mobilities are consistent between measurements from different small lateral BHJ devices on the same substrate. The mobilities increase steadily with respect to temperature and there is no divergence between the 300 K measurements at the beginning and end of the experiment. By plotting the natural log of the mobility with respect to 1/T in Figure 4.10b, we can extract the activation energy of the dominant trap population in the BHJ material. The temperature dependence of the mobility is described by the Arrhenius relationship:

$$\mu = \mu_0 e^{\left(\frac{-E_a}{kT}\right)} \tag{4.9}$$

where E_a is the activation energy, k is the Boltzmann constant, and T is the temperature. The black line in Figure 4.9b is a fit to this equation, and we extract an activation energy of 107 meV from the slope. This is consistent with previous studies on P3HT:PCBM using transient photocurrent (TPC) and transient photovoltage (TPV) techniques [97, 98]. These studies show a clear peak in the trap population of P3HT:PCBM at activation energies of approximately 100 meV. With respect to temperature, the carrier concentration and recombination rate coefficient are relatively stable and the values are consistent with previous measurements based on transient techniques [49, 99]. As these values are calculated from the SCL mobilities measured from multiple small devices, there is a larger scatter in values at each measured temperature, but some trends are noticeable. Over the course of the measurement, the recombination zone conductivity steadily decreased; the second value at 300 K was approximately half the initial value. As the mobility ratio did not change, this is attributable to a steady increase in the recombination coefficient and decrease in the carrier concentration in the bulk P3HT:$PC_{71}BM$. These trends, along with the divergence in values from the 300 K measurements, are shown in Figure 4.10. The ratio between the non-Langevin and Langevin recombination coefficients increased slightly but remained on the order of 10^{-3}.

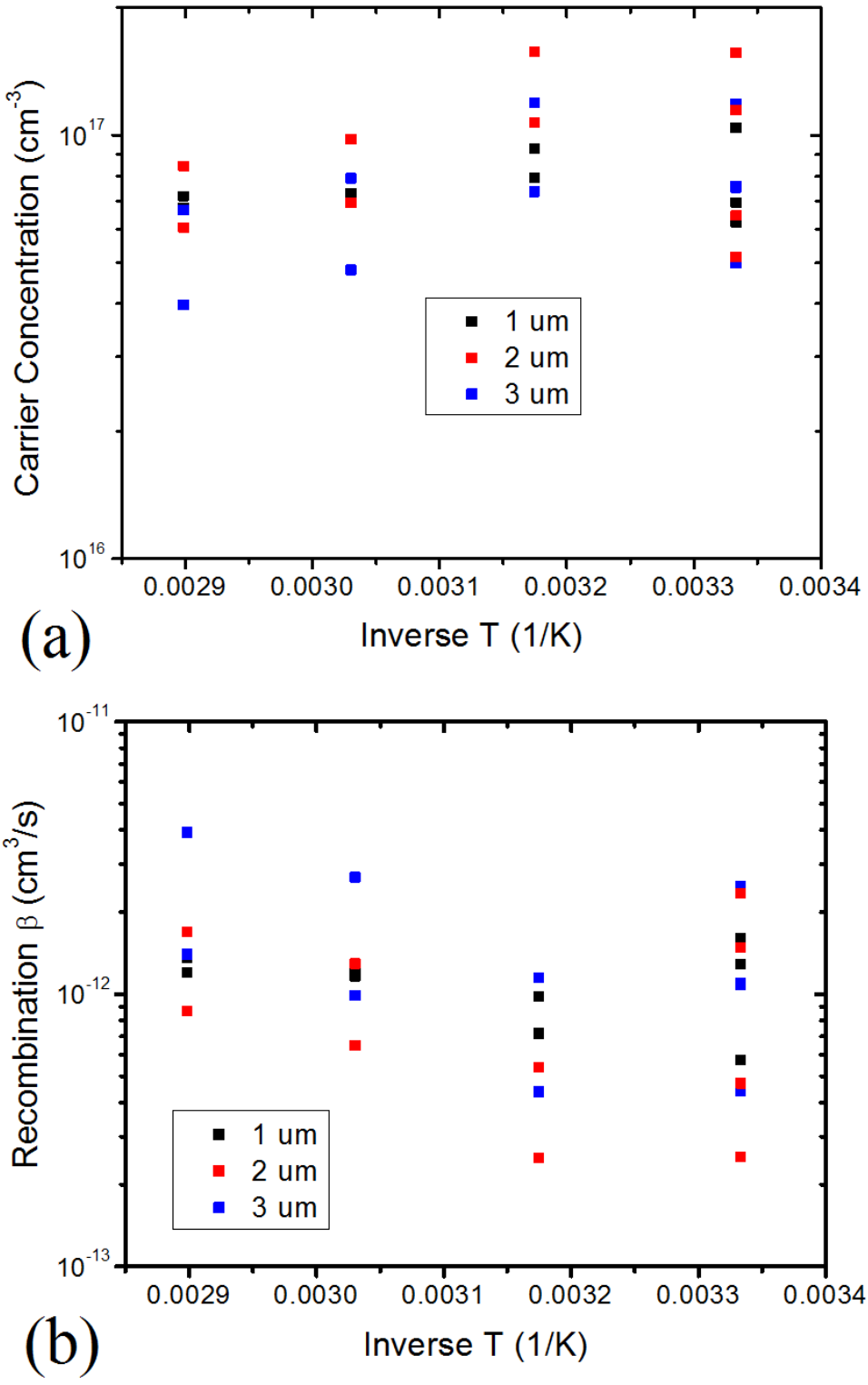

Figure 4.10: Carrier concentration (a) and bimolecular recombination coefficient (b) with respect to inverse temperature. Calculated from SCL mobility and conductivity measurements of ambipolar P3HT:$PC_{71}BM$ lateral devices under 100 mW/cm^2 AM1.5 illumination.

As this BHJ system had ambipolar transport, the difference between the hole and electron activation energies could not be distinguished. To test if activation energies of carriers in P3HT:$PC_{71}BM$ differed in systems with unequal mobilities, we prepared lateral BHJ devices using a 20 mg/mL solution of P3HT:$PC_{71}BM$ (1:1 by weight) in DCB that had been heated to 70ºC and stirred for over 16 h. The BHJ was spun cast at 1200 rpm for 60 s, followed by annealing at 145ºC for 15 min in a nitrogen atmosphere. The film thickness was 75 nm and measured using profilometry. Electrical measurements were performed in a *Desert Cryogenics* cryogenic probe station under vacuum better than 5×10^{-5} torr and at multiple temperatures (300, 315, 330, and 345 K). The substrate was then cooled using liquid nitrogen (LN_2) over a period of several hours back down to 300 K, and the measurements were repeated. During these initial measurements, the devices were measured over a range of intensities of AM1.5 spectrum ranging from 6 to 100 mW/cm^2. The sample was then heated again to 315, 330, and 345 K, cooled over several hours to 300 K, but measurements were performed at these temperatures only under 100 mW/cm^2 light intensity.

The measured mobility ratio (μ_n/μ_p) from the potential profiles of large devices was 0.42 at 100 mW/cm^2 and very stable over the measured temperature range. The mobility ratio did decrease with respect to light intensity to approximately 0.28 at 6 mW/cm^2. This behavior has been described in Section 4.2 and can be attributed to a larger population of trap states for electrons in the film. At low light intensities, the photogenerated charge carriers fill a smaller proportion of the trap states and electron mobility is more affected. The SCL mobility extracted from one small lateral BHJ device vs. incident light intensity at different temperatures is shown in Figure 4.11.

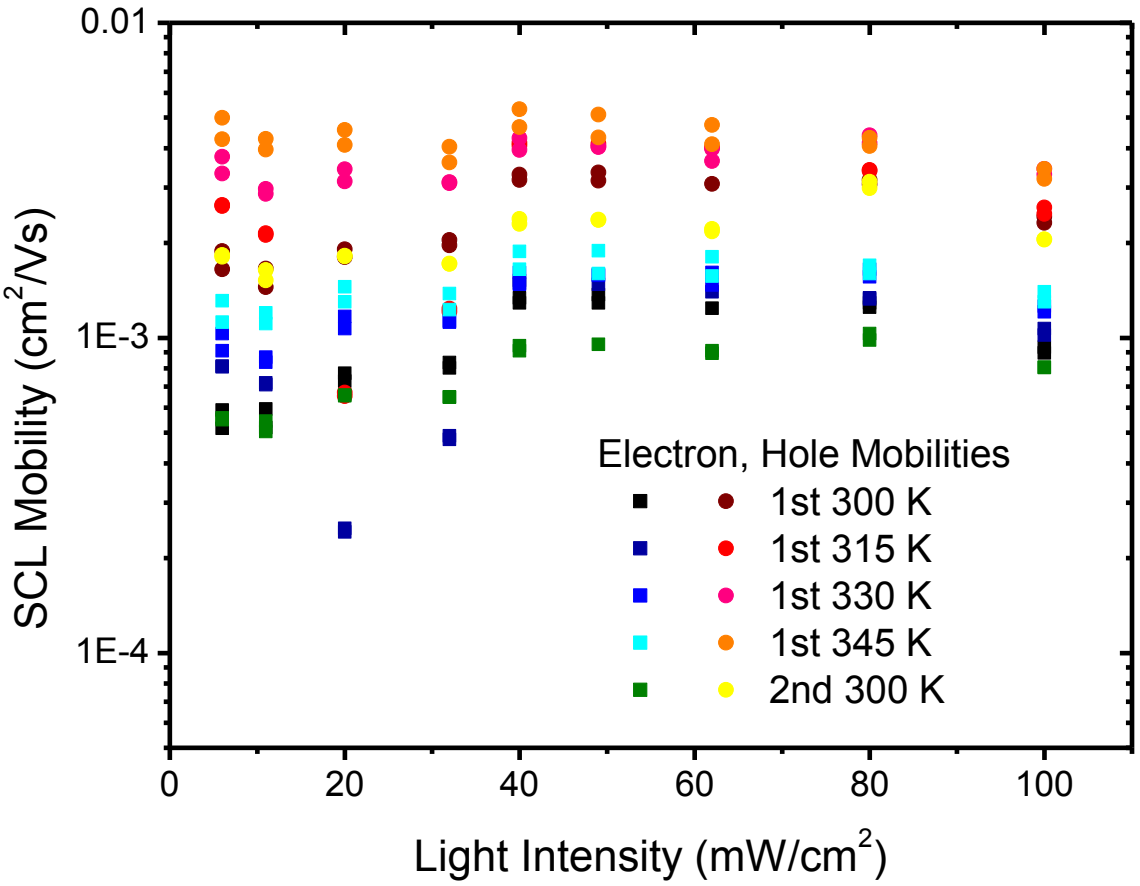

Figure 4.11: SCL electron (square) and hole (circle) mobilities vs. incident light intensity measured from a 500 nm channel length P3HT:$PC_{71}BM$ lateral device under AM1.5 illumination at different temperatures.

The natural logs of measured SCL mobilities from several small devices are plotted with respect to 1/T in Figure 4.13. As before, the calculated mobilities are consistent between measurements from different small lateral BHJ devices and the mobilities increase steadily with respect to temperature, with no divergence between measurements made at different times. Due to the stability of the mobility ratio with temperature, we expect similar hole and electron activation energies. These were calculated using Equation 4.9 and are shown on Figure 4.12.

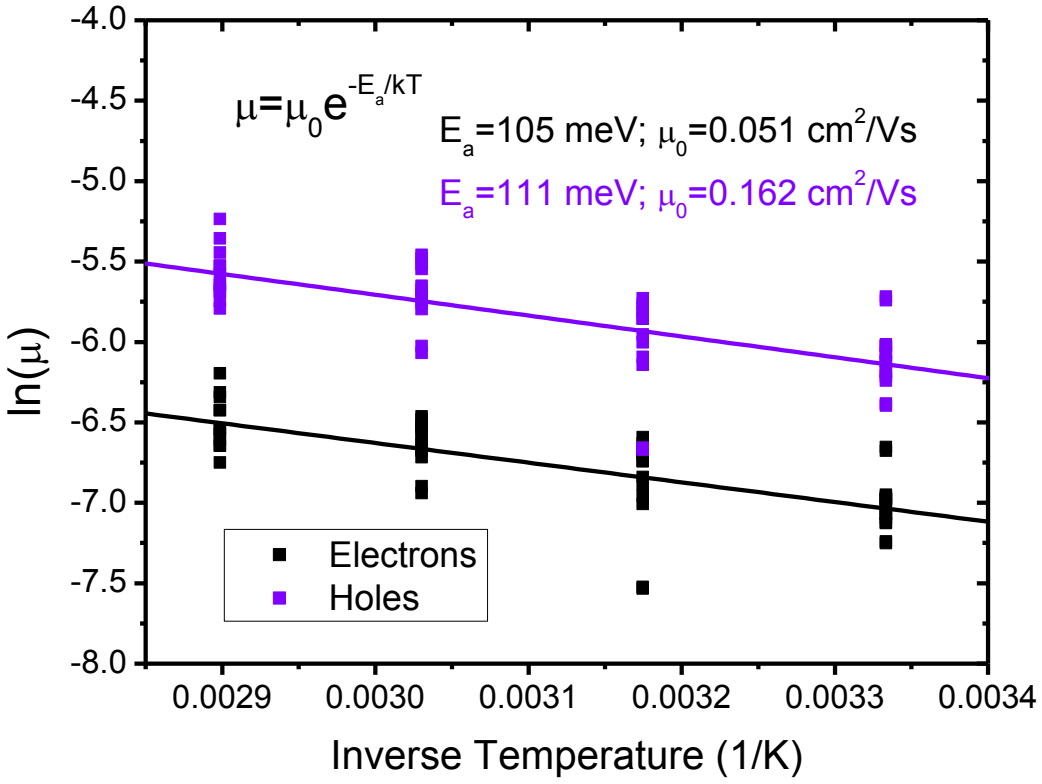

Figure 4.12: Natural logarithms of measured electron and hole mobilities with respect to inverse temperature for P3HT:$PC_{71}BM$ lateral devices under 100 mW/cm^2 AM1.5 illumination.

The thermal activation energies are very similar and close to the peak population of trap energies at 100 meV in P3HT:PCBM films [97, 98]. By modifying the solvent system used in the preparation of the P3HT:$PC_{71}BM$ film, we have increased the population of electron traps, rather than modifying the electron trap depths, to reduce the mobility ratio. In this modified BHJ system, the carrier concentration and bimolecular recombination coefficient under full 100 mW/cm^2 AM1.5 illumination are more stable with temperature (Figure 4.13). However, as in the previous P3HT:$PC_{71}BM$ temperature dependent measurement, the recombination zone conductivity at high light intensities decreased. As the mobility ratio did not change, this is attributable to an increase in the recombination coefficient and decrease in the carrier concentration in the bulk P3HT:$PC_{71}BM$. This can be seen in the intensity and temperature dependent data in Figure 4.14. The ratio between the non-Langevin and Langevin recombination coefficients increased slightly but remained on the order of 10^{-3}.

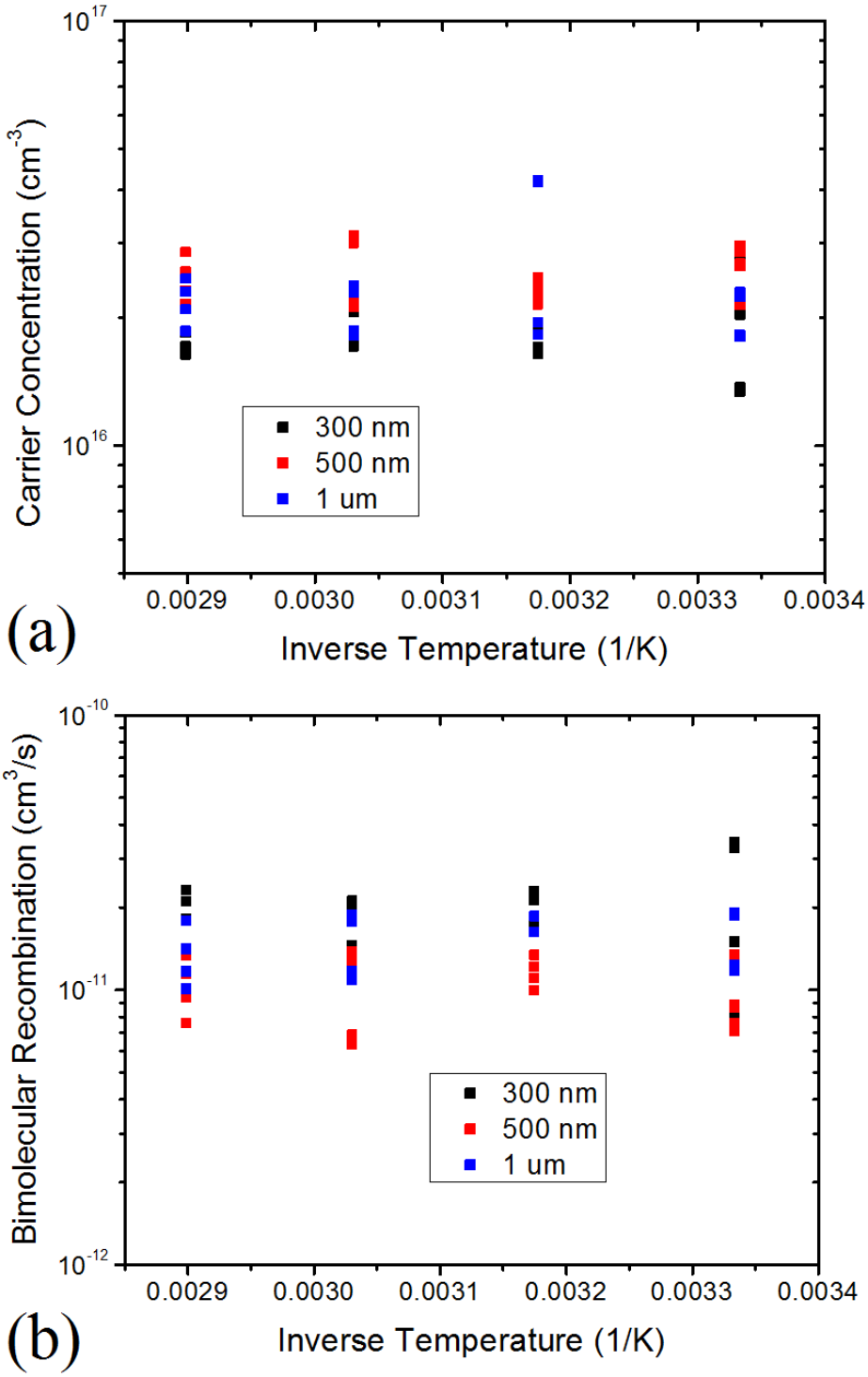

Figure 4.13: Carrier concentration (a) and bimolecular recombination coefficient (b) with respect to inverse temperature. Calculated from SCL mobility and conductivity measurements of P3HT:$PC_{71}BM$ lateral devices with different electron and hole mobilities under 100 mW/cm^2 AM1.5 illumination.

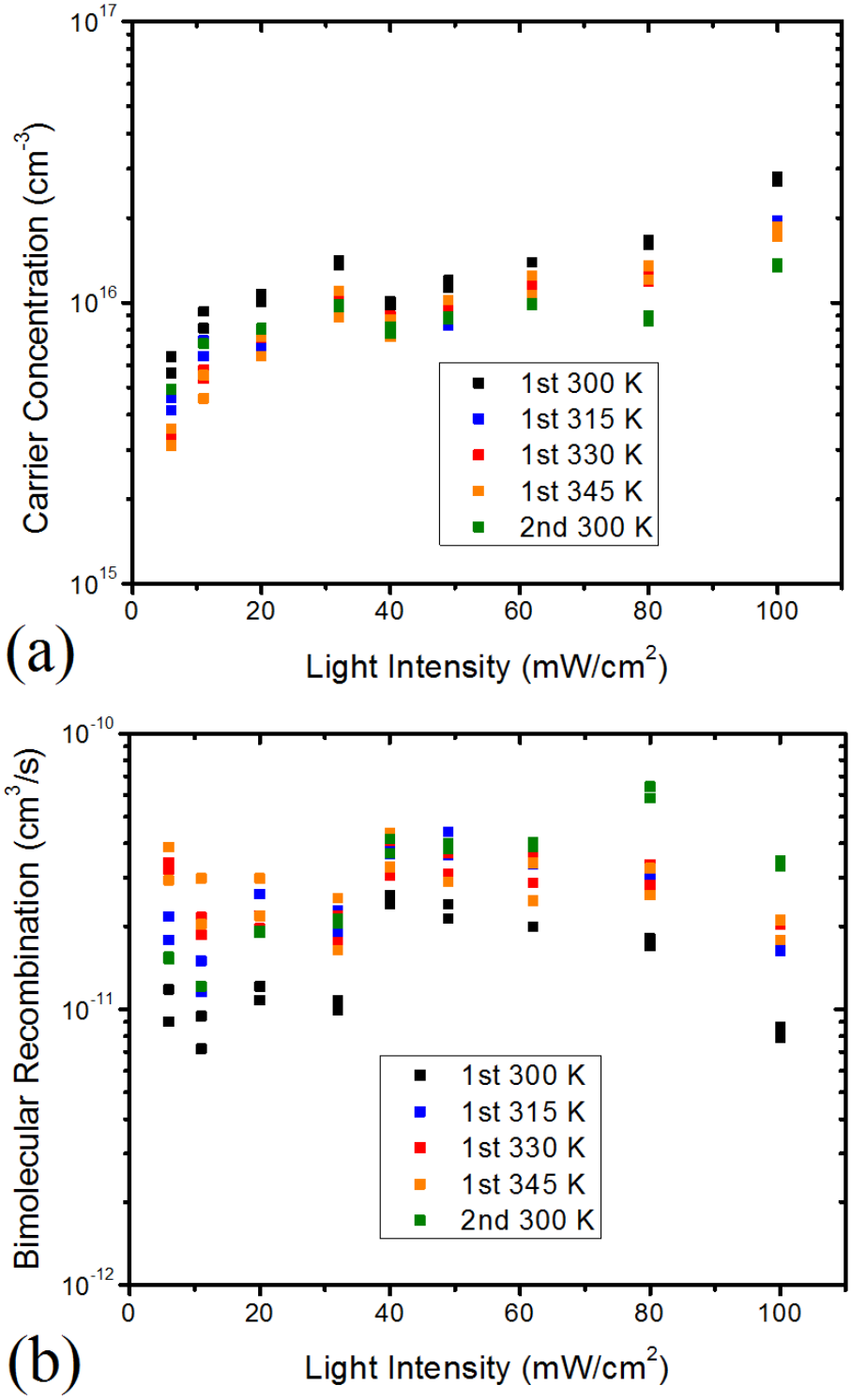

Figure 4.14: Carrier concentration (a) and bimolecular recombination coefficient (b) with respect to incident AM1.5 light intensity at different temperatures. Calculated from the SCL mobilities in Figure 4.12 and recombination zone conductivity measurements of large P3HT:$PC_{71}BM$ lateral devices.

Chapter 5: Geminate Recombination

5.1 Introduction

In organic photovoltaic (OPV) cells, after the photogeneration of charges, the electron and hole remain Coulombically bound as an exciton. These excitons have a high binding energy and cannot be dissociated by the electric fields present in OPV cells under operation or by the ambient thermal energy. In organic bulk heterojunction (BHJ) materials, the exciton diffuses to an interface between the electron donor and acceptor (D/A interface), where it can separate due to the difference in energy levels between the donor and acceptor. At the interface, the electron and hole form a charge transfer (CT) state with the electron on the acceptor and the hole on the donor [100, 101]. If the binding energy of the CT state is overcome, the carriers are separated and can exit the device through percolation pathways in the BHJ.

At several points during this process, the exciton may recombine and the energy from the incident photon lost. Recombinaton involving a single electron-hole pair which originated from a single photon is known as geminate recombination. Geminate recombination is considered to be a monomolecular process independent of the total geminate pair density and can occur through multiple pathways. The exciton may not reach a D/A interface in its lifetime and relax back to its ground state, or the exciton may recombine through a CT state. At the D/A interface, multiple CT states exist which vary in energy and width depending on their delocalization and the material characteristics of the donor and acceptor. Hot CT states are more delocalized and allow electron-hole pairs to be separated easily by decreasing their Coulombic attraction [100-103]. These hot CT states can also be at higher energies than the LUMO of the electron acceptor, making charge separation more energetically favorable. Excitons occupying cooler CT states may need additional energy to dissociate and can recombine through the CT state. An energy level diagram of the photogeneration and separation process illustrating these two main geminate recombination pathways is shown in Figure 5.1.

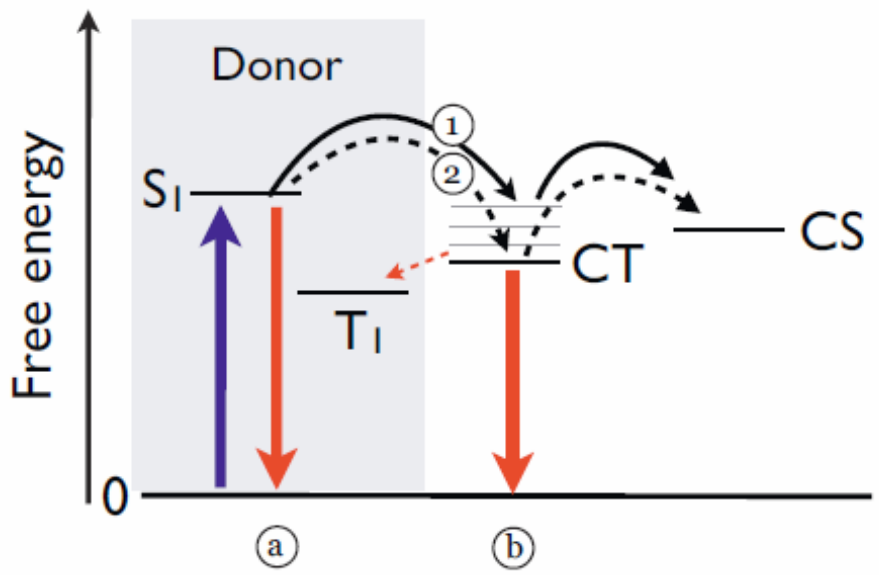

Figure 5.1: Jablonski diagram illustrating the different mechanisms of charge separation at a BHJ interface and geminate recombination. The red arrow labeled (a) indicates the decay of an exciton before it can make to the interface while the red arrow labeled (b) indicates geminate recombination at the D/A interface through the CT state. The arrows labeled (1) and (2) indicate charge separation through hot and "cool" CT states at the interface. The red dashed arrow indicates recombination into the triplet state. [24]

Geminate recombination can become a significant loss mechanism in BHJ systems with enlarged material domains, where photogenerated excitons cannot reach the D/A interface within their lifetime. A high trap density in the BHJ may also increase geminate recombination by reducing delocalization at the D/A interface and making recombination through a CT state more probable [104]. Although geminate recombination has been shown to be non-dominant in P3HT:PCBM solar cells [22], there are many other BHJ systems in which geminate recombination losses can significantly affect the photocurrent of OPV cells [105-107]. Geminate recombination and CT state dynamics in organic BHJ systems have been investigated using photoluminescence (PL) spectroscopy [108, 109], and a variety of two-photon spectroscopy techniques [24, 101, 102]. However, these time-resolved transient measurements are usually performed on pristine films, and the effect of geminate recombination is not often considered in reliability and lifetime studies of OPV cells.

Lateral devices offer a unique way to separate out the effects of geminate and nongeminate recombination in degradation studies. Previous sections have discussed how conductivity measurements in the central recombination zone of large lateral devices can be used to calculation the bimolecular recombination rate and distinguish between nongeminate recombination mechanisms. Under conditions similar to OPV device operation, the channel of small lateral devices (with channel lengths ≤ 1 μm) are dominated by one space charge region (SCR) with high concentrations of the slower mobility carrier. The faster carriers exit the device quickly, while the slower carriers accumulate in the device. This buildup of space charge distorts the applied electric field and the device exhibits space charge limited (SCL) photocurrent. The presence of SCL photocurrent behavior is dependent on the high carrier density within the BHJ material. Therefore if the photogeneration rate is reduced by increased geminate recombination, the SCL behavior in these small lateral devices will be affected. By monitoring the SCL behavior of small lateral BHJ devices with respect to time, and comparing these results with initial measurements made at low light intensities, we are able to track the decrease in photogeneration with time due to increased geminate recombination in BHJ materials.

5.2 Effect of Extended Light Exposure

Changes in the recombination characteristics, as well as film degradation, have been observed in organic BHJ materials upon exposure to light for extended periods of time [84, 85, 110]. We initially investigated the effect of long term light exposure on lateral BHJ devices in order to correct for this process during other long term experiments, such as the introduction of ethanol vapor or temperature dependent studies.

The BHJ absorber layer was deposited from a 20 mg/mL solution of P3HT:$PC_{71}BM$ (1:1 by weight) in 1,2-dichlorobenzene that had been heated to 50ºC and stirred for over 16 h. The BHJ was spun cast at 1200 rpm for 60 s, followed by annealing at 145ºC for 15 min in a nitrogen

atmosphere. Electrical measurements were performed in a *Desert Cryogenics* cryogenic probe station under vacuum better than 5×10^{-5} torr at 300 K. The sample was kept under vacuum and measured over a period of 4 days. Sample illumination was achieved using an *Oriel model 66912* 150 W xenon lamp, modified using an AM1.5 spectral filter. The incident light intensity was varied from 6 to 100 mW/cm^2 using neutral density filters. The sample was kept continuously illuminated under the AM1.5 light source at an intensity of 100 mW/cm^2 between measurements.

Initial SCL carrier mobility measurements from the small lateral devices were successful and found to be approximately 1.85 and 3.63×10^{-4} cm^2/Vs, with electrons as the slower carrier. These measurements were repeated after 6 hours of light exposure, with similar but slightly reduced SCL carrier mobilities. The mobility ratio measurements from the larger 50 μm device were consistent between these two initial measurements. After 24 hours of light exposure, however, SCL behavior was no longer observed in the photocurrent characteristics of the lateral BHJ devices, as shown in Figure 5.2 below:

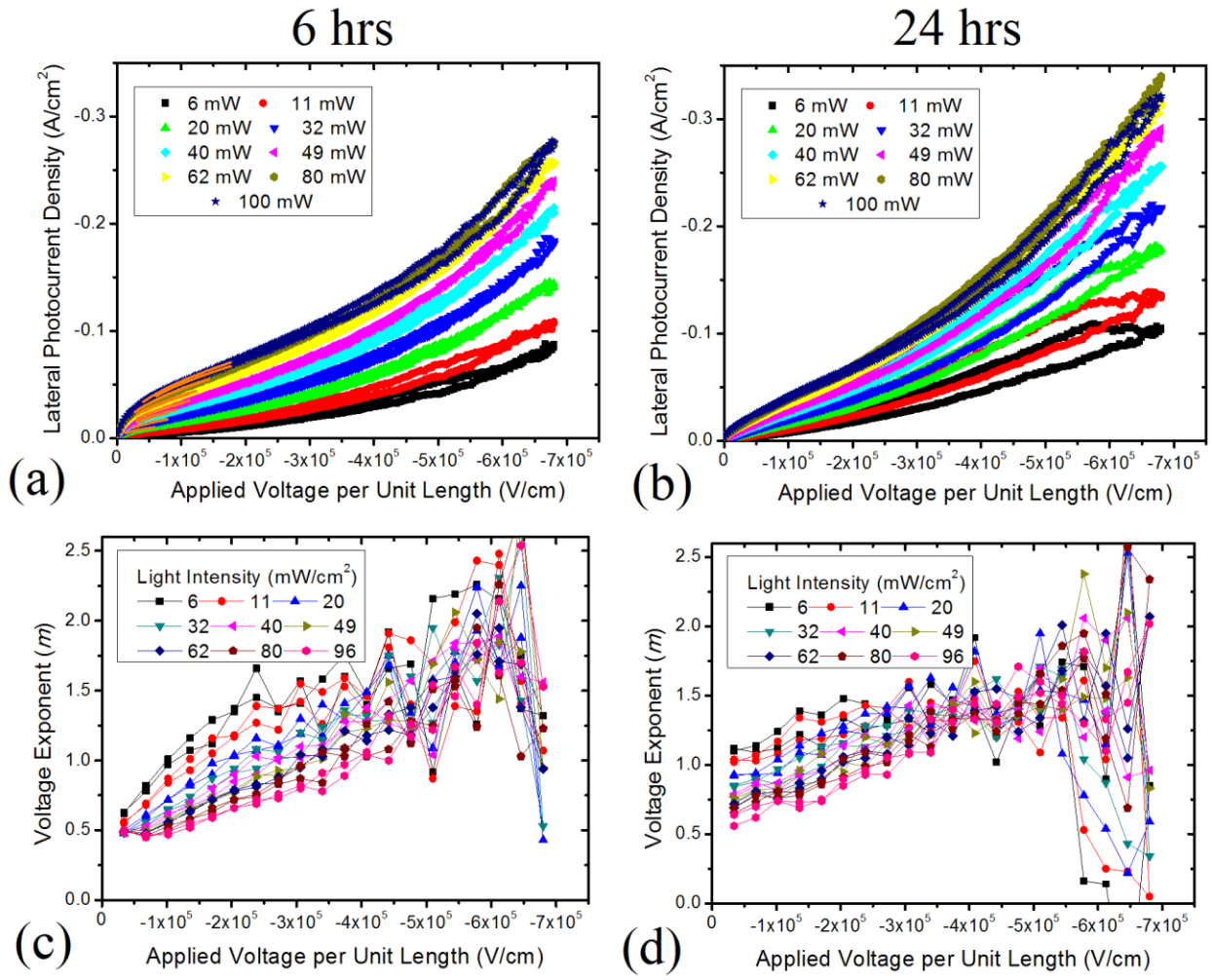

Figure 5.2: Lateral photocurrent density (a,b) and voltage exponent (c,d) vs. applied voltage per unit length for a 500 nm lateral P3HT:$PC_{71}BM$ device illuminated by varying AM1.5 light intensities after 6 (a,c) and 24 (b,d) hours of 100 mW/cm^2 light exposure. The orange lines in Figure 4.8a indicate the voltage range in which SCL transport is prevalent and the carrier mobility was calculated.

Initially, SCL behavior is observed in the photocurrent behavior of the small lateral BHJ device, especially at high light intensities. The value of the voltage exponent (m) in the range $\leq 1 \times 10^5$ V/cm is equal to 0.5, allowing us to fit Equation 4.3 over this range and calculate the slower carrier mobility. At low light intensities, this behavior is not observed; the exponent begins at approximately 0.6 and immediately rises due to increasing injection from the contacts. Due to low photogeneration of charge carriers at these intensities, space charge cannot be built

up in the lateral BHJ device adjacent to the contacts, and the contacts inject carriers more efficiently into the device. After 24 hours of light exposure, the device no longer exhibits SCL behavior even at high illumination intensities. Photocurrent measurements at all intensities are injection dominated. This change in voltage exponent behavior over time can be clearly seen in Figure 5.3:

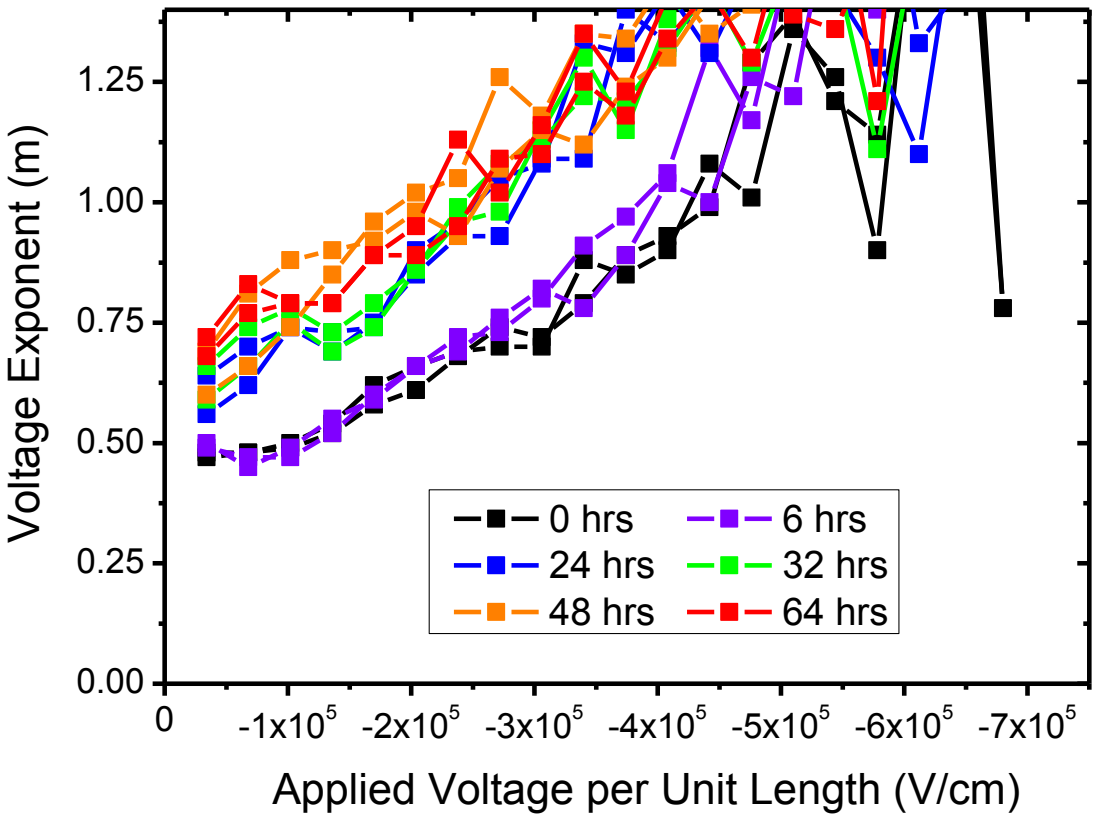

Figure 5.3: Voltage exponent vs. applied voltage per unit length for the same 500 nm lateral P3HT:$PC_{71}BM$ device under 100 mW/cm^2 AM1.5 illumination after continual light exposure.

All high light intensity measurements made after 24 hours show no SCL behavior. The voltage exponent begins at a value larger than 0.5 and increases steadily. This behavior is consistent with the original voltage exponent behavior measured at low light intensities. The initial value of the voltage exponent and the slope increases with light exposure time, stabilizing after 48 hrs.

Due to the absence of SCL behavior at later times, we cannot extract the carrier mobilities using our lateral device model. However, we can infer from this disappearance of SCL behavior that the recombination mechanism of the system must have changed over the course of the experiment. In order to observe SCL photocurrents, the number of photogenerated charge carriers must be large and the material system should have a low mobility [61]. From our initial measurements, we know that the sample exhibited a low mobility with unbalanced charge transport. The magnitude of the photocurrent also did not change significantly after 24 hrs of light exposure, which suggests that the mobility and nongeminate recombination rates of carriers within the material remained relatively constant. SCL measurements after 6 hours do show a slight decrease in the carrier mobilities, but we have previously measured SCL photocurrent behavior in BHJ systems with significantly lower mobilities. In addition, this apparent decrease in the SCL mobility may also be due to the decrease in the photogeneration rate, which is included in the lateral SCL Equation 4.3, reproduced here:

$$J_{ph} = \chi\sqrt{2}(\varepsilon\mu)^{\frac{1}{4}}(eG)^{\frac{3}{4}}(V + E_r d)^{\frac{1}{2}} \qquad (5.1)$$

The reduction in J_{ph} after 6 hours of light exposure could therefore be caused by a decrease in the electron mobility from 1.85 to 1.14 × 10^{-4} cm^2/Vs, or by a decrease in G to 90% of its initial value.

To remove the observed SCL behavior entirely, there must have been a large increase in the geminate recombination rate. If the number of photogenerated charge carriers decreased, not enough space charge would be built up in the device to cause the SCL photocurrent behavior described by Equation 5.1. The absorbance of the P3HT:PC_{71}BM film is not known to be affected by light exposure in an inert atmosphere for less than 1000 hours [84, 85], therefore an increase in the geminate recombination rate is a more likely cause.

From this change in voltage exponent behavior, we can estimate the change in the photogeneration rate due to increased geminate recombination. The voltage exponent curves

from later photocurrent measurements in Figure 5.4 were compared and matched with the voltage exponent curves from initial low intensity measurements. From this comparison, we estimate the decrease in the photogeneration rate over time, compared to the initial value:

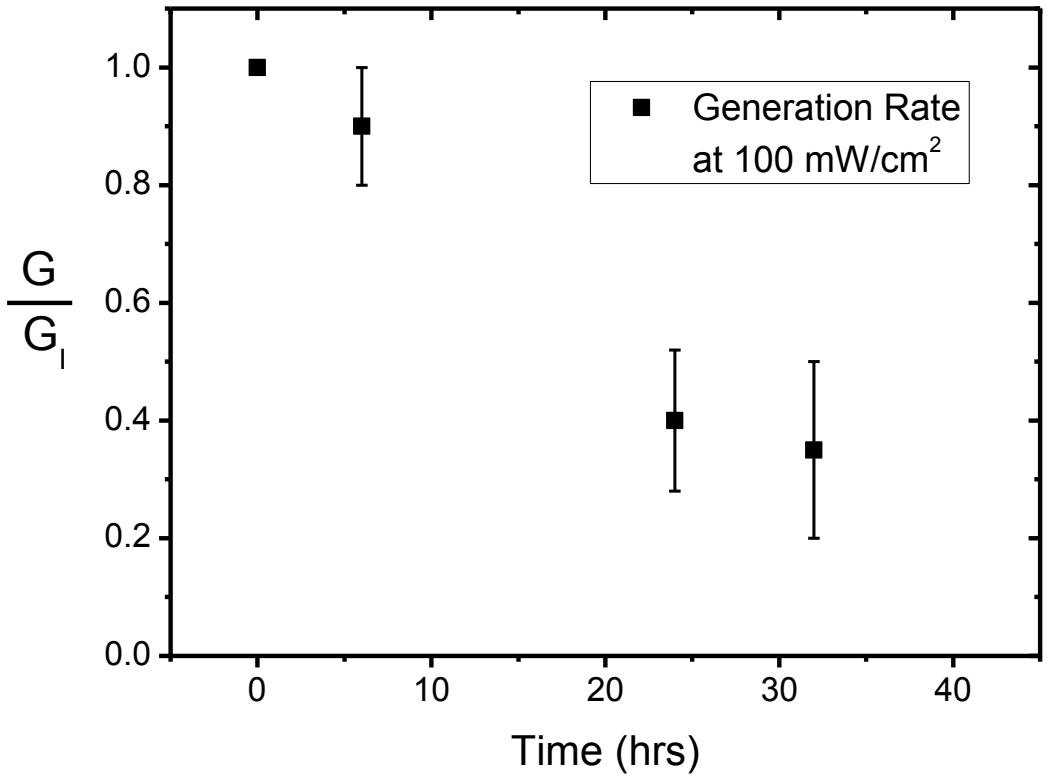

Figure 5.4: Change in generation rate (G) relative to the initial value (G_I) over time after continued light exposure. G is estimated at later times relative to G_I using the initial low intensity voltage exponent behavior.

The error bars in Figure 5.4 are estimated from the range of voltage exponent curves at different low light intensities which match the voltage exponent behavior after a certain light exposure time. At later times, the voltage exponent curves could not be easily compared with the low intensity exponent behavior and are not included in the plot. The voltage exponent curves after 48 hours begin at very high values and do not easily match low intensity exponent behavior over the applied field range where SCL behavior is expected. This could be indicative of a change in the contacts of the device, limiting the extraction of photogenerated carriers. The upper limits of the error bars can also be inferred from the reduction in lateral photocurrent density.

The initial decrease in G after 6 hours is estimated from the change in J_{ph}, but could also be caused by a slight decrease in the electron mobility, as explained above. The larger change in photocurrent density and voltage exponent behavior at later times cannot be explained by a change in the carrier mobilities. It is clear from this plot that a significant reduction in the photogeneration rate due to increased geminate recombination must occur in order to eliminate the SCL behavior in these small lateral BHJ devices. This increase in geminate recombination of the BHJ film will have significant effects on the long-term performance of OPV cells. The effective generation rate at an incident light intensity of 100 mW/cm^2 drops by over a factor of two for this P3HT:PC$_{71}$BM film over 24 hours of continuous light exposure. This is supported by the lateral photocurrent measurements, shown in Figure 5.5:

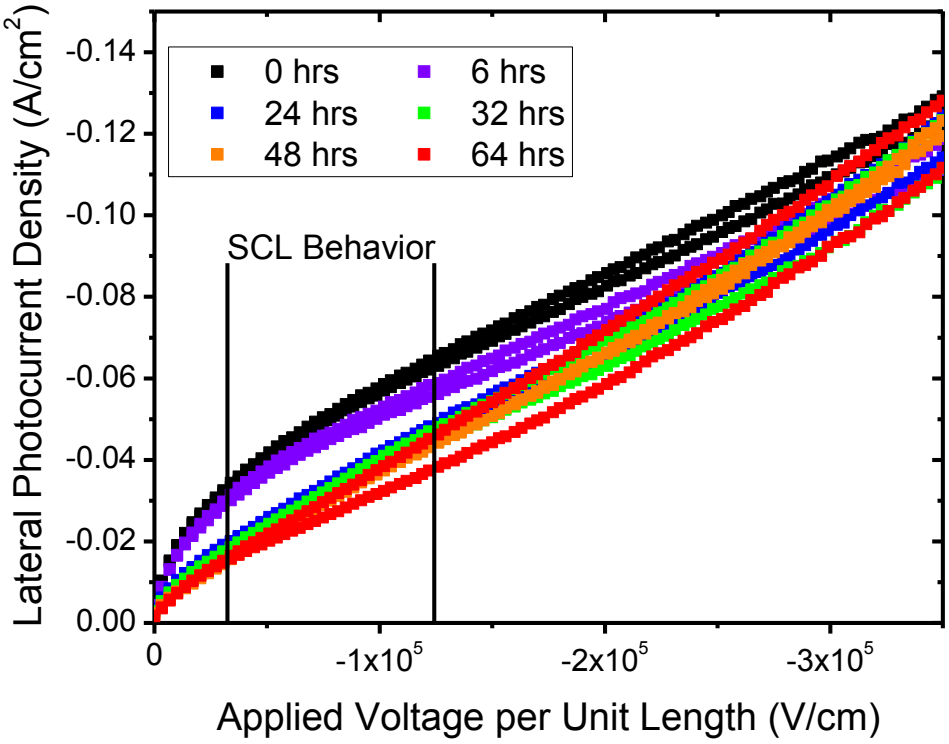

Figure 5.5: Lateral photocurrent density vs. applied voltage per unit length for the same 500 nm lateral P3HT:PC$_{71}$BM device under 100 mW/cm^2 AM1.5 illumination after continual light exposure. The range over which SCL behavior was initially observed is indicated on the plot.

As expected from the estimated drop in geminate recombination and voltage exponent curves, there is a small initial decrease in the photocurrent after 6 hours, and then a more significant decrease after 24 hours where the SCL behavior is significantly diminished. The lateral device photocurrents decrease by approximately a factor of two over the entire light exposure period, in the applied field range where SCL behavior was originally dominant. This gives us an upper limit on the change in the geminate recombination rate, although the current could be enhanced slightly over this applied field range due to enhanced injection from the contacts.

Geminate recombination in organic BHJ materials is not often considered in reliability and lifetime studies, but it is an important component of light exposure degradation in these materials. Using small lateral device measurements, we are able to isolate the effects of geminate and nongeminate recombination and investigate them separately in degradation studies. Although the change in contact extraction behavior limits the use of this technique over long time periods (>24 hrs), we are able to estimate the change in the geminate recombination rate in the BHJ film and track its effect on the photocurrent of small lateral devices. The exact mechanism for this change cannot be determined from these current vs. voltage measurements alone, but we hypothesize that the increased geminate recombination rate emerges from a large population of electron traps which increase with light exposure time. The observed decrease in electron mobility is consistent with this explanation, but the larger trap density would also have significant effects on the generation rate. Electron traps close to the D/A interface would result in reduced delocalization of the exciton at the D/A interface and increases the probability of recombination through the CT state [24, 104].

References

1. Green, M.A., et al., *Solar cell efficiency tables (version 42).* Progress in Photovoltaics: Research and Applications, 2013. **21**(5): p. 827-837.
2. Hoppe, H. and N.S. Sariciftci, *Organic solar cells: An overview.* Journal of Materials Research, 2004. **19**(7): p. 1924-1945.
3. Brabec, C.J., *Organic photovoltaics: technology and market.* Solar Energy Materials & Solar Cells, 2004. **83**: p. 273-292.
4. Fozdar, D.Y., et al., *Nano/Microfabrication Techniques for Organic Electronics and Photonics*, in *Handbook of Organic Electronics and Photonics*, H.S. Nalwa, Editor. 2006, American Scientific Publishers. p. 1-25.
5. Bredas, J.L., et al., *Organic semiconductors: A theoretical characterization of basic parameters governing charge transport.* Proceedings of the National Academy of Sciences, 2002. **99**(9): p. 5804-5809.
6. Coropceanu, V., et al., *Charge Transport in Organic Semiconductors.* Chemical Reviews, 2007. **107**: p. 926-952.
7. Gomes da Costa, P. and E.M. Conwell, *Excitons and the band gap in poly(phenylene vinylene).* Physical Review B, 1993. **48**(3): p. 1993.
8. Blom, P.W.M., et al., *Device Physics of Polymer:Fullerene Bulk Heterojunction Solar Cells.* Advanced Materials, 2007. **19**: p. 1551-1566.
9. Tang, C.W., *Twolayer organic photovoltaic cell.* Applied Physics Letters, 1986. **48**: p. 183-185.
10. Chen, Y., et al., *A new solution-processed diketopyrrolopyrrole donor for non-fullerene small-molecule solar cells.* Journal of Materials Chemistry A, 2014. **2**(6): p. 1869-1876.
11. Qu, J., et al., *Donor-spacer-acceptor monodisperse conjugated co-oligomers for efficient single-molecule photovoltaic cells based on non-fullerene acceptors.* Journal of Materials Chemistry A, 2014. **2**(10): p. 3632-3640.
12. Wolfer, P., et al., *Indentifying the optimum composition in organic solar cells comprising non-fullerene electron acceptors.* Journal of Materials Chemistry A, 2013. **1**(19): p. 5989-5995.
13. Ballantyne, A.M., et al., *The Effect of Poly(3-hexylthiophene) Molecular Weight on Charge Transport and the Performance of Polymer:Fullerene Solar Cells.* Advanced Functional Materials, 2008. **18**(16): p. 2373-2380.
14. Li, G., et al., *Manipulating regioregular poly(3-hexylthiophene): [6,6]-phenyl-C61-butryic acid methyl ester blends-route towards high efficiency polymer solar cells.* Journal of Materials Chemistry, 2007. **17**(30): p. 3126-3140.
15. Peumans, P., A. Yakimov, and S.R. Forrest, *Small molecular weight organic thin-film photodetectors and solar cells.* Journal of Applied Physics, 2003. **93**(7): p. 3693-3723.
16. Lunt, R.R., et al., *Exciton diffusion lengths of organic semiconductor thin films measured by spectrally resolved photoluminescence quenching.* Journal of Applied Physics, 2009. **105**.
17. Forrest, S.R., *The Limits to Organic Photovoltaic Cell Efficiency.* MRS Bulletin, 2005. **30**: p. 28-32.
18. Granstrom, M., et al., *Laminated fabrication of polymeric photovoltaic diodes.* Nature, 1998. **395**(6699): p. 257-260.
19. Yu, G., et al., *Polymer Photovoltaic Cells: Enhanced Efficiencies via a Network of Internal Donor-Acceptor Heterojunctions.* Science, 1995. **270**: p. 1789-1791.
20. Shockley, W. and H.J. Queisser, *Detailed Balance Limit of Efficiency of p-n Junction Solar Cells.* Journal of Applied Physics, 1961. **32**(3): p. 510-519.
21. Vandewal, K., et al., *On the origin of the open-circuit voltage of polymer-fullerene solar cells.* Nature Materials, 2009. **8**(11): p. 904-909.

22. Street, R.A., S.R. Cowan, and A.J. Heeger, *Experimental test for geminate recombination applied to organic solar cells.* Physical Review B, 2010. **82**: p. 121301.
23. Street, R.A., et al., *Interface state recombination in organic solar cells.* Physical Review B, 2010. **81**: p. 205307.
24. Proctor, C.M., M. Kuik, and T.-Q. Nguyen, *Charge carrier recombination in organic solar cells.* Progress in Polymer Science, 2013. **38**(12): p. 1941-1960.
25. Pivrikas, A., et al., *Time-dependent Langevin-type bimolecular charge carrier recombination in regiorandom poly(3-hexylthiophene).* Synthetic Metals, 2005. **155**(2): p. 242-245.
26. Juska, G., et al., *Two dimensional Langevin recombination in regioregular poly(3-hexylthiophene).* Applied Physics Letters, 2009. **95**(1): p. 013303.
27. Koster, L.J.A., V.D. Mihailetchi, and P.W.M. Blom, *Bimolecular recombination in polymer/fullerene bulk heterojunction solar cells.* Applied Physics Letters, 2006. **88**: p. 052104.
28. Pivrikas, A., et al., *A Review of Charge Transport and Recombination in Polymer/Fullerene Organic Solar Cells.* Progress in Photovoltaics: Research and Applications, 2007. **15**(8): p. 677-696.
29. Sliauzys, G., et al., *Recombination of photogenerated and injected charge carriers in pi-conjugated polymer/fullerene blends.* Thin Solid Films, 2006. **511-512**: p. 224-227.
30. Liu, A., et al., *Control of Electric Field Strength and Orientation at the Donor-Acceptor Interface in Organic Solar Cells.* Advanced Materials, 2008. **20**(5): p. 1065-1070.
31. Mihailetchi, V.D., et al., *Photocurrent Generation in Polymer-Fullerene Bulk Heterojunctions.* Physical Review Letters, 2004. **93**(21): p. 216601.
32. Veldman, D., et al., *Compositional and Electric Field Dependence of the Dissociation of Charge Transfer Excitons in Alternating Polyfluorene Copolymer/Fullerene Blends.* Journal of the American Chemical Society, 2008. **130**: p. 7721-7735.
33. Shuttle, C.G., et al., *Bimolecular recombination losses in polythiophene: Fullerene solar cells.* Physical Review B, 2008. **78**: p. 113201.
34. Koster, L.J.A., et al., *Quantifying Bimolecular Recombination Losses in Organic Bulk Heterojunction Solar Cells.* Advanced Materials, 2011. **23**(14): p. 1670-1674.
35. Cowan, S.R., A. Roy, and A.J. Heeger, *Recombination in polymer-fullerene bulk heterojunction solar cells.* Physical Review B, 2010. **82**(24): p. 245207.
36. Scharber, M.C. and N.S. Sariciftci, *Efficiency of bulk-heterojunction organic solar cells.* Progress in Polymer Science, 2013. **38**(12): p. 1929-1940.
37. Scharber, M., et al., *Design Rules for Donors in Bulk-Heterojunction Solar Cells - Towards 10% Energy-Conversion Efficiency.* Advanced Materials, 2006. **18**(6): p. 789-794.
38. Tiwari, S. and N.C. Greenham, *Charge mobility measurement techniques in organic semiconductors.* Optical and Quantum Electronics, 2009. **41**: p. 69-89.
39. Morfa, A.J., et al., *Time-of-Flight Studies of Electron-Collection Kinetics in Polymer:Fullerene Bulk-Heterojunction Solar Cells.* Advanced Functional Materials, 2011. **21**(13): p. 2580-2586.
40. Choulis, S.A., et al., *Investigation of transport properties in polymer/fullerene blends using time-of-flight photocurrent measurements.* Applied Physics Letters, 2003. **83**(18): p. 3812-3814.
41. Juska, G., et al., *Extraction Current Transients: New Method of Study of Charge Transport in Microcrystalline Silicon.* Physical Review Letters, 2000. **84**(21): p. 4946-4949.
42. Mozer, A.J., et al., *Charge transport and recombination in bulk heterojunction solar cells studied by the photoinduced charge extraction in linearly increasing voltage technique.* Applied Physics Letters, 2005. **86**(11): p. 112104.
43. Dennler, G., et al., *Charge carrier mobility and lifetime versus composition of conjugated polymer/fullerene bulk-heterojunction solar cells.* Organic Electronics, 2006. **7**(4): p. 229-234.

44. Mozer, A.J., et al., *Time-dependent mobility and recombination of the photoinduced charge carriers in conjugated polymer/fullerene bulk heterojunction solar cells.* Physical Review B, 2005. **72**: p. 035217.
45. Chen, S., et al., *Photo-Carrier Recombination in Polymer Solar Cells Based on P3HT and Silole-Based Copolymer.* Advanced Energy Materials, 2011. **1**(5): p. 963-969.
46. Rost, C., et al., *Ambipolar light-emitting organic field-effect transistor.* Applied Physics Letters, 2004. **85**(9): p. 1613-1615.
47. Dodabalapur, A., et al., *Organic Heterostructure Field-Effect Transistors.* Science, 1995. **269**: p. 1560-1562.
48. Shuttle, C.G., et al., *Charge extraction analysis of charge carrier densities in a polythiophene/fullerene solar cell: Analysis of the origin of the device dark current.* Applied Physics Letters, 2008. **93**: p. 183501.
49. Rauh, D., C. Deibel, and V. Dyakonov, *Charge Density Dependent Nongeminate Recombination in Organic Bulk Heterojunction Solar Cells.* Advanced Functional Materials, 2012. **22**(16): p. 3371-3377.
50. Cowan, S.R., et al., *Transient photoconductivity in polymer bulk heterojunction solar cells: Competition between sweep-out and recombination.* Physical Review B, 2011. **83**(3): p. 035205.
51. Garcia-Belmonte, G., et al., *Charge carrier mobility and lifetime of organic bulk heterojunctions analyzed by impedance spectroscopy.* Organic Electronics, 2008. **9**: p. 847-851.
52. Leever, B.J., et al., *In Situ Characterization of Lifetime and Morphology in Operating Bulk Heterojunction Organic Photovoltaic Devices by Impedance Spectroscopy.* Advanced Energy Materials, 2011. **2**(1): p. 120-128.
53. Koster, L.J.A., et al., *Light intensity dependence of open-circuit voltage of polymer:fullerene solar cells.* Applied Physics Letters, 2005. **86**: p. 123509.
54. Dibb, G.F.A., et al., *Analysis of the Relationship between Linearity of Corrected Photocurrent and the Order of Recombination in Organic Solar Cells.* The Journal of Physical Chemistry Letters, 2011. **2**(19): p. 2407-2411.
55. Li, J.V., et al., *Simultaneous measurement of carrier density and mobility of organic semiconductors using capacitance techniques.* Organic Electronics, 2011. **12**(11): p. 1879-1885.
56. Leong, W.L., S.R. Cowan, and A.J. Heeger, *Differential Resistance Analysis of Charge Carrier Losses in Organic Bulk Heterojunction Solar Cells: Observing the Transition from Bimolecular to Trap-Assisted Recombination and Quantifying the Order of Recombination.* Advanced Energy Materials, 2011. **1**(4): p. 517-522.
57. Ai, X., et al., *Photoinduced Charge Carrier Generation in a Poly(3-hexylthiophene) and Methanofullerene Bulk Heterojunction Investigated by Time-Resolved Terahertz Spectroscopy.* Journal of Physical Chemistry B, 2006. **110**(50): p. 25462-25471.
58. Baumann, A., et al., *Influence of Phase Segregation on Recombination Dynamics in Organic Bulk-Heterojunction Solar Cells.* Advanced Functional Materials, 2011. **21**(9): p. 1687-1692.
59. Chan, K.K.H., et al., *Charge injection and transport studies of poly(2,7-carbazole) copolymer PCDTBT and their relationship to solar cell performance.* Organic Electronics, 2012. **13**(5): p. 850-855.
60. Goodman, A.M. and A. Rose, *Double Extraction of Uniformly Generated Electron-Hole Pairs from Insulators with Noninjecting Contacts.* Journal of Applied Physics, 1971. **42**(7): p. 2823-2830.
61. Mihailetchi, V.D., J. Wildeman, and P.W.M. Blom, *Space-Charge Limited Photocurrent.* Physical Review Letters, 2005. **94**(12): p. 126602.
62. Ooi, Z.E., et al., *Analysis of photocurrents in lateral-geometry organic bulk heterojunction devices.* Applied Physics Letters, 2012. **101**(5): p. 053301.

63. Ooi, Z.E., et al., *Evaluating charge carrier mobility balance in organic bulk heterojunctions using lateral device structures.* Journal of Physical Chemistry C, 2014. **In Press**.
64. Lombardo, C., et al., *Device physics and operation of lateral bulk heterojunction devices.* The Journal of Physical Chemistry B, 2013. **117**(16): p. 4503-4509.
65. Lombardo, C., et al., *Scanning photocurrent microscopy of lateral organic bulk heterojunctions.* Physical Chemistry Chemical Physics, 2012. **14**(38): p. 13199-13203.
66. Morris, J.D., et al., *Mapping Electric Field Distributions in Biased Organic Bulk Heterojunctions Under Illumination by Nonlinear Optical Microscopy.* Applied Physics Letters, 2013. **102**(3): p. 033301.
67. Morris, J.D., et al., *Quantifying space charge accumulation in organic bulk heterojunctions by nonlinear optical microscopy.* Organic Electronics, 2013. **14**(11): p. 3014-3018.
68. Cho, S., et al., *Photovoltaic effects on the organic ambipolar field-effect transistors.* Applied Physics Letters, 2007. **90**: p. 063511.
69. Cho, S., et al., *Ambipolar organic field-effect transistors fabricated using a composite of semiconducting polymer and soluble fullerene.* Applied Physics Letters, 2006. **89**: p. 153505.
70. Lombardo, C., et al., *Lateral mobility measurements in organic bulk heterojunctions: comparison of field-effect and space charge mobilities.* Journal of Photonics for Energy, 2012. **2**(1): p. 021007.
71. Lombardo, C., et al., *Electrical characteristics of lateral organic bulk heterojunction structures.* Organic Electronics, 2012. **13**(7): p. 1185-1191.
72. Mihailetchi, V.D., et al., *Cathode dependence of the open-circuit voltage of polymer:fullerene bulk heterojunction solar cells.* Journal of Applied Physics, 2003. **94**(10): p. 6849-6854.
73. Mihailetchi, V.D., et al., *Charge Transport and Photocurrent Generation in Poly(3-hexylthiophene):Methanofullerene Bulk-Heterojunction Solar Cells.* Advanced Functional Materials, 2006. **16**(5): p. 699-708.
74. Chellappan, V., et al., *Imbalanced charge mobility in oxygen treated polythiophene/fullerene based bulk heterojunction solar cells.* Applied Physics Letters, 2009. **95**(26): p. 263305.
75. Chirvase, D., et al., *Electrical and optical design and characterisation of regioregular poly(3-hexylthiophene-2,5diyl)/fullerene-based heterojunction polymer solar cells.* Synthetic Metals, 2003. **138**(1-2): p. 299-304.
76. Danielson, E., et al., *Bimolecular recombination coefficient calculation by in situ potentiometry in a bulk heterojunction organic photovoltaic material.* Applied Physics Letters, 2013. **102**(17): p. 173304.
77. Deibel, C., A. Baumann, and V. Dyakonov, *Polaron recombination in pristine and annealed bulk heterojunction solar cells.* Applied Physics Letters, 2008. **93**(16).
78. Dunlap, D.H., V.M. Kenkre, and P.E. Parris, *What is Behind the Square Root of E?* Journal of Imaging Science and Technology, 1999. **43**(5): p. 437-443.
79. Wang, L., et al., *Electric-field-dependent charge transport in organic thin-film transistors.* Journal of Applied Physics, 2007. **101**(5).
80. Frenkel, J., *On Pre-Breakdown Phenomena in Insulators and Electronic Semi-Conductors.* Physical Review, 1938. **54**(8): p. 647-648.
81. Duarte, D., et al., *Charge transport and trapping in organic field effect transistors exposed to polar analytes.* Applied Physics Letters, 2011. **98**(13): p. 133302.
82. Duarte, D. and A. Dodabalapur, *Investigation of the physics of sensing in organic field effect transistor based sensors.* Journal of Applied Physics, 2012. **111**(4): p. 044509
83. Tournebize, A., et al., *New Insights into the Mechanisms of Photodegradation/Stabilization of P3HT:PCBM Active Layers Using Poly(3-hexyl-d13-Thiophene).* Chemistry of Materials, 2013. **25**(22): p. 4522-4528.

84. Brabec, C.J., et al., *Polymer-Fullerene Bulk-Heterojunction Solar Cells.* Advanced Materials, 2010. **22**: p. 3839-3856.
85. Reese, M.O., et al., *Photoinduced Degradation of Polymer and Polymer-Fullerene Active Layers: Experiment and Theory.* Advanced Functional Materials, 2010. **20**(20): p. 3476-3483.
86. Seemann, A., et al., *Reversible and irreversible degradation of organic solar cell performance by oxygen.* Solar Energy, 2011. **85**(6): p. 1238-1249.
87. Rogers, J.T., et al., *Structural Order in Bulk Heterojunction Films Prepared with Solvent Additives.* Advanced Materials, 2011. **23**(20): p. 2284-2288.
88. Collins, B.A., et al., *Absolute Measurement of Domain Composition and Nanoscale Size Distribution Explains Performance in PTB7:$PC_{71}BM$ Solar Cells.* Advanced Energy Materials, 2013. **3**(1): p. 65-74.
89. Dang, M.T., L. Hirsch, and G. Wantz, *P3HT:PCBM, Best Seller in Polymer Photovoltaic Research.* Advanced Materials, 2011. **XX**: p. 1-6.
90. Muller, C., et al., *Binary Organic Photovoltaic Blends: A Simple Rationale for Optimum Compositions.* Advanced Materials, 2008. **20**: p. 3510-3515.
91. Lange, A., et al., *Inkjet printed solar cell active layers prepared from chlorine-free solvent systems.* Solar Energy Materials & Solar Cells, 2013. **109**(0): p. 104-110.
92. Kim, M., et al., *Solar Cells: Electrical Performance of Organic Solar Cells with Additive-Assisted Vertical Phase Separation in the Photoactive Layer (Adv. Energy Mater. 2/2014).* Advanced Energy Materials, 2014. **4**(2): p. n/a-n/a.
93. Chang, L., et al., *Effect of Trace Solvent on the Morphology of P3HT:PCBM Bulk Heterojunction Solar Cells.* Advanced Functional Materials, 2011. **21**(10): p. 1779-1787.
94. Moule, A.J. and K. Meerholz, *Morphology Control in Solution-Processed Bulk-Heterojunction Solar Cell Mixtures.* Advanced Functional Materials, 2009. **19**(19): p. 3028-3036.
95. Lee, J.K., et al., *Processing Additives for Improved Efficiency from Bulk Heterojunction Solar Cells.* Journal of the American Chemical Society, 2008. **130**: p. 3619.
96. Morana, M., et al., *Organic Field-Effect Devices as Tool to Characterize the Bipolar Transport in Polymer-Fullerene Blends: The Case of P3HT-PCBM.* Advanced Functional Materials, 2007. **17**(16): p. 3274-3283.
97. Neugebauer, S., et al., *Investigation of electronic trap states in organic photovoltaic materials by current-based deep level transient spectroscopy.* Applied Physics Letters, 2012. **100**(26): p. -.
98. Schafferhans, J., C. Deibel, and V. Dyakonov, *Electronic Trap States in Methanofullerenes.* Advanced Energy Materials, 2011. **1**(4): p. 655-660.
99. Foertig, A., et al., *Charge carrier concentration and temperature dependent recombination in polymer-fullerene solar cells.* Applied Physics Letters, 2009. **95**(5).
100. Lee, J., et al., *Charge Transfer State Versus Hot Exciton Dissociation in Polymer-Fullerene Blended Solar Cells.* Journal of the American Chemical Society, 2010. **132**(34): p. 11878-11880.
101. Zhu, X., Q. Yang, and M. Muntwiler, *Charge-Transfer Excitons at Organic Semiconductor Surfaces and Interfaces.* Accounts of Chemical Research, 2009. **42**(11): p. 1779-1787.
102. Bakulin, A.A., et al., *Charge-Transfer State Dynamics Following Hole and Electron Transfer in Organic Photovoltaic Devices.* The Journal of Physical Chemistry Letters, 2012. **4**(1): p. 209-215.
103. Rao, M. and K.S. Narayan, *Studies of charge transfer processes across donor-acceptor interface using a field effect transistor geometry.* Applied Physics Letters, 2009. **95**.
104. Schwarz, C., et al., *Role of the effective mass and interfacial dipoles on exciton dissociation in organic donor-acceptor solar cells.* Physical Review B, 2013. **87**(15): p. 155205.
105. Deibel, C. and V. Dyakonov, *Polymer–fullerene bulk heterojunction solar cells.* Reports on Progress in Physics, 2010. **73**(9): p. 096401.

106. Pivrikas, A., H. Neugebauer, and N.S. Sariciftci, *Charge Carrier Lifetime and Recombination in Bulk Heterojunction Solar Cells.* Selected Topics in Quantum Electronics, IEEE Journal of, 2010. **16**(6): p. 1746-1758.
107. Cowan, S.R., et al., *Charge Formation, Recombination, and Sweep-Out Dynamics in Organic Solar Cells.* Advanced Functional Materials, 2012. **22**(6): p. 1116-1128.
108. Glowe, J.-F., et al., *Charge-transfer excitons in strongly coupled organic semiconductors.* Physical Review B, 2010. **81**.
109. Loi, M.A., et al., *Charge Transfer Excitons in Bulk Heterojunctions of Polyfluorene Copolymer and a Fullerene Derivative.* Advanced Functional Materials, 2007. **17**: p. 2111-2116.
110. Nguyen, T.-P., et al., *Degradation of phenyl C61 butryic acid methyl ester: poly (3-hexylthiophene) organic photovoltaic cells and structure changes as determined by defect investigations.* Journal of Photonics for Energy, 2012. **2**(1): p. 021013.

Vita

Eric Lewis Danielson was born in Houston, TX in 1985, but raised in Bryn Mawr, PA. After graduating from Radnor High School in 2003, he attended Trinity University in San Antonio, TX, where he earned a Bachelor of Science in Physics & Astronomy in 2007, studying apparent superluminal motion in radio-loud quasars. He attended graduate school briefly at the University of Florida in Gainesville, earning a Master of Science in Physics in 2008. He began his doctoral work in Materials Science and Engineering at The University of Texas at Austin in 2009. His doctoral thesis on organic bulk heterojunction photovoltaic materials has been supervised by Professor Ananth Dodabalapur.

Permanent email address: ibndaniel@gmail.com

This dissertation was typed by the author.